Post-Buckled Precompressed elements: a new class of control actuators for morphing wing UAVs

Roelof Vos

August 9, 2005

Summary

This report describes how Post-Buckled Precompressed (PBP) piezoelectric bender actuators are employed in a deformable wing structure which changes its camber and hence induces control. By applying axial compression to these actuators, significantly higher deflections can be achieved. Classical Laminate Plate Theory (CLPT) is shown to capture the behavior of the unloaded elements. A deflection model, employing nonlinear structural relations is shown to predict the behavior of the PBP elements accurately. Advantages of PBP actuators over conventional electro mechanical servo actuators are a substantial reduction in slop, dead band, complexity, power consumption and weight. Moreover, their corner frequency is an order of magnitude higher.

Two concepts are investigated. The wing of the first concept is based on the bending of a flat plate. The first 30% of the airfoil is shaped aerodynamically, whereas the remaining part is basically a flat plate with a total thickness of 0.5 mm, which is able to deflect up and down. One wing consists of two individual controllable panels. The inboard panel is used for direct lift control while the outboard panel induces roll control. This wing is designed for a 300 gram MAV (span 0.5 m). Precompression of the piezoelectric actuators is induced by rubber bands at both sides of each panel.

A dynamic test article was fabricated, which showed an increase in end rotation due to precompression of almost 100%, up to 14° peak to peak. A static article of this thin wing was fabricated which did not employ the piezoelectric actuators. This test article was used in the wind tunnel to verify the lifting capability of the wing at an early stage. A lift curve slope of $C_{l_\delta} = 3.80\ [1/rad]$ was obtained and attached flow was present up to 15° angle of attack. Extensive wind tunnel tests showed good stall behavior of the wing, and a maximum lift to drag ratio, $(C_L/C_D)_{max} = 5$. Furthermore, the lift as function of the shape deformation angle, δ, was measured to be $C_{L_\delta} = 2.97\ [1/rad]$, which translates to $C_{l_\delta} = 5.03\ [1/rad]$ for a two dimensional section of the wing.

The second wing design has a symmetric profile with finite thickness, incorporating the PBP actuators on the aft 60% of the camber line. This wing panel is used at the outboard parts of a wing for an existing UAV (span 1.4 m) in order to induce roll control. Due to the elasticity of the skin

the outer shape of the wing can be actively deformed. Moreover, the skin of the wing induced the required amount of precompression to the piezoelectric actuators.

For this thick wing, a proof-of-concept 100 mm wide wing section was fabricated. The tension in the wing skin could be varied in order to adjust precompression on the elements. Bench tests showed that with a wing chord of 145 mm deflection levels were increased with more than a factor of 2, to 15 degrees peak to peak, at a maximum frequency of 34 Hz. A new wing, employing the PBP morphing parts, was fabricated out of carbon fibre and flight testing was carried out which showed excellent control characteristics. The entire wing weight was reduced 9% with respect to the original wing, which did employ any wing movables. Each morphing part of the wing consisted of only 6 individual parts. Wind tunnel tests measured an average $C_{L_\delta} = 1.42$, which translates to $C_{l_\delta} = 4.16$ for a two dimensional wing section. The presence of wing loading caused a shift in deflection range at higher absolute angles of attack.

To control the morphing wing panels (for both the thick wing and the thin wing) an electronic circuit was designed. The PBP actuators demand a maximum voltage difference of 100V. To increase the control voltage to this value a linear amplifier was used. Battery voltage was increased with a direct current converter. Due to problems with demodulating the control signal and overheating of the amplifiers it was decided to separate the high voltage circuit from the low voltage control circuit and to link them mechanically. This led to a flight worthy electronic circuit which was suitable to control the morphing wing panels employed on the UAV. Moreover, losses were reduced and power consumption was limited to 0.1 W. However, the circuitry was relatively heavy, big and the control frequency was low.

The research that is presented in this report has shown that a PBP actuated morphing wing is a feasible and flight worthy concept and possesses significant benefits over conventional actuators. The PBP actuated morphing wing was demonstrated in benchtop experiments and its concept was proven in wind tunnel tests and in flight.

Nomenclature

Symbol	Description	Units
A	in-plane laminate stiffness matrix or aspect ratio	N m^{-1}, –
AR	amplification ratio	-
B	coupled laminate stiffness matrix	N
b	span	m
C	capacitance	F
c	chord	m
C_d, C_D	2 and 3 dimensional drag coefficient, resp.	-, -
C_{D_i}	induced drag coefficient	-
C_l, C_L	2 and 3 dimensional lift coefficient, resp.	-, -
C_m, C_M	2 and 3 dimensional pitching moment coefficient, resp.	-, -
C_p	pressure coefficient	-
D	bending laminate stiffness or drag force	N m, N
d	piezoelectric constant or diameter	m V^{-1}, m
E	electric field or stiffness	V m^{-1}, Nm^{-2}
e	Oswald factor	-
G	shear modulus of elasticity	N m^{-2}
I	2^{nd} area moment of inertia	m^4
k	spring stiffness	N m^{-1}
L	lift force	N
M	applied moment vector	N m
N	applied force vector	N
p	pressure	N m^{-2}
q	dynamic pressure	N m^{-2}
R	resistance	Ohm
Re	Reynolds number	-
S	wing surface area	m^2
SM	static margin	-
T	trust force, temperature or thermal strain vector	N, T, -
t	thickness or time	m, sec
U	internal energy	N m m^{-1}
u	vertical displacement	m
V	velocity, potential energy, voltage or volume	m s^{-1}, Nmm^{-1}, V, m^3
Z	Impedance	Ohm

Greek symbols

α	angle of attack or coefficient of thermal expansion	deg, microstrain K^{-1}
γ	shear strain	-
δ	PBP rotation angle	deg
ϵ	normal strain or downwash angle	-, deg
κ	curvature	deg m^{-1}
Λ	virgin actuator strain or sweep angle	-, deg
λ	taper ratio	-
μ	Poisson's Ratio	-
Π	potential energy	N m m^{-1}
ρ	density	kg m^{-3}
σ	normal stress	N m^{-2}
τ	shear stress	N m^{-2}
ω_n	angular frequency	s^{-1}

Subscripts

A	aircraft
a	actuator or axial
b	bonding layer or buckling
ac	aerodynamic center
cg	center of gravity
ex	external
f	fuselage
h	horizontal tail or hinge
l	laminate
s	substrate
t	thermal or tip
w	wing

Abbreviations

CLPT	Classical Laminate Plate Theory
CAP	Conventionally Attached PZT
CFD	Computational Fluid Dynamics
GFRP	Glass Fibre Reinforced Polymer
ISA	International Standard Atmosphere
MAV	Micro Aerial Vehicle
PBP	Post-Buckled Precompressed
PZT	Lead Titanate Zincronate
UAV	Unmanned Aerial Vehicle

Contents

List of Figures

Chapter 1

Introduction

For almost a century, piezoelectric materials have been used in various kinds of applications, ranging from SONAR detectors to twist active helicopter blades, to stereo tweeters. For more than fifteen years this unique branch of adaptive materials has been successfully used to enhance aircraft flight performance. Their relatively high mass specific energy and volume specific energy make them suitable to aircraft application [4].

Traditional actuator schemes for piezoelectric actuators tend to trade stroke at the expense of deflection. Recent studies at TU Delft and Auburn University have shown how the amount of deflection of piezoelectric actuators can be increased without decreasing the applied force. This new class of flight control actuators employ Post-Buckled Precompressed (PBP) piezoelectric elements. These actuators have been recently patented by TU Delft [2]. In the late 1990's it was first demonstrated by Lesieutre that when using an axial compression close to the buckling load of the actuator, the energy conversion efficiency becomes higher than the conversion efficiency of the raw piezoelectric material itself [14].

In general, most aircraft classes have extremely tight weight, volume and performance requirements. One of the most demanding types of aircraft are the small Uninhabited Aerial Vehicles (UAVs), known as Micro Aerial Vehicles (MAVs). The missions envisioned for MAVs, such as urban surveillance, require extreme agility. Although it has been shown that PBP actuators can be used successfully to enable MAV control, they have not yet been used as a structural part of either the wing or empennage to induce control [3]. It has been shown that wing morphing (using conventional actuators) provides excellent controllability and allows for rapid manoeuvring [16]. This report presents how this new class of flight control actuators is integrated into a flexible wing, allowing it to be deformed upon actuation.

Two individual wing morphing concepts are studied. Both concepts employ PBP actuators to induce wing morphing and consequently control of the

aircraft. However, both concepts have slightly different applications. The first concept contains a morphing wing designed for lift and roll control of an MAV (span 0.5m). The second concept is the design of two outboard morphing wing panels to provide roll control for a subscale UAV (span 1.4 m). An important similarity between both morphing wing concepts is the requirements they impose on the electronic control circuit.

The body of this report is divided in five chapters. After this introduction, background information on all the relevant topics is given in chapter 2. It is explained why this new type of wing morphing is very suitable for small aircraft with respect to larger aircraft. The basic principles of a Post-Buckled Precompressed (PBP) piezoelectric actuator are made explicit in chapter 3. Chapter 4 discusses the design, fabrication and testing of a thin morphing wing for an MAV. In chapter 5 design, fabrication and (flight) testing of a thick morphing wing for roll control on a small UAV is presented. The fifth chapter is dedicated to the design and manufacturing of a flight worthy electronic circuit for both morphing wing concepts. In the last chapter (7) of this report conclusions and recommendations are presented.

Chapter 2

Background and Motivation

In this chapter an overview is given of the main areas of interest that concern the investigation in so-called adaptive flight control. This includes an introduction in adaptive materials in general, and piezoelectric materials in particular. Also the concept of morphing wings is explained and why they should be used on Micro Aerial Vehicles. The chapter closes with a section on low Reynolds number aerodynamics.

2.1 Piezoelectric Materials

An adaptive material is defined to be a material which undergoes a change in mechanical, thermal, optical, chemical, geometrical, electrical or magnetic properties as a function of a given stimulus . The stimulus may be heat, a magnetic field, or, in case of piezoelectric materials, an electric field. An adaptive aerostructure is a structure which uses highly integrated, normally load bearing, adaptive materials, to undergo a change in mechanical, thermal, optical, geometrical, electrical, or magnetical state as as function of a given stimulus [6].

A piezoelectric material generates a mechanical motion or a change in stress field when exposed to an electric field. Conversely they undergo a change in electric charge state when exposed to a directional change in motion or a stress field [6]. Consequently, they can be used as both actuator and sensor. As a sensor, piezoelectric materials are not unfamiliar to the aircraft industry. Using resonance techniques they are used in turbine engines to detect small cracks in the turbine blades.

As an actuator the piezoelectric materials are less commonly used in (civil) aircraft industry. Piezoelectric elements have been used on the F-18 to alleviate buffet on the horizontal tail surface. The reason why active piezoelectric elements are not used as commonly as their passive counterparts

is twofold. Most importantly, they are relatively brittle and heavy. Using them as structural material is therefore not appealing. As part of an actuator (so not integrated in the structure) is possible. Secondly, due to the conservativeness of the aerospace world it is out of the question that these materials are to be used as primary or secondary structure, in the near future. Consequently, care must be taken when it comes to applying these materials. It should always be kept in mind that using these materials puts quite some constraints on the design. It must be verified that their use actually contributes to a better performance, lower cost, or whatever it is that needs to be optimized.

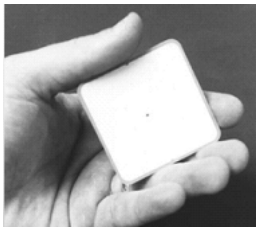

(a) Block cast Piezo ceramic [6]

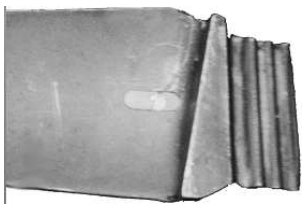

(b) Piezoelectric sensor in turbine blade [6]

(c) F-18 Active Aeroelastic Wing [37]

Figure 2.1: Piezoelectric materials and applications

This does not mean that piezoelectric material does not have a relevant application in modern aircraft industry. To see why this might be so, it is important to understand the capabilities of this material. As established above, active piezoelectric material shows strain when an electric field is applied. In other words, when exposed to an electric field the material will contract or expand, depending on the direction of the electric field. This has to do with the fact that the material is poled in a specific direction (confer section 3.1 for more detailed explanation). By altering the direction of the electric field it is possible to make the material contract and expand very rapidly. In fact, frequencies over 100 kHz are possible. This characteristic makes it very suitable for applications which desire high speed actuation.

2.2 Morphing Wings

Wing morphing is actually quite an old concept in aircraft industry. The Wright brothers used it in all their aircraft, including the Wright flyer II, the first aircraft to actually fly. By pulling wires, which were attached to the wing, the wing shape changed, inducing a change in pressure distribution and consequently a change in lift. That way, they were able to steer the aircraft [13].

That morphing is an efficient concept for control is proven by nature. Birds all make use of their morphing wings to adapt to different flight conditions. Those super morphing wings do not only change in twist and camber, but also in aspect ratio, dihedral and sweep. Moreover, birds do not possess a vertical tail surface for directional control. The morphing wings are used as ailerons, flaps, slats and direct lift control. To be short, bird wings show that there is still much to improve in aircraft wing design.

One step forward to resemble birds more closely is to apply morphing wings to an aircraft. However, this is not easily done, since conventional aircraft all have a rigid wing construction, which only have a limited amount of flexibility. They must be able to carry the weight of the aircraft, when in the air, and their own weight plus fuel, when on the ground. Morphing wings would require a relatively flexible structure which is able to provide sufficient strength to the wing on the one hand, but also give the wing the ability to change its shape. This shape change can either be a change in camber, thickness (t/c), aspect ratio, sweep, dihedral or twist. Each of the afore mentioned characteristics typically induce weight, volume and flexibility increments and penalties.

Wing morphing, to a certain extent, has been successful in the past and the present. Increasing of chord and camber is the most regular way of wing morphing in commercial and military aircraft. Flaps and slats are deployed to adapt to the speed regimes occurring at, for instance, take off and landing. This however, proves the wide interpretation that can be given to the term 'morphing.' The F-14 Tomcat is provided with a wing that can change sweep angle (so-called 'swing wings'). It can therefore operate at a larger speed range. Here the wing hinges around an hinge point and is rotated backwards when the speed is increased. Above two examples both contain a shape change of the wing. However, this shape change is in fact due to the sliding or rotating of stiff elements of the wing. The structure itself remains rigid. To be short, the current methods of wing morphing are only an approximation of real structural morphing. Structural morphing *is* possible when adaptive aerostructures are used.

Structural morphing for a 30 cm span aircraft was achieved by Lind at the University of Florida. By pulling a string that runs between the wing tip and the fuselage, the wing is deformed. Flight testing showed that wing morphing can be an effective means to achieve roll control for this class of small aircraft [16].

2.3 Micro Aerial Vehicle

During the past few years Unmanned Aerial Vehicles (UAVs) have become a new major segment in aircraft industry. Especially defense projects are

(a) Wright flyer [38] (b) Eagle [39] (c) Structural morphing of a 30 cm span aircraft [16]

Figure 2.2: Various types of wing morphing

more and more directed towards autonomous flight of robotic aircraft. Dangerous operations such as reconnaissance and post battle assessment can be done by these aircraft without risking the life of pilots. On top of that are the Uninhabited Combat Aerial Vehicles, or UCAVs, which can be used to conduct pre-emptive and reactive suppression of enemy air defense missions effectively and affordably.

The use of morphing wings on UAVs is a topic of interest for many research institutions around the world (among others DARPA in their Morphing Aircraft Structure program [36]). Both structural morphing of wings by means of adaptive materials, as shape change due to hinging or inflating parts of the wing, is looked into. A lot of different configurations as well as material applications are examined. On the one hand there is the investigation in adaptive materials to induce camber changes or active twist in the wing. On the other hand there is interest in extending, hinging, inflating and/or folding wings. The applications of morphing wings are currently targeted to UAVs because of their low wing loading and the ability to quickly perform flight tests [27].

Since structural morphing is limited to camber variations, bending and active twist, this is where adaptive materials could be applied. An important design parameter with respect to morphing wings on UAV aircraft is their size. When piezoelectric materials are used to actuate the morphing wing, there are some dimension related characteristics that should be considered when designing a UAV. Currently, UAV dimensions range from several meters in span up to several centimeters [32]. In order to determine what size would be appropriate for UAVs with morphing wings, actuated by piezoelectric materials, a comparison is made. Table 2.3 gives an overview of size related characteristics for larger and smaller UAVs. The left column considers a morphing wing on a micro aerial vehicle (span $<$ 50 cm), the right column on an 'ordinary' UAV (span $>$ 50 cm).

[!htp]

	MAV	**UAV**
Atmospheric instabilities	Small moment of inertia: requires fast actuators to counteract this	Larger moment of inertia, requires less fast actuators
Agility	Improves: small moment of inertia in combination with fast actuators	Large moment of inertia prevents agility to improve
Manufacturing	Simple to make a proof-of-concept model	Limited size of available piezoelectric materials would yield more complicated structure.
Weight	Weight saving due to PZT elements will be considerable[3]	Weight saving due to PZT elements not ensured due to relatively complicated structure [9]
Volume	Relatively large volume reduction w.r.t. conventional actuators	Relatively small volume reduction w.r.t. conventional actuators
Power	Piezoelectric actuators will reduce power consumption substantially	Structural resistance could lead to a higher power consumption.

Comparison MAV and UAV.

From Table 2.3 different conclusions on size could be drawn. An important one is that the overall benefits from using PBP actuators are larger for the MAV application than for the UAV. Weight and volume savings are more substantial, power consumption will decrease and the aircraft becomes more agile. From the MAV point of view, the capability of fast actuation is not so much desired as it is an absolute necessity to operate. With ever decreasing size of aircraft, they become more and more sensitive to wind gusts and other atmospheric instabilities. Since their speeds are generally between 10 and 20 m/s, wind speed is not something trivial anymore [15]. To act and react to these conditions the aircraft should possess fast and efficient actuators. Since conventional actuators only go up to frequencies of 1 to 2 Hz, these will not be capable of coping with quick changes in flow field. The piezoelectric actuators would be very suitable to perform changes in wing geometry up to 25 Hz. Another reason to use the PZT laminates is the fact that they can be integrated in membrane wings, which are commonly used for MAV's.

2.4 Low Reynolds Number Aerodynamics

To construct a wing for a UAV can be different from constructing a wing for a MAV. The difference is caused by the difference in Reynolds number between both. The Reynolds number is defined as in equation 2.1 [1].

$$Re = \frac{\rho V c}{\mu} \tag{2.1}$$

In equation (2.1) ρ is the density of the fluid. For air $\rho = 1.225$ $[kg/m^3]$, at 0m International Standard Atmosphere (ISA). V is the velocity in $[m/s]$ and μ is the viscosity of the fluid in $[N/s/m^2]$. At $0m$ ISA for air $\mu = 1.73 \cdot 10^{-5}$ $[N/s/m^2]$. Finally the c represents a characteristic length, usually the chord of the wing in $[m]$. For the MAV configuration the speeds will be around 15 m/s. Furthermore, a chord length of approximately 10 cm is realistic. Substituting these numbers into equation 2.1 gives an approximate Reynolds number of $1 \cdot 10^5$.

Low Reynolds number aerodynamics is quite different from high Reynolds number aerodynamics. Different flow problems arise. One of them is the possible occurrence of laminar separation at the leading edge of the airfoil. Due to high local curvature, the laminar boundary layer will not be able to follow the contour of the airfoil. It will therefore separate. After separation, the boundary layer could become turbulent (more energized) and could re-attach to the surface of the airfoil. This leaves the so-called laminar separation bubble, figure 2.3. The laminar separation bubble increases drag considerably. In addition the lift is decreased. Re-attachment of the flow only takes place if the boundary layer becomes turbulent, otherwise the boundary layer will just separate, causing a large wake and consequently a huge amount of drag. This form of leading edge separation destroys the lift over the wing completely [1].

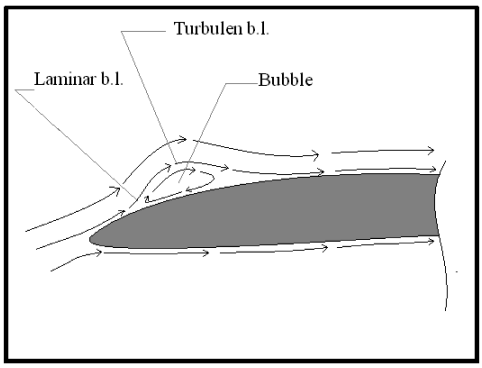

Figure 2.3: Schematic representation of the boundary layer.

Laminar separation bubbles are a common feature on airfoils at Reynolds numbers between 50,000 and 200,000. They tend to be larger with decreasing Reynolds number. They cause a substantial decrease in L/D. However, it is possible to control the laminar separation bubble: artificial turbulators can be placed on the leading edge to cause the boundary layer to trip. The

laminar flow in the boundary layer becomes turbulent and will have more strength to follow the curvature of the airfoil. Determining the size and the location of these turbulators is more an art than it is science [19].

Not only turbulators can energize the boundary layer, tip vortices also tend to do this, causing the bubble to disappear near the tips of the wing. This is a typical low Reynolds number phenomenon. The pressure at the top side of the airfoil, near the tip of the wing, gets lower than at an average spanwise location. This causes an increase in lift near the wing tips. This is contradictory to what happens at high Reynolds numbers. In the latter case the tip vortices tend to increase the pressure on the top side of the wing. This deteriorates the lift at the tip. The increase in lift near the tip is something the MAV can benefit from [22].

The low Reynolds number also puts constraints on the design of the airfoil. Thin airfoils ($t < 0.05c$) seem to give better results than thick airfoils. Furthermore, the sharpness of the trailing edge, as well as turbulence does not have much effect on the lift, drag and pitching moment. Also, slightly cambered airfoil (around 4%) perform better than straight airfoils [19].

In combination with low Reynolds numbers, the aspect ratio (A) is an important feature with respect to aerodynamics of MAV's. The aspect ratio is defined to be the square of the span divided by the surface area of the wing. The relatively low aspect ratios of MAV wings (down to $A = 0.5$) cause again two special characteristics: a high stall-angle of attack, and a non-linear C_L/α curve. Both features are caused by the interference of the tip vortices with the boundary layer on top of the wing [24][22].

2.5 Synopsis

This chapter has shown that piezoelectric materials are already being regularly applied in aerospace industry both as actuator and sensor. An introduction into 'morphing' wings has shown that there is a difference between structural deforming wings and wings that change shape due to sliding or hinging components and that both types can induce aircraft control. Furthermore, it has been concluded that piezoelectric morphing wings could best be applied to small UAVs rather than to larger ones. Finally, a qualitative aerodynamic analysis has shown that at low Reynolds number thin airfoils with a sharp nose and a slight camber should perform best in terms of lift and drag.

Chapter 3

Post Buckled Precompressed Piezoelectric Actuator

In this chapter the theory behind the piezoelectric actuator and its capabilities is explained in detail. First of all the principles of a piezoelectric actuator are explained. In section 2 the actuator laminate is analyzed using Classical Laminate Plate Theory. To be able to predict the deflection in the beam a Newtonian model is presented in the third section. On top of that, a potential energy model is laid out in section four, which can be used to calculate the relation between tip force and deflection.

3.1 Piezoelectric Actuator

There are different kinds of piezoelectric materials. One commonly used is the led-zincronate-titanium (PZT) ceramic. This material possesses a number of relevant characteristics which should be kept in mind when designing a structure using PZT materials. High stress fields can de-pole the element which means it becomes inactive. The same happens when the element breaches its Curie temperature. Self heating can occur when the element is exposed to high stress levels. Furthermore, the elements have low fracture toughness and a low ultimate tensile strength; they are very difficult to handle in foil thicknesses because of their extreme brittleness. When cracks occur in the surface of the PZT material, arcing can occur between the electrically connected part and the disconnected part of the surface. And finally, the performance of the elements tends to degrade with time after the poling process (usually measured in decades). On the other hand, when the element is poled again, it is as new.

The brittleness of the sheet material and the low ultimate tensile strength make the manufacturing of PZT structures a laborious process. By attach-

ing the PZT sheets to a metal substrate, it is possible to make an active bender element. If, during the curing of the adhesive, the laminate is heated, the metal substrate will expand more than the PZT due to a mismatch in coefficient of thermal expansion. After the resin has set, the element will cool again and compress the PZT which it is attached to. This means that the PZT material is under constant compression. This internal precompression makes the actuator much less brittle.

To avoid curvature in the laminate it is also possible to make a so-called bimorph: a metal substrate with two PZT elements attached in the same direction on either side (compare figure 3.1(a)). This class of actuators are termed Conventionally Attached PZT (CAP) elements. The bimorph structure is most simple to manufacture. If the sheets are attached correctly, applying an electric field results in straining the PZT sheets in equal but opposite directions. This will induce an anti-symmetric motion of the laminate about its axis of symmetry.

The maximum strain on a PZT-element is determined by two properties of the material: the piezoelectric constants (d_{ij}) and the electric field strength at which the element de-poles. The piezoelectric constant d_{ij} is the ratio between the induced strain in the j direction and the applied field in the i direction, where $i, j = 1, 2, 3$. For example d_{31} is the ratio between the electric field in direction 3 (the electrodes are perpendicular to axis 3) and the induced strain or applied stress in direction 1. The three directions are orthogonal and direction 3 is the poling direction of the element, confer figure 3.1(b). The field strength is given in V/mm and can go up to 600 $[V/mm]$, before the material is being de-poled.

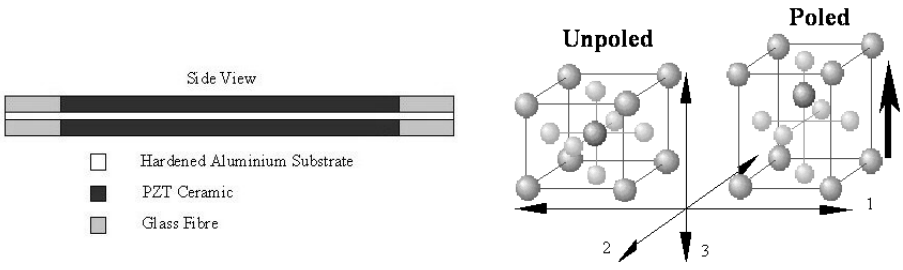

(a) Example of a bimorph piezoelectric actuator **??**.

(b) The Titanium atom is displaced during poling **??**.

Figure 3.1: PZT actuator and atom structure.

Because the field levels exceed 200 $[V/mm]$, the assumption that the thickness of the PZT sheet is independent of the electric field may not me used.

The field strength *is* dependent on the thickness of the actuator (eqn. (5) in [18]):

$$E_j = \frac{t_a}{V_j} \tag{3.1}$$

Equation 3.2 gives the relation between the free strain and the applied field strength, E (eqn. (6) in [18]).

$$\Lambda_i = d_{ij} E_j \tag{3.2}$$

PZT 5A is a material with a strain/applied field ratio, $d_{31} = d_{32} = -171 \cdot 10^{-9}$ $[mm/V]$, $d_{33} = 374 \cdot 10^{-9}$ $[mm/V]$. This material is very suitable as actuation element in a bimorph CAP laminate. From a practical point of view the d_{31} coefficient is most interesting. It is relatively simple to apply a sufficient electric field over a laminate in thickness direction, because it is usually very thin. Expansion/contraction will occur perpendicular to the field direction.

3.2 Classical Laminated Plate Theory Model

To model the behavior of a free piezoelectric laminate Classical Laminated Plate Theory (CLPT) is used. The analysis presented in this section follows the assumptions laid out in Jones [12]. Appendix A gives a more detailed overview of the CLPT analysis applied to a piezoelectric actuator. In this section the theory is laid out in a more general way. The resultant forces and moments in the laminate are obtained by integrating the stress over the thickness of the laminate (eq. (4.14) in [12]).

$$N_x = \int_{-t/2}^{t/2} \sigma_x dz \qquad M_x = \int_{-t/2}^{t/2} \sigma_x z dz \tag{3.3}$$

For forces and moments in all directions and for N number of laminae, equation (3.3) expands to the following expression (eqns. (4.15) and (4.16) in [12]).

$$\begin{pmatrix} N_x \\ N_y \\ N_{xy} \end{pmatrix} = \int_{-t/2}^{t/2} \begin{pmatrix} \sigma_x \\ \sigma_y \\ \tau_{xy} \end{pmatrix} dz = \sum_{k=1}^{N} \int_{z_{k-1}}^{z_k} \begin{pmatrix} \sigma_x \\ \sigma_y \\ \tau_{xy} \end{pmatrix}_k dz \tag{3.4}$$

$$\begin{pmatrix} M_x \\ M_y \\ M_{xy} \end{pmatrix} = \int_{-t/2}^{t/2} \begin{pmatrix} \sigma_x \\ \sigma_y \\ \tau_{xy} \end{pmatrix} z dz = \sum_{k=1}^{N} \int_{z_{k-1}}^{z_k} \begin{pmatrix} \sigma_x \\ \sigma_y \\ \tau_{xy} \end{pmatrix}_k z dz \tag{3.5}$$

The thicknesses in equations 3.4 and 3.5 refer to figure 3.2.

The PZT sheets that are used in the laminate is so-called orthotropic material. An orthotropic material possesses symmetry in stiffness properties with

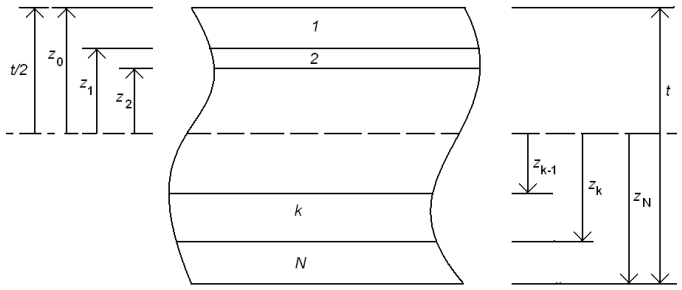

Figure 3.2: Geometry of an N-layered laminate.[12]

respect to two or more directions perpendicular to another. For orthotropic materials the relation between stress and strain can be written as follows (eqn. (2.59) in [12]):

$$\begin{pmatrix} \sigma_1 \\ \sigma_2 \\ \tau_{12} \end{pmatrix} = \begin{bmatrix} Q_{11} & Q_{12} & 0 \\ Q_{12} & Q_{22} & 0 \\ 0 & 0 & Q_{66} \end{bmatrix} \begin{pmatrix} \epsilon_1 \\ \epsilon_1 \\ \gamma_{12} \end{pmatrix} \tag{3.6}$$

Where the matrix components, Q_{ij}, are a function of the stiffness of the material (E_i) and Poisson's ratio (μ_{ij}) (eqn. (2.61) in [12]):

$$Q_{11} = \frac{E_1}{1 - \mu_{12}\mu_{21}} \tag{3.7}$$

$$Q_{12} = \frac{\mu_{12}E_2}{1 - \mu_{12}\mu_{21}} \tag{3.8}$$

$$Q_{22} = \frac{E_2}{1 - \mu_{12}\mu_{21}} \tag{3.9}$$

$$Q_{66} = G_{12} \tag{3.10}$$

The above stiffness components can be transformed to a rotated coordinate system, xyz. This coordinate system is rotated over an angle θ, using the 3-axis as rotational axis (cf. figure 3.3). The rotated stiffness components then become (eqn. (2.79) and (2.80) in [12])

$$\begin{pmatrix} \sigma_x \\ \sigma_y \\ \tau_{xy} \end{pmatrix} = \begin{bmatrix} \overline{Q}_{11} & \overline{Q}_{12} & \overline{Q}_{16} \\ \overline{Q}_{12} & \overline{Q}_{22} & \overline{Q}_{26} \\ \overline{Q}_{16} & \overline{Q}_{26} & \overline{Q}_{66} \end{bmatrix} \begin{pmatrix} \epsilon_x \\ \epsilon_y \\ \gamma_{xy} \end{pmatrix} \tag{3.11}$$

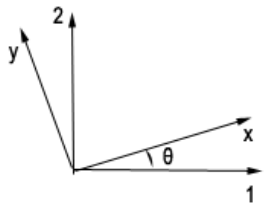

Figure 3.3: Rotation of the coordinate system.

Where:

$$\overline{Q}_{11} = Q_{11}cos^4\theta + 2(Q_{12} + 2Q_{66})sin^2\theta cos^2\theta + Q_{22}sin^4\theta \tag{3.12}$$

$$\overline{Q}_{12} = (Q_{11} + Q_{22} - 4Q_{66})sin^2\theta cos^2\theta + Q_{12}(sin^4\theta + cos^4\theta) \tag{3.13}$$

$$\overline{Q}_{22} = Q_{11}sin^4\theta + 2(Q_{12} + 2Q_{66})sin^2\theta cos^2\theta + Q_{22}cos^4\theta \tag{3.14}$$

$$\overline{Q}_{16} = (Q_{11} - Q_{12} - 2Q_{66})sin\theta cos^3\theta + (Q_{12} - Q_{22} + 2Q_{66})sin^3\theta cos\theta \tag{3.15}$$

$$\overline{Q}_{26} = (Q_{11} - Q_{12} - 2Q_{66})sin^3\theta cos\theta + (Q_{12} - Q_{22} + 2Q_{66})sin\theta cos^3\theta \tag{3.16}$$

$$\overline{Q}_{66} = (Q_{11} + Q_{22} - 2Q_{12} - 2Q_{66})sin^2\theta cos^2\theta + Q_{66}(sin^4\theta + cos^4\theta) \tag{3.17}$$

The stress strain relations in an arbitrary coordinate system (equation 3.11) are useful for determining the stiffness of the entire laminate. Following Jones the strain in the laminate can be split up into vectors: an in plane and an out of plane strain vector. The first of these vectors gives the middle surface strain of the laminate and the second vector gives the middle surface curvature (eqn. (4.13) in [12]).

$$\begin{pmatrix} \epsilon_x \\ \epsilon_y \\ \gamma_{xy} \end{pmatrix} = \begin{pmatrix} \epsilon_x^0 \\ \epsilon_y^0 \\ \gamma_{xy}^0 \end{pmatrix} + z \begin{pmatrix} \kappa_x \\ \kappa_y \\ \kappa_{xy} \end{pmatrix} \tag{3.18}$$

The results of equations 3.11 and 3.18 can now be substituted in equations 3.4 and 3.5. This gives the following expression for the force and moment

vectors (eqns. (4.17) and (4.18) in [12]):

$$\begin{pmatrix} N_x \\ N_y \\ N_{xy} \end{pmatrix} = \sum_{k=1}^{N} \begin{bmatrix} \overline{Q}_{11} & \overline{Q}_{12} & \overline{Q}_{16} \\ \overline{Q}_{12} & \overline{Q}_{22} & \overline{Q}_{26} \\ \overline{Q}_{16} & \overline{Q}_{26} & \overline{Q}_{66} \end{bmatrix}_k \left\{ \int_{z_{k-1}}^{z_k} \begin{pmatrix} \epsilon_x^0 \\ \epsilon_y^0 \\ \gamma_{xy}^0 \end{pmatrix} dz + \int_{z_{k-1}}^{z_k} \begin{pmatrix} \kappa_x \\ \kappa_y \\ \kappa_{xy} \end{pmatrix} z dz \right\} \tag{3.19}$$

$$\begin{pmatrix} M_x \\ M_y \\ M_{xy} \end{pmatrix} = \sum_{k=1}^{N} \begin{bmatrix} \overline{Q}_{11} & \overline{Q}_{12} & \overline{Q}_{16} \\ \overline{Q}_{12} & \overline{Q}_{22} & \overline{Q}_{26} \\ \overline{Q}_{16} & \overline{Q}_{26} & \overline{Q}_{66} \end{bmatrix}_k \left\{ \int_{z_{k-1}}^{z_k} \begin{pmatrix} \epsilon_x^0 \\ \epsilon_y^0 \\ \gamma_{xy}^0 \end{pmatrix} z dz + \int_{z_{k-1}}^{z_k} \begin{pmatrix} \kappa_x \\ \kappa_y \\ \kappa_{xy} \end{pmatrix} z^2 dz \right\} \tag{3.20}$$

Keeping in mind that ϵ_i^0 and κ_i are middle surface strains and therefore independent of z, these equations can be written as follows (eqns. (4.19) to (4.21) in [12]):

$$\begin{pmatrix} N_x \\ N_y \\ N_{xy} \end{pmatrix} = \begin{bmatrix} A_{11} & A_{12} & A_{16} \\ A_{12} & A_{22} & A_{26} \\ A_{16} & A_{26} & A_{66} \end{bmatrix} \begin{pmatrix} \epsilon_x^0 \\ \epsilon_y^0 \\ \gamma_{xy}^0 \end{pmatrix} + \begin{bmatrix} B_{11} & B_{12} & B_{16} \\ B_{12} & B_{22} & B_{26} \\ B_{16} & B_{26} & B_{66} \end{bmatrix} \begin{pmatrix} \kappa_x \\ \kappa_y \\ \kappa_{xy} \end{pmatrix} \tag{3.21}$$

$$\begin{pmatrix} M_x \\ M_y \\ M_{xy} \end{pmatrix} = \begin{bmatrix} B_{11} & B_{12} & B_{16} \\ B_{12} & B_{22} & B_{26} \\ B_{16} & B_{26} & B_{66} \end{bmatrix} \begin{pmatrix} \epsilon_x^0 \\ \epsilon_y^0 \\ \gamma_{xy}^0 \end{pmatrix} + \begin{bmatrix} D_{11} & D_{12} & D_{16} \\ D_{12} & D_{22} & D_{26} \\ D_{16} & D_{26} & D_{66} \end{bmatrix} \begin{pmatrix} \kappa_x \\ \kappa_y \\ \kappa_{xy} \end{pmatrix} \tag{3.22}$$

Where:

$$A_{ij\ n} = \sum_{k=1}^{N} (\overline{Q}_{ij})_k (z_k - z_{k-1}) \delta_{kn} \tag{3.23}$$

$$B_{ij\ n} = \frac{1}{2} \sum_{k=1}^{N} (\overline{Q}_{ij})_k (z_k^2 - z_{k-1}^2) \delta_{kn} \tag{3.24}$$

$$D_{ij\ n} = \frac{1}{3} \sum_{k=1}^{N} (\overline{Q}_{ij})_k (z_k^3 - z_{k-1}^3) \delta_{kn} \tag{3.25}$$

In the above equations δ_{kn} is the Kronecker delta where $\delta = 1$ for $k = n$ and $\delta = 0$ for $k \neq n$. The subscript n denotes the A,B or D-matrix for the n'th layer *in* the laminate. The laminate consists of five layers: two actuator layers ($k, n = 1$ and $k, n = 5$), two bonding layers ($k, n = 2$ and $k, n = 4$) and the substrate ($k, n = 3$). Adding the ABD-matrices for the individual layers in the laminate (with subscript l) results in the A,B and D-matrices for the entire laminate:

$$A_{ij\ l} = \sum_{n=1}^{N} A_{ij\ n} \tag{3.26}$$

$$B_{ij\ l} = \sum_{n=1}^{N} B_{ij\ n} \tag{3.27}$$

$$D_{ij\ l} = \sum_{n=1}^{N} D_{ij\ n} \tag{3.28}$$

With these components equation (3.2) can also be written as:

$$\begin{pmatrix} N \\ M \end{pmatrix} = \begin{bmatrix} A & B \\ B & D \end{bmatrix}_l \begin{pmatrix} \epsilon^0 \\ \kappa \end{pmatrix}_l \tag{3.29}$$

The forces and moments in equation (3.29) can be sub-categorized in actuator in-plane forces and moments (a), external forces and moments (ex) and forces and moments due to a mismatch in coefficients of thermal expansion (t) [3].

$$\begin{pmatrix} N \\ M \end{pmatrix}_a + \begin{pmatrix} N \\ M \end{pmatrix}_{ex} + \begin{pmatrix} N \\ M \end{pmatrix}_t = \begin{bmatrix} A & B \\ B & D \end{bmatrix}_l \begin{pmatrix} \epsilon^0 \\ \kappa \end{pmatrix}_l \tag{3.30}$$

If external forces and moments are ignored, that is the element is free to move, and when thermally induced stresses are not considered, this equation can be reduced to (eqn. 4 in [18]):

$$\begin{bmatrix} A & B \\ B & D \end{bmatrix}_a \begin{pmatrix} \Lambda \\ 0 \end{pmatrix}_a = \begin{bmatrix} A & B \\ B & D \end{bmatrix}_l \begin{pmatrix} \epsilon^0 \\ \kappa \end{pmatrix}_l \tag{3.31}$$

Λ represents the virgin strain of the actuator, which is a function of the electric field, E_j, and the actuator thickness, d_{ij}, as in equation (3.2). The ABD-matrix for the two actuators in the laminate carry the subscript (a). This matrix is a superposition of the two matrices which result from inserting $n = 1$ and $n = 5$ in equations (3.23) to (3.25). Equation (3.31) shows how the in-plane strain and the curvature of the laminate (l) are related to the free strain of the actuator (a). The curvature is of main importance. The laminate that is used in this actuator consists of five layers: [CAP($+\Lambda$)/bond/isotropic sustrate/bond/CAP($-\Lambda$)]. Since this laminate is symmetric in both material as geometrical properties, with respect to the midplane of the laminate, all the coupling stiffnesses, $(B_{ij})_l$, become zero (sec. 4.3.2 in [12]). Applying this to equation (3.31) the curvature of the

laminate can be directly coupled to the free strain in the actuators (eqn. (4) in [3]):

$$\kappa = \frac{B_a}{D_l}\Lambda \tag{3.32}$$

For the bending actuator κ_{11} represents the curvature w.r.t. the 1-axis, and can be deduced from equation (3.32). It is assumed that the two piezoelectric actuators are attached at either side of an isotropic substrate with a bond of finite thickness and low stiffness. Lateral contraction is therefore neglected. When all the appropriate substitutions are made, $\theta_s = \theta_a = 0$, the expression for κ_{11} is as in equation (3.33), in which subscript s denotes substrate and b stands for bonding layer (eqn. (4) in [18]).

$$\kappa_{11} = \frac{E_a(t_s t_a + 2t_b t_a + t_a^2)}{\left(\frac{E_s t_s^3}{12}\right) + E_a\left\{\left[\frac{t_a(t_s+2t_b)^2}{2}\right] + (t_s + 2t_b)t_a^2 + \frac{2}{3}t_a^3\right\}}\Lambda_1 \tag{3.33}$$

3.3 Analysis of a PBP laminate

The previous section showed how in a free pzt-laminate the free strain of each of the actuator elements is related to the curvature of the laminate. In this section it is shown that the curvatures in the laminate can be increased considerably when a compressive force is applied at the center line of the laminate. This type of actuator is termed a Post Buckled Precompressed (PBP) piezoelectric actuator and the principle that it is based upon is shown in figure 3.4.

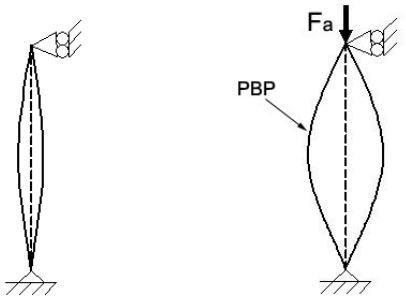

(a) Without compressive force.

(b) With compressive force.

Figure 3.4: Pre-compression increases deflection [18].

The following analysis of the PBP actuator is laid out in [3]. All the formulae appearing in the following analysis are taken from this source. Referring to figure 3.5, it is assumed that the element is only loaded in pure bending and

that the rotations are moderate. The normal strain in the laminate at any distance y from the neutral axis through its thickness is expresses as:

$$\epsilon = \frac{yd\delta}{ds} = \frac{\sigma}{E} \tag{3.34}$$

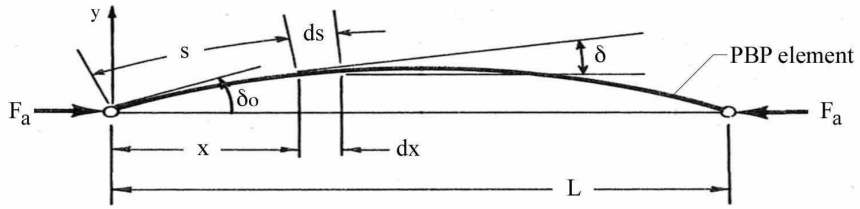

Figure 3.5: Terms and conventions for analysis of the PBP actuator arrangement [3].

For a beam element in pure bending the following holds:

$$\sigma = \frac{My}{I} \tag{3.35}$$

Combining equations (3.34) and (3.35) and inserting CLPT conventions and terminology the following can be obtained:

$$\frac{yd\delta}{ds} = \frac{My}{Db} \tag{3.36}$$

The moment that is externally applied comes from the compressive force, F_a:

$$M = -F_a y \tag{3.37}$$

Substituting equation (3.37) in equation (3.36) yields:

$$\frac{d\delta}{ds} = -\frac{F_a y}{Db} \tag{3.38}$$

When (3.38) is differentiated with respect to s the following expression is obtained:

$$\frac{d^2\delta}{ds^2} = -\frac{F_a}{Db}\sin\delta \tag{3.39}$$

Multiplying this result with an integrating factor $2\frac{d\delta}{ds}$ yields:

$$2\frac{d\delta}{ds}\frac{d^2\delta}{ds^2} = -2\frac{F_a}{Db}\sin\delta\frac{d\delta}{ds} \tag{3.40}$$

Integrating equation (3.40):

$$\left(\frac{d\delta}{ds}\right)^2 = 2\frac{F_a}{Db}\cos\delta + a \tag{3.41}$$

To determine the integration constant, a, it is considered that the applied moment via the piezoelectric elements generates an imperfection across the beam. It is then given that at $x = 0$:

$$\delta = \delta_0 \qquad \frac{d\delta}{ds} = \kappa$$

Substituting these expressions yields for the integration constant, $a = \kappa^2$, and accordingly equation (3.41) results in:

$$\left(\frac{d\delta}{ds}\right)^2 = 2\frac{F_a}{Db}(\cos\delta - \cos\delta_0) + \kappa^2 \tag{3.42}$$

Using the appropriate trigonometric substitutions and considering the negative root because $d\delta$ is always negative:

$$\frac{d\delta}{ds} = -2\sqrt{\frac{F_a}{Db}}\sqrt{\sin^2\left(\frac{\delta_0}{2}\right) - \sin^2\left(\frac{\delta}{2}\right) + \frac{\kappa^2 Db}{4F_a}} \tag{3.43}$$

To solve this equation a change of variables is imposed:

$$\sin\left(\frac{\delta}{2}\right) = c\sin\xi \tag{3.44}$$

Where ξ is a variable with the value $\pi/2$ when $x = 0$ and the value of 0 at $x = \frac{L}{2}$. Consequently at $x = 0$:

$$c = \sin\left(\frac{\delta_0}{2}\right) \tag{3.45}$$

Solving for δ and differentiating with respect to ξ yields:

$$\delta = 2\sin^{-1}\left(\sin\left(\frac{\delta_0}{2}\right)\sin\xi\right) \qquad d\delta = \frac{2\sin\left(\frac{\delta_0}{2}\right)\cos\xi}{\sqrt{1 - \sin^2\left(\frac{\delta_0}{2}\right)\sin^2\xi}}\xi \tag{3.46}$$

When equations (3.43) to (3.46) are combined, this leads to the following result:

$$\sqrt{\frac{F_a}{Db}}\int_0^{\frac{L}{2}} ds = \frac{L}{2}\sqrt{\frac{F_a}{Db}} = \\ = \int_0^{\frac{\pi}{2}} \frac{\sin\left(\frac{\delta_0}{2}\right)\cos\xi}{\left(\sqrt{\sin^2\left(\frac{\delta_0}{2}\right)\cos^2\xi + \frac{\kappa^2 Db}{4F_a}}\right)\left(\sqrt{1 - \sin^2\left(\frac{\delta_0}{2}\right)\sin^2\xi}\right)} d\xi \tag{3.47}$$

Equation (3.47) does not have a closed form solution but it can be solved numerically. For a given precompressive force, F_a, both the left and the right side are solved. Depending on the difference between each of these solutions δ_0 is increased or decreased. After this alteration the routine is run again and eventually it will converge to the point where both sides of the equation are equal. This is the value of δ_0 that belongs to the specific value of F_a. Appendix B presents the Matlab code that was written to solve this equation. Figure 3.6 shows a result of applying this model at various potential levels to a piezoelectric element with dimensions as shown in figure A.1. In this model it is assumed that the total length (92 mm) of the laminate is covered by the PZT actuators.

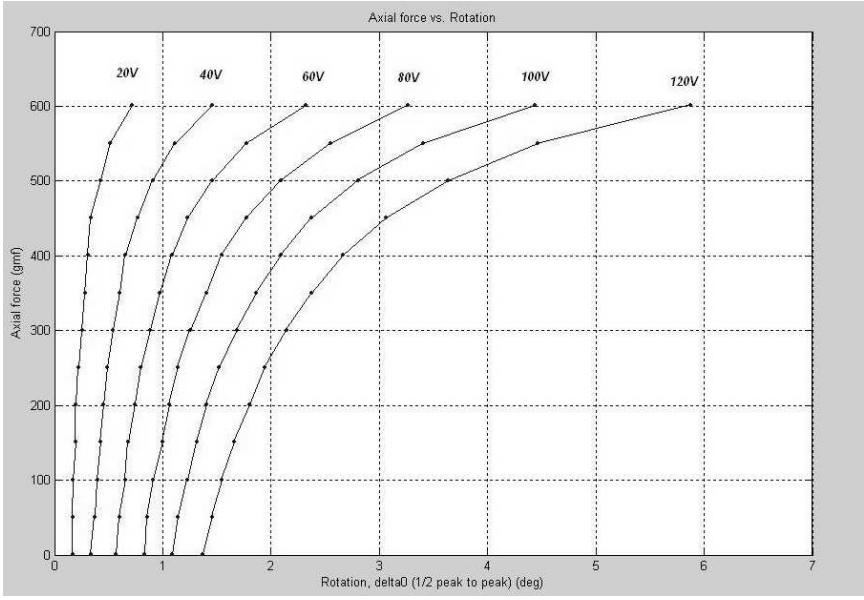

Figure 3.6: Modeled relationship between δ_0 and F_a at various field strengths.

3.4 Potential Energy Model

In section 3.3 the deformation of a piezoelectric laminate is shown as a function of the applied voltage. However, when the laminate is not able to attain this strain state due to counteracting forces or moments, part of the strain is exchanged for applied stress. This section will show how the amount of applied stress and the amount of strain are related. To obtain this relation a so-called semi-analytical approach is followed, after De Breuker (section 4.1.4 in [8]).

To describe the state of the laminate the theory of minimum potential energy is used. Potential energy consists of internal (U) and external (V) energy (eqn. (4.37) in [8]):

$$\Pi = U + V \tag{3.48}$$

Where the internal energy is defined as (eqn. 4.37 in [8]):

$$U = \int_V \sigma d\epsilon \tag{3.49}$$

For a symmetric beam that is bent and actuated by the piezoelectric elements, the internal energy expands to:

$$U = \frac{1}{2}\int_0^L (N\epsilon + M\kappa)dx - \int_0^L B_a \Lambda \kappa dx \tag{3.50}$$

External energy is generated by any force or moment that causes a deflection or rotation in the beam. Using the PBP actuators in a morphing wing means that they will be be used in a cantilevered configuration. In the previous sections the results for the simply supported adaptive beam are directly applicable to the cantilevered beam. Since this section is also concerned with resistive forces and moments (as opposed to the previous sections), the cantilevered beam will behave differently from the simply supported one. A cantilevered beam is considered, being precompressed by a force F_a, on which a tip force F_t is exerted (compare figure 3.7). For this case the external energy is expressed as:

$$V = -F_a(\sqrt{(L+u)^2 + w^2} - L) + F_t w \tag{3.51}$$

Figure 3.7: Two applied forces on a cantilevered beam.

For a structure to be in equilibrium the virtual work done on the structure equals zero. Assuming that F_a and F_t are both conservative forces, the virtual work is equivalent to the first variation of the potential energy. Using Hamilton's principle, the first variation of the potential energy is zero:

$$\delta\Pi = 0 \tag{3.52}$$

This equation is solved numerically. One of the results is a relation between the tip force, F_t, the precompressive force, F_a, and the free strain of the actuator, Λ. Since Λ is linearly related to the voltage, via equation 3.2, it is now possible to show a relationship between tip force, F_t and the tip deflection, w, at a constant voltage level. This relationship is shown in figure 3.8. These figures give an overview of different force deflection-curves at a constant voltage of $100V$ (3.8-a), and constant precompression force of $0.9F_b$ (3.8-b). Where F_b is the buckling load of the actuator.. This data is obtained for a 15 mm wide specimen with a length of 72.4 mm (standard length of PZT sheet) [8].

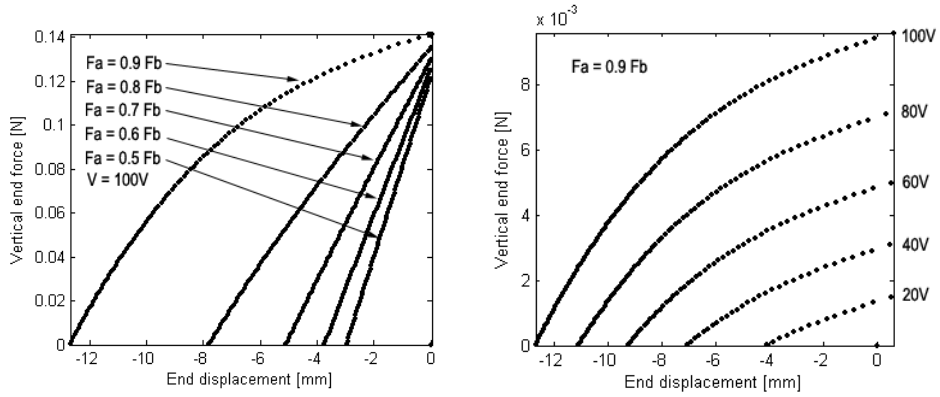

(a) At constant voltage of $100V$. (b) At constant axial force of 0.9 F_b.

Figure 3.8: Vertical end force versus tip deflection

3.5 PBP Experiments and Results

To show that the modeling of the PBP actuator is accurate, the results shown in figure 3.6 are to be compared to practical measurements. These measurements were taken in the spring of 2004 and are laid out in [18]. Figure 3.9 shows the wired test actuator and the experimental setup that was used to determine the precompression force, F_a, and the end rotation, δ_0. To measure F_a, the actuator is placed on a scale. By screwing down the top bar, this force can be adjusted. A laser beam is used to magnify the end rotation so it can be read accurately from a screen (not displayed). A more detailed description of the test setup can be found in [18]. The dimensions of the test specimen are displayed in figure A.1 in appendix A.

Using this experimental setup a series of experiments were carried out. Eight different specimen were tested successfully. The result of one of the specimen is displayed in figure 3.10. The experimental values in this graph are close to

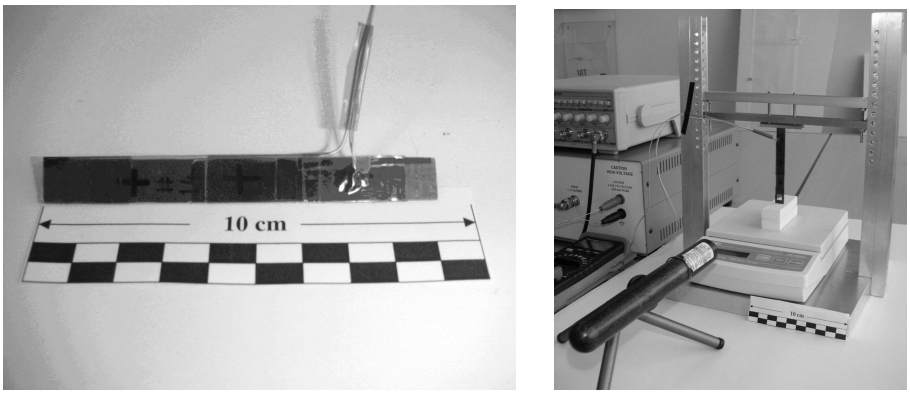

Figure 3.9: Actuator and experimental setup [18].

the predicted values, indicating that the model as laid out in section 3.3 gives a good representation of the behavior of a PBP piezoelectric actuator. The discrepancies between the two plots are the result of the assumption that the total laminate length is covered by the PZT laminate, while in reality the end parts are glass fibre reinforced epoxy. Figure 3.10 shows that curvatures can be magnified up to a factor of four, when precompression is applied. Furthermore, this figure shows that the buckling load for this specimen is found between 550 and 600 $[gmf]$, which translates to $55 - 60$ $[gmf/mm]$.

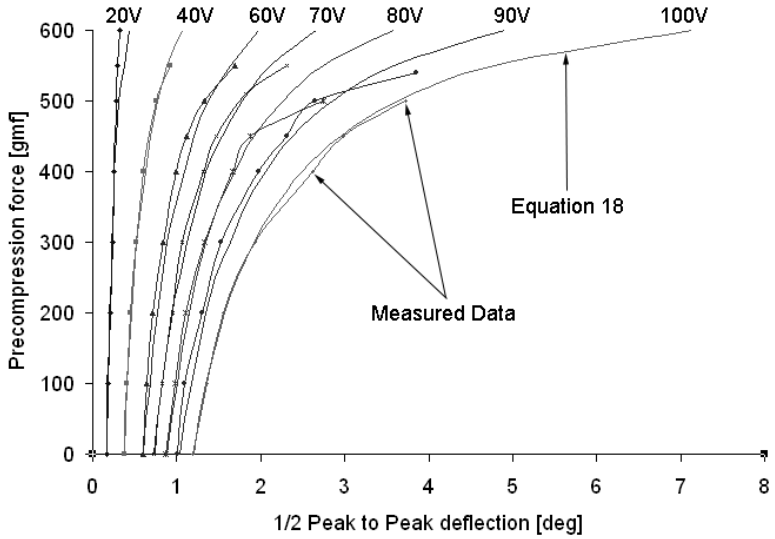

Figure 3.10: Correlation of deflection angle, δ_0, applied voltage and axial force, F_a.

Maximum Curvature To find out at what curvatures the specimen fails a destructive experiment is carried out. This is done by means of a three point pressure test. A simply supported specimen (length= $40mm$, width= $12\ mm$, thickness= $0.66\ mm$, cure temperature= $176°C$) is being deflected by a point force, acting at the center. Figure 3.11 shows the destructive test set-up. The load is introduced using a small vise. A laser beam is reflected by a mirror at the end of the specimen and projects onto the reflection board from which the rotation can be determined. To determine when a crack is formed the resistivity over the tensioned face is measured by a voltmeter. When the resistivity suddenly increases orders of magnitude, this would indicate the element has cracked.

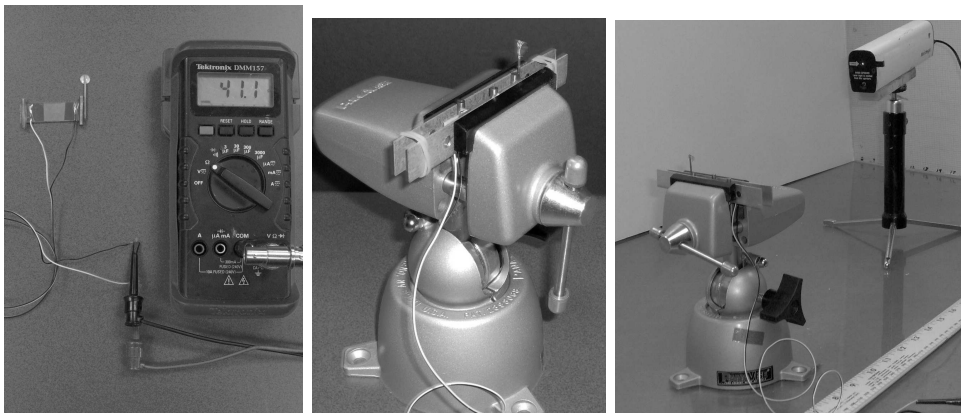

(a) Resistivity measurement (b) Specimen in vise (c) Total set-up with laser

Figure 3.11: Destructive experiment to determine maximum rotation.

The test shows an increase in tip deflection of 5.4 degrees. Since this is a simply supported set-up and only small rotations are present, the curvature of the specimen is prescribed by:

$$\kappa = \frac{2\delta_0}{l} \tag{3.53}$$

In equation 3.53 l denotes the length of the specimen and δ_0 denotes the deflection angle as presented in Figure 3.5. The length of the specimen amounts to 40 mm. Substituting both values into equation 3.53 gives a maximum curvature of $0.27°/mm$. A 72 mm long simply supported specimen should be able to handle a peak to peak deflection of 19.4°. Translating this to a clamped specimen, would give a maximum peak to peak tip deflection of 38.8°.

Note that the values are only applicable for actuator laminates that are cured at $176°C$. Lower temperatures will induce less internal precompression of the

PZT sheets. Accordingly, the sheets will break at lower curvatures. To make a robust actuator it is therefore important to cure at high temperatures.

3.6 Integration and Comparison

Significant benefits are obtained by switching from conventional electromechanical servo actuators to PBP actuators. They do not employ any linkages, gears, or heavy motors, and are therefore significantly lighter. Since PBP actuators operate under a high voltage but very low current, power consumption is decreased dramatically [7]. This in turn leads to a reduction in battery capacity and consequently battery weight. Section 6.1 will go more into detail about power consumption. Contradictory to conventional servo actuators, the PBP actuator is solid state so part count, slop and deadband are one to two orders of magnitude lower [3]. Moreover, using a PBP actuated morphing wing can increase the actuation frequency by an order of magnitude, with excellent control authority. Table 3.1 shows how PBP actuators compare to conventional electromechanical servo actuators used for identical actuation purposes [3].

	Conventional Servoactuator	PBP Actuator
Max Power	24W	100mW
Max Current	5A	1.4mA
Mass	108 g	14 g
Slop	1.6°	0.02°
Corner Frequency	3 Hz	34 Hz
Part Count	56	6

Table 3.1: Comparison of electromechanical servo actuator and PBP actuator [3].

An additional benefit of these type of solid state actuators is the fact that the actuator can form an integral part of the structure. Therefore, the weight of the actuator is not added to the structure, but could already be perceived as part of the structural weight. By introducing axial loads in a simple way, complexity can be greatly reduced. The following two chapters will go more into detail about how a PBP piezoelectric actuator can be integrated into the wing of an aircraft and be used to induce control.

3.7 Synopsis

This chapter has presented the basic principles and model of a post-buckled precompressed (PBP) piezoelectric bending actuator. It has been shown

how piezoelectric strain is related to the atomic structure of the material and and how a piezoelectric bender actuator is actuated by applying a voltage difference over the individual piezoelectric elements. Classical Laminated Plate Theory has shown to capture the behavior of the unloaded bender element really well. A Newtonian model has been developed to predict curvatures of the axially loaded PBP actuator. Experiments showed good a correlation with this model. It has been shown that by applying an axial load, curvatures can be magnified up to a factor of 4. A comparison between a conventional servo actuator and a PBP actuator has shown that power consumption, slop, dead band, part count and weight are all substantially lower for the PBP actuator, while at the same time the corner frequency is increased.

Chapter 4

Thin Wing Design, Fabrication and Testing

This chapter will show how a PBP actuator can be integrated in a wing and be used to change its camber and consequently control the aircraft. This chapter starts off with a set of requirements that are imposed on the design. The following section will give an overview of all the important features of the wing, their function and their dimensions. Also, the performance characteristics of the airfoil are investigated. The design and fabrication of the wing are presented in the two subsequent sections and this chapter ends with a section on bench testing and a section on wind tunnel testing.

4.1 Application and Requirements of a Morphing Wing

Integrating PBP piezoelectric actuators into a morphing wing configuration has not been done before. The main goal of this project is to show that a morphing wing can induce control successfully. Applications of a (partly) morphing wing can be various. Deforming wing parts could for instance replace conventional ailerons or flaps for small UAVs. They could be applied on the entire wing or just on a small part. In this chapter it is assumed that a morphing wing is to be used on a subscale UAV (span 0.5 m) in order to supply it with roll control and direct lift control.

The requirements on the aircraft mission are partly drawn from an annual MAV contest that is held in the US. The flight time of the aircraft must be 10 minutes, its ceiling 100 meters and an average cruise velocity of 15 m/s. Furthermore it must be capable of carrying a small camera that takes pictures at regular intervals. The stall speed may not be lower than 7 m/s,

which makes it possible to throw the aircraft manually to have it take off. The maximum take off weight amounts to 300 grams [31].

From these requirements it can be easily established that each of the wings must supply the aircraft with approximately 1.5 N of gross lift (without being actively deformed). Since no specific aircraft is yet available to fly with this new wing, no performance calculations of the aircraft as a whole can be made.

4.2 Airfoil Design

4.2.1 Airfoil Geometry

A small deformable wing with a static gross lifting capability of 1.5 N is to be designed. To supply the wing with both lift control and roll control, it is decided to divide each of the wings into two individual panels. The inboard panels for lift control and the outboard panels for roll control.

From section 2.4 it is known that a low Reynolds number airfoil should be thin ($t < 0.05c$) and that a slight cambering is beneficial (approximately 4%) The leading edge of the airfoil should be relatively sharp, while the trailing edge geometry does not significantly alter the pressure distribution [19]. Furthermore curvature on the leading edge may not be too large with respect to the size of the laminar separation bubble (confer section 1.4).

What makes this airfoil design different from all the other airfoil designs, is of course the bimorph piezoelectric element (cf. figure 3.9 (a)). From the trade study between the UAV and the MAV (section 2.3) it has become clear that using the bimorph to directly influence the flow is most efficient. No losses in structural deformation of a thick airfoil occur. The camber line virtually forms both top and bottom face of the profile. This is the most important constraint on the geometry. Furthermore, a bimorph, uncharged, is basically a flat plate.

Combining the desired shape with the constraints of the bimorph laminate, yields an airfoil with an aerodynamically shaped leading edge and a flat plate behind it. How the aerodynamic shape should look like is part of an aerodynamic study, which is shown later in this section. For now, figure 4.1 gives a generic view of how the airfoil should look like, when the bimorph is uncharged. This airfoil will be referenced to as the "thin airfoil".

As shown in figure 4.1 the geometry of the airfoil is fixed for 70 to 80% of the airfoil. This part is just a flat plate (in uncharged condition). The remaining part (the leading) edge has to be shaped in such a way that it gives an as high as possible lift coefficient. To calculate this analytically is a laborious job, so the panel code Xfoil is used. This panel code is based on potential flow

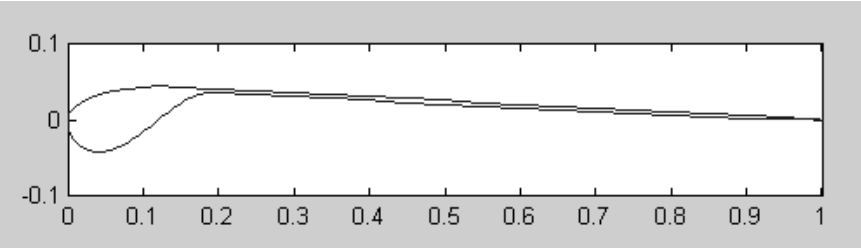

Figure 4.1: Geometry of the airfoil.

in combination with the Kutta condition but is able to incorporate viscous effects. The boundary layers and wake are described with a two-equation lagged dissipation integral boundary layer formulation and an envelope e^n transition criterion [25]. Xfoil is able to calculate pressure distributions over airfoil sections, determine the aerodynamic coefficients, and give an impression of boundary layer development over the airfoil. It incorporates viscous effects in the boundary layer and also includes the Reynolds number. On the other hand, it is not able to incorporate three dimensional effects like tip vortices. It must also be noted that with Reynolds numbers lower than 200.000 Xfoil results must be interpreted as an indication rather than an exact simulation of reality. Wind tunnel tests are the only way to determine the true characteristics of a low Reynolds number wing.

In appendix C it is explained how the basic geometry of the leading edge is defined by using simple geometric shapes. By using the appropriate boundary conditions (Reynolds number of 10^5 and a velocity of 15 m/s) it is then possible to alter the shape within certain physical constraints. This way numerous of different shapes are examined in Xfoil. The airfoil is examined in uncharged condition, meaning that 70-80% is flat. The leading edge geometry that produces the highest lift coefficient at zero angle of attack, is the one that is most suited. Excessive values of the drag coefficient would also indicate that a particular shape is not desirable, however the lift coefficient in cruise condition is dominant.

A number of iterations of the shape finally indicated that the shape presented in figure 4.2 performed best. A lift coefficient of $C_l = 0.25$ is the largest value, obtained at zero angle of attack. From figure 4.2 it can be seen that this airfoil has a rather small nose radius and is therefore fairly sharp. On the other hand, the top side of the leading edge has little curvature because it is quite stretched. The flow will therefore remain attached more easily, also at larger angles of attack.

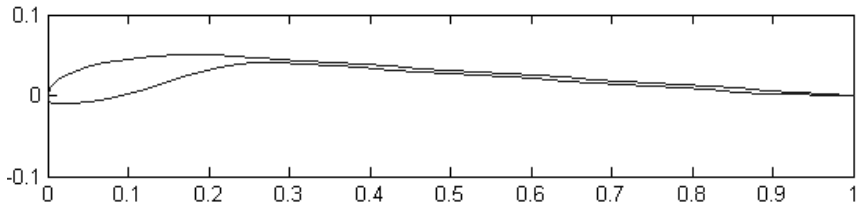

Figure 4.2: Airfoil with highest C_l at $\alpha = 0$.

4.2.2 Predicted Static Performance of Thin Airfoil

This section will investigate the predicted performance of the airfoil in terms of lift, drag and moment coefficient. Besides the normal effect of the angle of attack on these coefficients, the influence of morphing is of particular interest. To express the amount of morphing the trailing edge deflection is measured. Figure 4.3 shows how the deflection of the tip is converted to the angle δ. Angle δ corresponds with δ_0 in figure 3.5. The graphs in this section are produced using Xfoil.

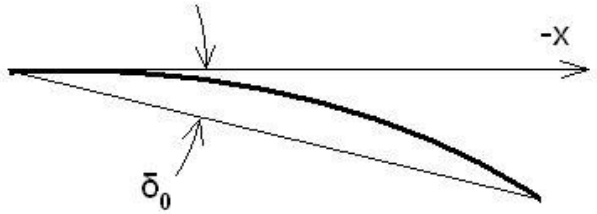

Figure 4.3: Definition of the angle δ_0.

Opposite to the simple supported beam in section 3.3, in this case the bimorph is clamped to one side at the leading edge. As shown in section 3.3, δ_0 is determined by the amount of curvature κ. By changing the curvature the airfoil shape is changed subsequently. In this section $delta_0$ is shortened with δ, for convenience. It is assumed that the maximum value of δ amounts to +/-6°. The two most pronounced shape deformations are displayed in figure 4.4.

An angle of attack sweep, ranging from 0 to 15 degrees is carried out. Using Matlab, the curvature is altered for each airfoil configuration. Between maximum and minimum curvature seven different deflections are examined with a step size of 2 degrees. The results of all the calculations are presented in figures 4.5 to 4.7.

Figure 4.5 shows the change in lift coefficient with the deflection of the

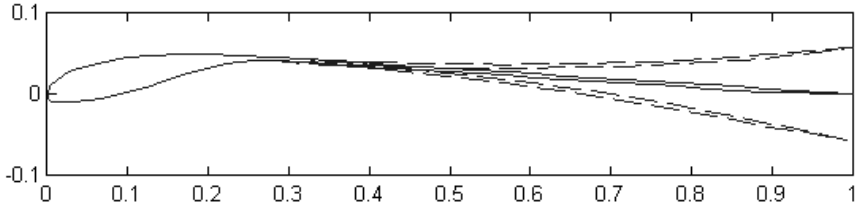

Figure 4.4: Maximum downward and upward deflection.

airfoil. As can be seen from the graph, C_l varies linearly with the deflection. At zero angle of attack $C_{l_\delta} = 7.95$ $[1/rad]$. For higher angles of attack C_{l_δ} only declines a little to 6.58 $[1/rad]$ at $\alpha = 8°$. Finally, note that some of the points are not lined up with the rest. This indicates that Xfoil is not capable to produce a closed solution at that specific condition.

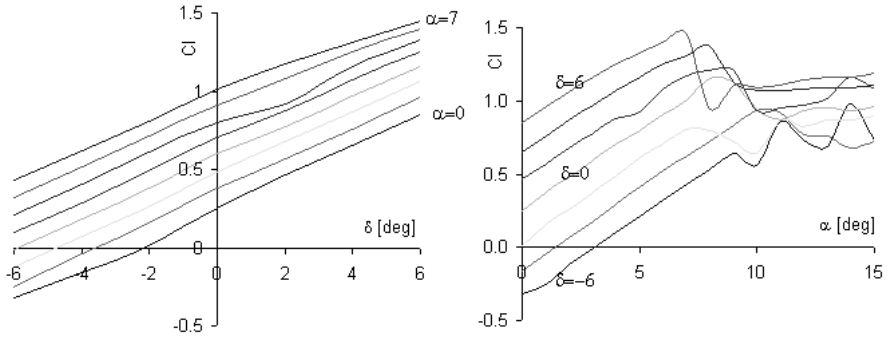

(a) Predicted C_l vs. δ (b) Predicted C_l vs. α

Figure 4.5: Lift coefficient as a function of δ and α.

Contradictory to the lift coefficient, the drag coefficient does not show a linear behavior with the tip deflection (compare figure 4.6-a). Moreover, the curves also differ in shape at different angles of attack. It can generally be seen that at small angels of attack ($\alpha < 4°$) C_{d_δ} is negative, but decreasing with deflection. For larger angles of attack ($\alpha > 4°$) C_{d_δ} appears to be positive, and increasing with deflection. Consequently, two totally different ways of behavior for small and large angles of attack. Note that for $\alpha = 4°$ the drag coefficient is approximately constant for every deflection angle. As can be seen from figure 4.6-b the drag rise due to separation starts at lower angles of attack for higher deflection angles.

The moment coefficient (point of application = quarter chord point [25]) as a function of angle of attack, α, and deflection angle, δ is presented in Figure 4.7. The moment coefficient shows a negative linear trend with increasing

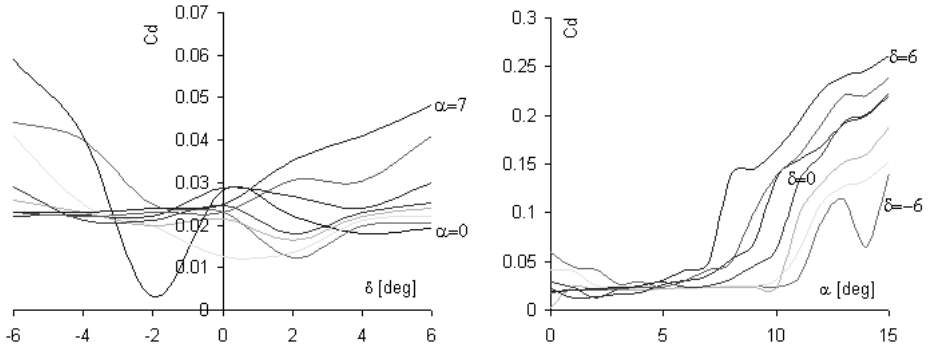

(a) Predicted C_d vs. δ (b) Predicted C_d vs. α

Figure 4.6: Drag coefficient as a function of δ and α.

deflection angle. From Figure 4.7-a it can be seen that for higher angles of attack C_{m_δ} becomes a little less ($C_{m_\delta} = -0.57$ $[1/rad]$) At zero angle attack C_{m_δ} amounts to -0.82 $[1/rad]$. Figure 4.7-b shows that the moment line at various deflection angles is relatively flat up to 8 degrees angle of attack.

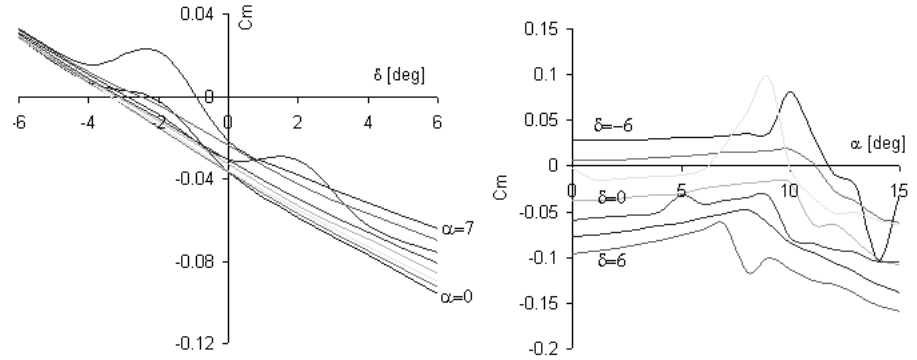

(a) Predicted C_m vs. δ (b) Predicted C_m vs. α

Figure 4.7: Moments coefficient as a function of δ and α.

In conclusion, this paragraph will repeat the most important features of this airfoil. $C_{l_{max}} = 0.9$ at zero angle of attack; at maximum deflection $C_{l_{max}} = 1.45$; $C_{l_\delta} = 7.95$ $[1/rad]$ for zero angle of attack; C_{d_δ} is negative up to $\alpha < 4°$, at higher angle of attack it is positive. At $\alpha = 4°$ C_{d_δ} is constant for all delta. C_{m_α} is fairly constant at various values of δ up to 8° angle of attack.

4.3 Wing Design

4.3.1 Preliminary Design

Now that the airfoil shapes are more or less determined, the layout of the total wing is considered. The wing should be able to perform both roll control and direct lift control. Also, each wing should supply 1.5 N of lift during cruise ($V = 15\ m/s$) in order to carry the aircraft. Most desirable would be a wing with a continuously variable spanwise camber distribution. This is practically what a bird does with its wings when it is soaring. The inboard part of its wing remains at a constant camber, while at the tips the shape is altered constantly to manoeuvre. Between the tip and root of the wing a continuous change in camber can be observed.

The question is whether this is also possible for this MAV wing. A bird uses its feathers to slide over each other when the wing morphs. To mimic this in a mechanical wing would be very difficult. One must consider that the airfoil shape is already established (compare previous section). It would be possible to divide the wing in spanwise direction into a finite number of panels. Each panel would than independently of the rest change its camber. A semi-continuous spanwise camber change could then be achieved.

The PBP actuator requires a tool to pre-compress the PZT laminate. In the thin wing concept this force is easily applied by using a rubber band at either side of each wing panel (compare figure 4.8). This compression mechanism is described in [2]. This implies that the wing will not have a continuous cross section but will have gaps to store the rubber bands. The gaps will increase induced drag and profile drag. It is therefore decided that the wing is divided into two spanwise panels, which each can be operated separately. The inboard panel will be used for direct lift control, while the outboard panel induces roll control.

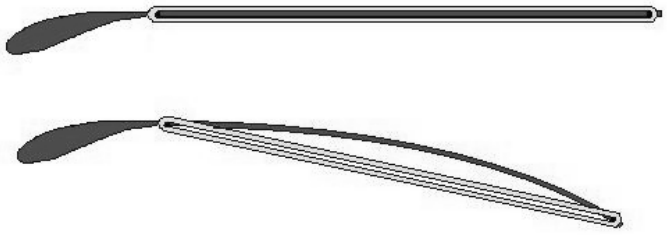

Figure 4.8: Compressive force by a rubber band.

Figure 4.9 shows an impression of the wing and all the components it consists of. The total wing area amounts to $2.64 \cdot 10^{-2}\ m^2$.

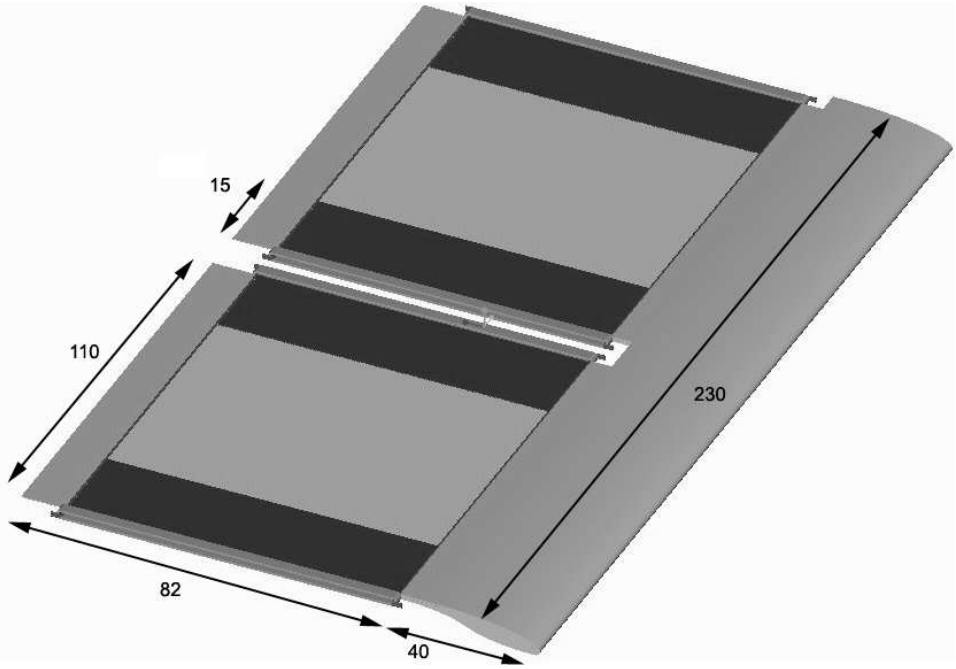

Figure 4.9: 3D image of the wing lay-out (all dimensions in mm).

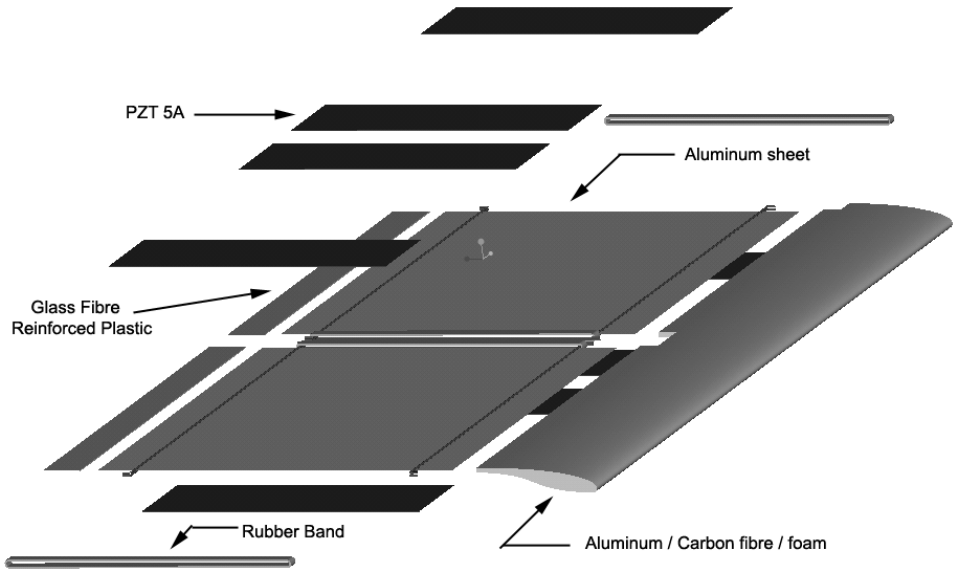

Figure 4.10: Exploded view of the wing.

Figure 4.10 also suggests the materials to be used in the wing. The leading edge is fabricated out of foam, covered with thin Aluminum sheet. Spanwise rigidity is increased due to the application of unidirectional carbon fibres that are laminated in between the foam core and the Aluminum. The trailing edges of the wing are also fabricated out of this material. The relatively large width of the trailing edges (10 mm) is necessary to ensure that the load introduction on the piezoelectric elements (PZT, in figure 4.10) is constant over the width of the specimen (compare appendix D for trailing edge structural analysis).

The substrate material, that is used between the bimorph PZT, is extended throughout the wing panel. The substrate is a thin Aluminum sheet (3/4 hard Al 1018) of 0.078 mm thickness. It is a relatively tough material and because it is so thin it is very flexible. The additional weight to the total wing will be less than 2 grams, so it is light as well. Moreover, because it is supported by the frame, it will be able to carry the aerodynamic loads. Another advantage is that the wing panel can be produced more easily. The substrate/foil is used as base material. The PZT specimen and the trailing edge can simply be attached to it.

The complex interaction between aerodynamic loads on the panel and the panel deflection, make it hard to analytically determine the combination of end force and deflection. For practical reasons it is therefore chosen to give each piezoelectric actuator a width of 15 mm. From figure 3.10 it can be deduced that the buckling load for such an element will be between 800 and 900 gmf. Available rubber bands have shown a compressive force between 250 and 300 gmf, at the required elongation. This would mean three rubber bands should be able to give the required precompression. Increasing the width of the elements means more rubber bands are needed, which can be obstructive and require stronger (heavier) attachment points.

4.3.2 Lift Distribution

The simplest way to design a wing from the airfoil is just adding a third dimension, yielding a straight wing with no in change section geometry in spanwise direction. To a certain extend this can be applied to the wing sketched in section 4.3. The wing is straight: no taper, sweep or twist is present. There are, however, discontinuities in the form of gaps between the wing panels (compare figure 4.9).

The effect of the gaps on lift is uncertain. The gaps will allow air from below the wing (high pressure) to flow to the top side of the wing (low pressure). As a result a vortex is produced over the each of the wing panels. Figure 4.11 gives a schematic impression of this phenomenon. The vortices between the panels are similar to the tip vortices which are present at all regular aircraft.

In general tip vortices cause a loss in lift, because the negative pressure on top of the wing is reduced by the flow over the wing tip [23]. However, investigation in low Reynolds number, low aspect ratio wings shows that tip vortices are not always detrimental for lift [22].

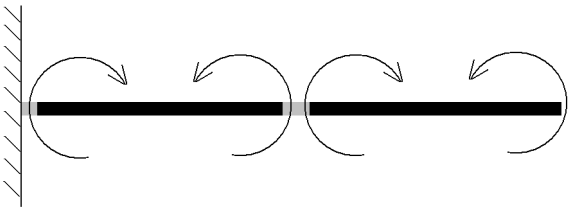

Figure 4.11: The gaps cause additional vortices over the wing.

A way to mimic the influence of the gaps between the panels is by assuming that one panel can be treated as a separate wing. In this assumption, the continuity of the leading edge of the wing is neglected. The aspect ratio of a wing is defined as follows:

$$A = \frac{b^2}{S} \tag{4.1}$$

The dimensions of one panel are $b = 11$ $[cm]$, $S = b \cdot c = 12 \cdot 10 = 120$ $[cm^2]$. Substituting these values in equation 4.1 yields an aspect ratio of 0.92. Investigation has shown that for a wing with aspect ratio 1 and a Reynolds number around $8.5 \cdot 10^4$, the tip vortex causes an increase in lift near the tip of the wing. Theory behind this increase is the disappearance of the separation bubble, due to energizing of the local boundary layer. The effect increases with increasing angle of attack [22].

Beside an increase in lift near the tip of the wing, the vortices also induce an off-elliptical lift distribution, meaning more induced drag. The exact influence of the gaps is very hard to predict at this stage. Wind tunnel experiments are required to establish this. To calculate some effective forces over the individual panels it is assumed that the lift distribution in spanwise direction is constant and equals that of the airfoil C_l (compare figure 4.12).

From the assumption of constant lift distribution, the required lift coefficient can be determined. The lift coefficient can be altered by changing the angle of attack or by changing the deflection of the adaptive laminates (or a combination). Accordingly, for every lift coefficient there will be a range of combinations of angle of attack and deflection angles. At cruise condition, the required lift is 1.5 N and the lift coefficient is given by equation (4.2)[21]:

$$C_L = \frac{2L}{\rho V^2 S} \tag{4.2}$$

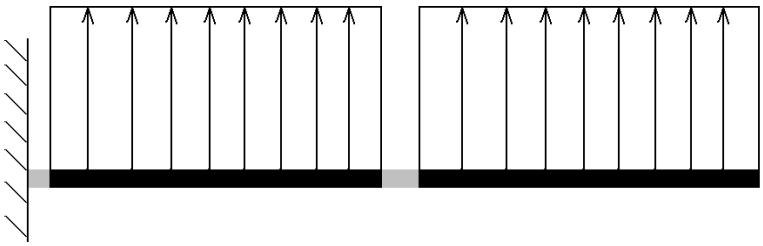

Figure 4.12: The assumed spanwise lift distribution.

Substituting for the total wing area, $S = b \cdot c = 0.22\ [m] \cdot 0.12\ [m] = 0.0242\ [m]$, the required lift coefficient, $C_L = 0.41$. This means that an angle of attack of 1.5° is needed at zero deflection. At zero angle of attack, a deflection of 1.4 degrees is required to attain the same lift coefficient (cf. figure 4.5).

4.4 Fabrication

4.4.1 Leading Edge Fabrication

Manufacturing the thin wing will be divided into two distinct parts: the leading edge part and the adaptive part. This section will describe how the leading edge is made. The cross sectional width of the leading edge is 31 mm, the height amounts to 8 mm (compare figure 4.13). The length of the leading edge amounts to 230 mm.

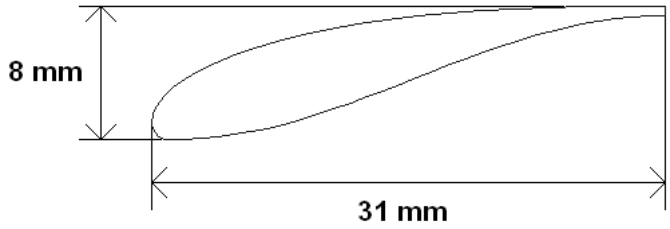

Figure 4.13: Dimensions of the leading edge.

The leading edge is fabricated as a sandwich structure. It consists of a foam core with an aluminum sheet attached to it. To give the laminate additional stiffness, unidirectional fibres are positioned at the thickest point between the aluminum sheet and the core. This requires that the shape of the core matches exactly the shape of the leading edge itself. This can be done fairly simple by cutting the foam with a hot wire. To attach the aluminum sheet

in the concave part of the leading edge vacuum must be applied during the curing of the adhesive (compare figure 4.14).

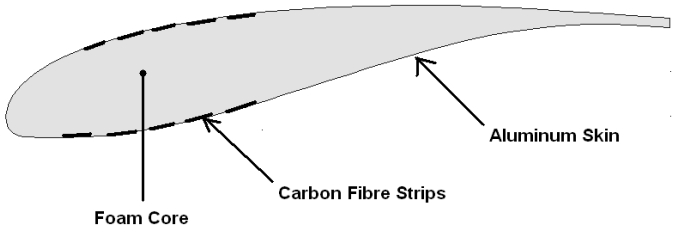

Figure 4.14: Leading edge materials.

To save weight it would be best to keep the aluminum skin as thin as possible. The thinnest plates at hand are the same sheets that are used as substrate materials for the PZT's. These measure a mere 0.0762 mm in thickness. To prevent the leading edge from buckling additional unidirectional carbon fibres are applied between the foam and the aluminum around the thickest location of the wing.

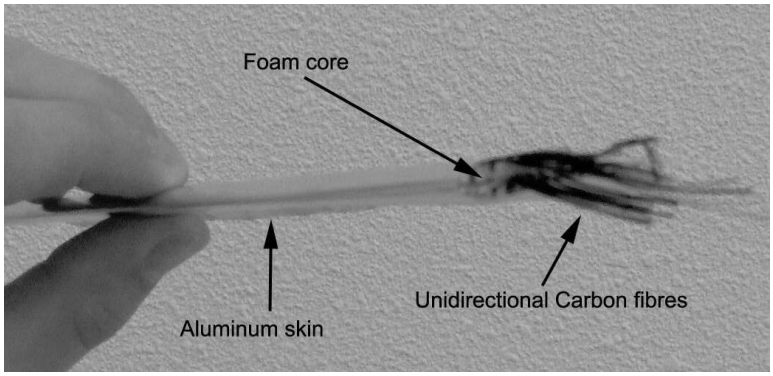

Figure 4.15: Leading edge.

4.4.2 Actuator Fabrication and Integration

The actuator and the aft part of the wing are one integrated part. A wet lay-up is used to attach the PZT elements onto the Aluminum substrate (figure 4.17). The trailing edge on the wing consists of a glass fibre reinforced plastic layer on the top and bottom of the aluminum substrate. The trailing edge covers the last 10 mm of the wing and is made a little wider than the individual wing panels such that the rubber bands can be easily attached later.

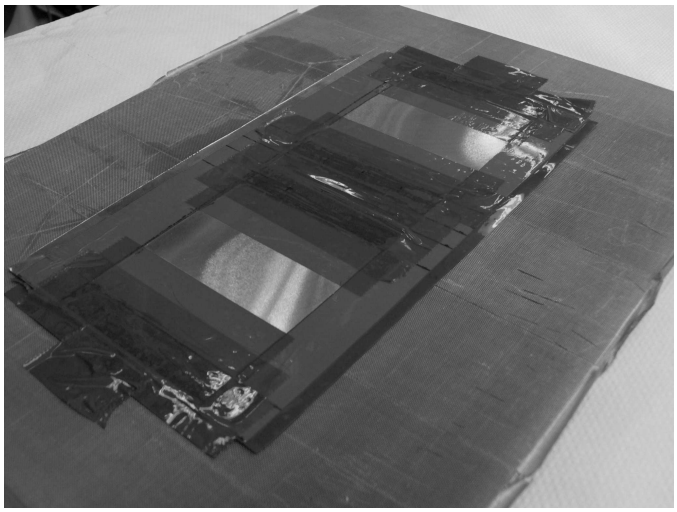

Figure 4.16: Actuator lay-up on caul plate right before cure.

The wires to connect the PZT sheets are integrated in a narrow band of glass fibre reinforced plastic that touches the foam of the leading edge. Integration of the leading edge and the deformable panels is done by affixing them to the aluminum sheet of the leading edge. A slight deviation from the original design was made by omitting the steel rods to hook the rubber bands to. Instead, the glass fibre at the trailing edge and near the leading edge is used to put the rubber bands around. Figure **??** shows the entire wing, including the rubber bands.

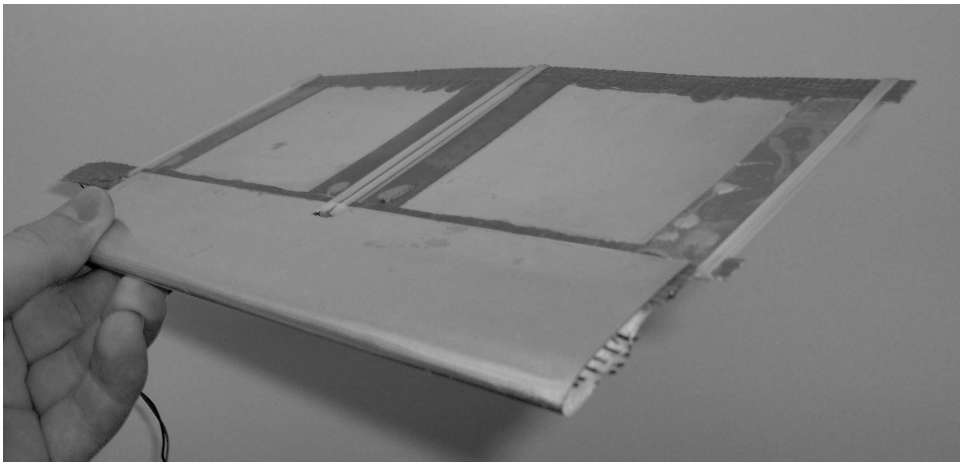

Figure 4.17: Total wing lay out.

4.5 Static Bench Testing

Static bench tests were carried out to determine the deflections of the wing. Since the wing consists of two individual panels, each of the panels was tested individually. End rotations of the trailing edge are measured by reflecting a laser off the trailing edge onto a reflection board. The experiments are done statically, meaning voltage is constant during each measurement. Figure 4.18-a shows the experimental test setup.

To achieve the right amount of precompression, a combination of two different kinds of rubber bands is used. Each panel is being compressed by two sets of rubber bands, each set consisting of three rubber bands: two orthodontal high quality elastics and one ordinary 'desktop' rubber band. Each set provides 800 gmf of precompression, which is just below the expected buckling load ($825 - 900$ gmf).

Two sets of experiments were undertaken. The first one involving only the unloaded actuators, the second one with axial loading of the elements, introduced by rubber bands. Figure 4.18-b shows the end rotation of the elements as a function of the applied voltage. It can be seen that by applying the precompression end rotations are almost doubled, up to 13.6 degrees peak to peak at 95V.

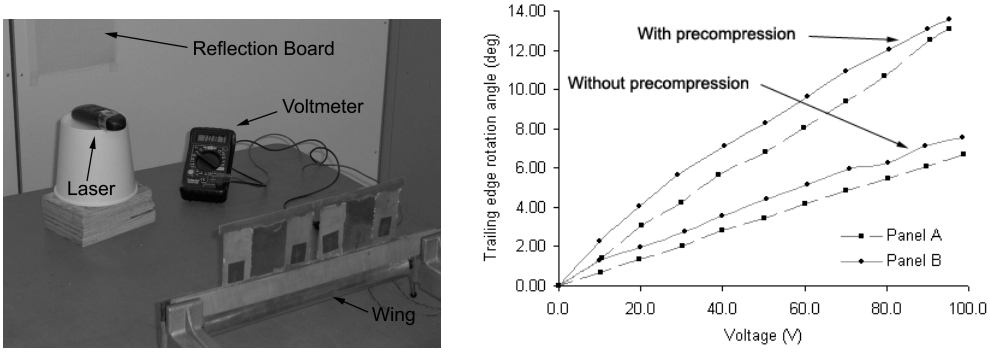

(a) Bench test setup

(b) Static end rotations as a function of voltage.

Figure 4.18: Bench test experiment set-up and results

4.6 Wind Tunnel Tests

4.6.1 Lift Curve Slope

In order to verify the lifting capability of the wing in an early stage, a static test article was fabricated. This wing has the exact same geometry as the

designed wing, but does not employ the piezoelectric actuators. Instead, copper substrates of the same dimensions as the actuators are used as surrogates. The wing was hinged and put into an open wind tunnel. During the wind tunnel tests the angle of attack and the velocity were measured. The wing could rotate freely about the hinge point. Figure 4.19 gives a schematic overview of the wing in the airflow and all the forces and moments that are acting on it.

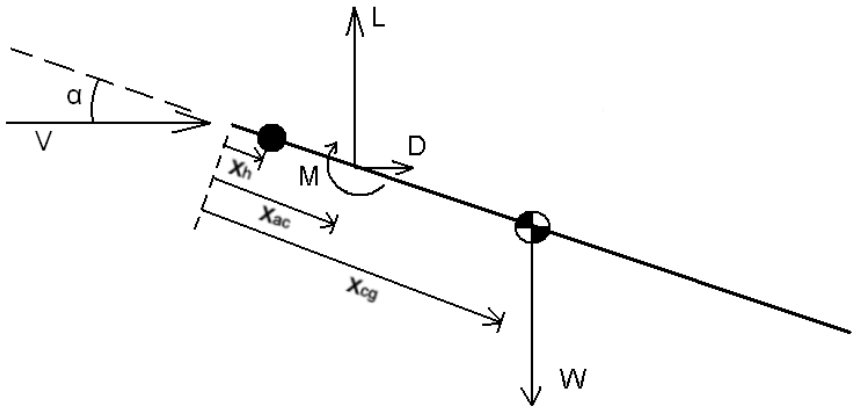

Figure 4.19: Schematic representation of forces on the wing.

The wing's center of gravity (cg) had been determined beforehand. The aerodynamic center (ac) was assumed to be positioned at a quarter chord and also the hinge point (h) was measured in accurately. Since the wing is hinged freely, the air velocity will determine the angle of attack of the wing. The moment balance around the hinge point can be written as:

$$\begin{aligned} 0 &= M_{ac} - L(x_{ac} - x_h) - D(x_{ac} - x_h)(\alpha - \alpha_0) + W(x_{cg} - x_h) \\ &= C_M qSc - C_L qS(x_{ac} - x_h) - C_D qS(x_{ac} - x_h)(\alpha - \alpha_0) + mg(x_{cg} - x_h) \end{aligned} \tag{4.3}$$

In equation (4.3) it is assumed that only small angles of attack are attained, implying $\cos\alpha = 1$ and $\sin\alpha = \alpha$. Remembering that $C_L = C_{L_\alpha}(\alpha - \alpha_0)$, and assuming that $C_D << C_{L_\alpha}$, equation (4.3) can be rearranged to:

$$\frac{1}{q} = -\frac{C_m Sc + C_{L_\alpha} S(x_{ac} - x_h)\alpha_0}{mg(x_{cg} - x_h)} + \frac{C_{L_\alpha} S(x_{ac} - x_h)}{mg(x_{cg} - x_h)}\alpha \tag{4.4}$$

This equation can be written as:

$$\frac{1}{q} = \eta + \xi\alpha \tag{4.5}$$

With:

$$\xi = \frac{C_{L_\alpha} S(x_{ac} - x_h)}{mg(x_{cg} - x_h)} \tag{4.6}$$

Rewriting this for C_{L_α} results in:

$$C_{L_\alpha} = \frac{mg(x_{cg} - x_h)}{S(x_{ac} - x_h)} \xi \tag{4.7}$$

All the terms on the right hand side of equation (4.7) are either known, or measured during the wind tunnel tests. As is shown in figure 4.20-b, the inverse of the dynamic pressure, q is linearly related to the angle of attack, α. The slope of this line is $\xi = 0.1345$. Furthermore, $x_{ac} = 0.0340$ $[m]$, $x_{cg} = 0.0692$ $[m]$, $x_h = 0.0130$ $[m]$, $m = 0.032$ $[kg]$, $S = 2.97 \cdot 10^{-2}$ $[m^2]$ and $g = 9.81$ $[m/s^2]$. Substituting this in equation 4.7 yields:

$$C_{L_\alpha} = 3.80 \ [1/rad]$$

These wind tunnel tests have shown qualitatively that the wing geometry does induce lift and that attached flow is present up until an angle of 15°. Figure 4.20-a shows a picture of the hinged wing during the wind tunnel tests.

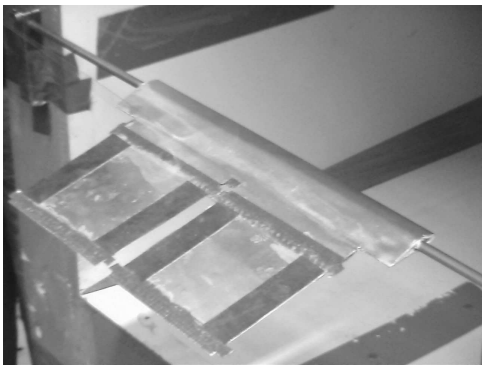

(a) Static wing in wind tunnel

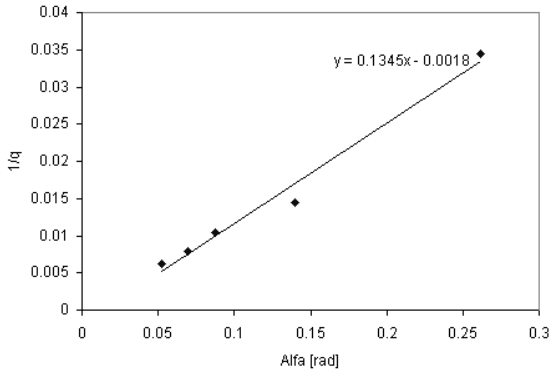

(b) Relation between the dynamic pressure, q, and the angle of attack, α

Figure 4.20: Wind tunnel experiment set-up and results

4.6.2 Lift and Drag Measurements

The static test article gives a good indication of the behavior of the wing under a range of angle of attacks. To determine the actual lift and drag forces a set of nine static wing articles are fabricated. Each of the test articles has an identical leading edge. However, they each exhibit a differently curved

rear part. The curvatures each represent a tip rotation of respectively 0, 2.5, 5, 7.5 and 10 degrees (both positive and negative), which translates to a deflection of +/-5° in steps of 1.25° (cf. figure 4.21-a). The static tests have shown that the maximum peak to peak end rotation of the wing is close to 14° peak to peak (cf. figure 4.18), which translates to a maximum deflection of +/-3.5°. Actuator improvement might lead to even higher curvatures, so it is therefore chosen to measure beyond this maximum value of deflection. Deflection is defined in figure 4.3 and is denoted here with δ, for convenience.

Tests are performed in the Low Speed Wind Tunnel of the TU Delft. The wing is positioned on a rotating part of the top wall of the wind tunnel. Due to the presence of this wall, a half model of the total wing is simulated. Since the test article is only one of the two wings for the MAV, this setup is a good estimation of what happens during actual flight. A picture of the test setup is shown in figure 4.21-b.

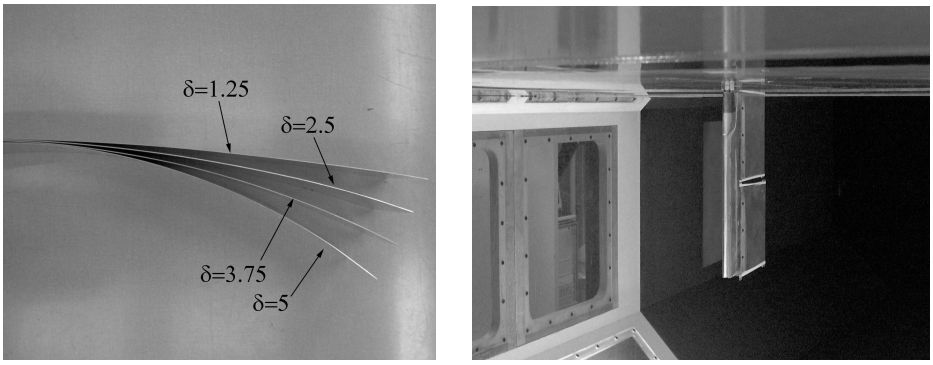

(a) Set of deflections for aft part of wing

(b) Experimental setup of wing in wind tunnel

Figure 4.21: Static deflections and wind tunnel setup.

Measurements were taken at an average airspeed of 15 m/s, at a Reynolds number of $1.24 \cdot 10^5$. At each deflection a angle of attack sweep was carried out in steps of 1° between $\alpha = -5°$ and $\alpha = 25°$. At each measurement point C_L, C_D and C_M were recorded. Figure 4.22 shows the lift coefficient plotted against the angle of attack at different deflection angles.

From figure 4.22 the overall lift performance is shown to be linear up until an angle of attack of 18°, with a lift curve slope of $C_{L_\alpha} = 3.52$ $[1/rad]$. For straight wings at low Reynolds numbers and low aspect ratio a reduced version of the Polhamus equation can be used to calculate the relation between the wing lift curve slope and the lift curve slope of the profile [20]:

$$C_{l_\alpha} = \frac{2 + \sqrt{A^2 + 4}}{A} C_{L_\alpha}$$

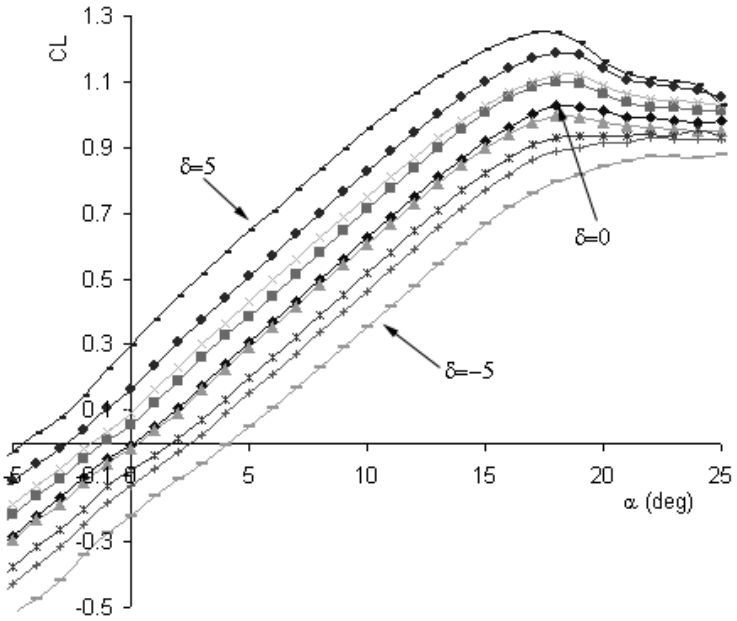

Figure 4.22: Lift coefficient versus angle of attack at various deflection angles.

Substituting for $A = \frac{b}{c} = \frac{460}{127} = 3.62$, and $C_{L_\alpha} = 3.52$ $[1/rad]$ yields $C_{l_\alpha} = 5.97$ $[1/rad]$. Note that since this wing should be mirrored in the wind tunnel wall, the span is increased with a factor of 2. The corrected C_{l_α} is close to the theoretical value of 2π.

The increase in lift as function of the deflection angle, δ, is non-linear. However, it is possible to make an estimate of C_{L_δ}. Since the $C_L - \alpha$ curves are parallel up to 18°, the average C_{L_δ} is constant over this range and amounts to $C_{L_\delta} = 2.97$ $[1/rad]$. Using the same transformation factor as for the lift curve slope, the section $C_{l_\delta} = 5.03$ $[1/rad]$. Although this value is well below the predicted values from section 4.2.2 (C_{l_δ} between 7.95 [1/rad] and 6.58 [1/rad]), it is still significant.

The stall behavior of this wing is fairly good. No steep decreases in lift, even for high deflection angles. The stall angle of attack is around 18°. At higher angles of attack, the lift gradually decreases to a constant value (between $C_L = 0.9$ and $C_L = 1.1$, depending on the deflection).

During cruise the wing should be able to supply 1.5 Newton of lifting force. This translates to a lift coefficient of $C_L = 0.37$ at the specified conditions. Assuming no deformation of the wing, this required lift coefficient is obtained at an angle of attack of $\alpha = 6°$. The relation between lift and drag at a particular angle of attack is displayed in figure 4.23. At an angle of attack of

6 degrees the lift to drag ratio amounts to 4. The maximum lift to drag is a little over 5 for the positive deflections, and shifts between $\alpha = 5°$ (at $\delta = 5°$) and $\alpha = 10°$ (at $\delta = 0°$). For the negative deflections the maximum lift to drag ratio declines to 4.4 at an angle of attack of $\alpha = 10°$ at a deflection of $\delta = -5°$.

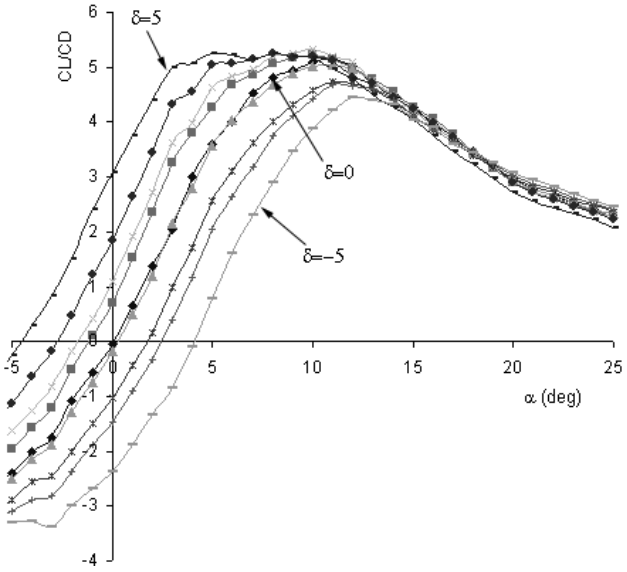

Figure 4.23: Lift over drag at various angles of attack.

In section 3.4 the relation between applied tip force and deflection was discussed. As can be seen from figure 3.8 the deflections of the actuator will be lower when tip force is present. This also holds for the deforming part of the wing, which is loaded by a pressure distribution. This pressure distribution will help the wing deflect upward (negative), but will counteract downward (positive) deflections. These wind tunnel tests have not been carried out with the actual dynamically morphing wing, so no data is yet available on the influence of wing loading on the deflection angles. Further wind tunnel tests with a dynamic test article are required to gain insight in this effect.

4.7 Synopsis

A thin airfoil morphing wing, applicable to a 300 gram MAV has been designed, built and tested. The wing consists of an aerodynamically shaped leading edge which spans 30% of the wing chord and is used to transfer all the aerodynamic loads to the fuselage. The leading edge is made out of a foam core with thin aluminum sheet attached to it. Unidirectional fibres give it additional stiffness. The aft 70% of the airfoil is basically a flat plate with

the piezoelectric elements attached on top and bottom. The wing consists of two individual panels which can be controlled separately in order to create lift control and roll control. In order to magnify rotations, each panel is being precompressed by rubber bands. By applying this precompression, end rotations were magnified with almost a factor of 2, up to 14° peak to peak. A static test article was fabricated in order to verify the lifting capabilities of the wing. A lift curve slope of $C_{L_\alpha} = 3.64$ was found and attached flow was present up to 15° angle of attack. Extensive wind tunnel tests of a static half model of the (total) wing showed a lift curve slope of $C_{L_\alpha} = 3.52$. Furthermore, the influence of the deflection was measured which resulted in a $C_{L_\delta} = 2.97$, which translates to $C_{l_\delta} = 5.03$ for a two dimensional section of this wing. The wing showed good stall behavior. The maximum lift to drag ratio, $(C_L/C_D)_{max} = 5$ and occurs between $\alpha = 5$ and $\alpha = 10$, depending on the amount of deflection. Further wind tunnel tests are required to determine the effect of wing loading on the deflections.

Chapter 5

Thick Wing Design, Fabrication and Testing

A second application of the PBP actuator is found in a thick wing. An existing radio controlled UAV is used to proof the concept of the thick morphing wing. By replacing the normal wing with the modified one, it will be shown that the change in camber of the airfoil will be sufficient to control the rolling motion of the aircraft. This chapter will first give an overview of some aircraft characteristics that are important for the modified wing. Then a preliminary design is presented in terms of general geometry of the wing and airfoil characteristics. Based on the preliminary design each of the wing details are determined and laid out. Then wing fabrication and experiments are presented and the chapter ends with sections on flight and wind tunnel testing.

5.1 Aircraft Properties

5.1.1 Aircraft Geometry

The thick wing concept is implemented in an existing radio controlled UAV. The model type is called the aerobird (compare figure 5.1). Before the thick wing is implemented the characteristics of the unmodified aircraft are examined. This section will show how important properties as aerodynamic center and center of gravity are determined. First of all some basic geometric features of the aircraft are laid out below. Since the wing possesses a curved form of taper, the method of equivalent wing as laid out in section 8.2.3 of [20] is used to determine the equivalent taper ratio and the sweep angle.

Figure 5.1: Radio Controlled UAV: Aerobird.

$$\bar{c}_w = 145 \quad [mm] \qquad \bar{c}_h = 80 \quad [mm]$$
$$S_w = 2.08 \cdot 10^5 \quad [mm^2] \qquad S_h = 1.56 \cdot 10^4 \quad [mm^2]$$
$$b_w = 1392 \quad [mm] \qquad b_h = 372 \quad [mm]$$
$$\Lambda_{c/2_w} = 6 \quad [deg] \qquad \Lambda_{c/2} = 18 \quad [deg]$$
$$\Lambda_{c/4_w} = 10 \quad [deg] \qquad l_h = 776 \quad [mm]$$
$$d_f = 75 \quad [mm] \qquad h_h = -165 \quad [mm]$$
$$\lambda_w = 0.31 \qquad \lambda_h = 0.2$$

5.1.2 Lift curve slope

To determine the lift curve slope of the wing Polhamus equation is used (eqn. (8.22) [20]):

$$C_{L_{\alpha_w}} = \frac{2\pi A}{2 + \sqrt{\frac{A^2\beta^2}{k^2}(1 + \frac{tan^2\Lambda_{c/2}}{\beta^2}) + 4}} \tag{5.1}$$

Where,

$$A = \frac{b^2}{S} \tag{5.2}$$

$$\beta = \sqrt{1 - M^2} \tag{5.3}$$

$$k = \frac{C_{l\alpha_{at\ M}}}{\frac{2\pi}{\beta}} \tag{5.4}$$

$$C_{l_{\alpha_{at\ M}}} = \frac{C_{l_{\alpha_{at\ M_0}}}}{\sqrt{1 - M^2}} \tag{5.5}$$

These equations are equations (8.23) to (8.25) and (8.1)respectively from [20]. For a low speed MAV with a straight wing the following assumptions are made:

$$\beta = \sqrt{1 - M^2} \cong 1 \qquad C_{l_{\alpha_{at\ M_0}}} \cong 2\pi$$

With these assumptions equation 5.1 reduces to

$$C_{L_{\alpha_w}} = \frac{2\pi A_w}{2 + \sqrt{1.01 A_w^2 + 4}} \tag{5.6}$$

For the horizontal tail a similar analysis can be exercised. Because of the sweep angle of the horizontal tail the equations for the lift curve slope of the horizontal tail reduce to

$$C_{L_{\alpha_h}} = \frac{2\pi A_h}{2 + \sqrt{1.11 \cdot A_h^2 + 4}} \tag{5.7}$$

When the aircraft geometry parameters are substituted in equations (5.2) and (5.6) than the following is obtained.

$$A_w = 9.32 \qquad C_{L_{\alpha_w}} = 5.06\ [1/rad]$$
$$A_h = 4.45 \qquad C_{L_{\alpha_h}} = 3.94\ [1/rad]$$

5.1.3 Static Margin

The aerodynamic center of the aircraft is calculated as follows (eqn. (8.82) [20]):

$$\overline{x}_{ac_A} = \frac{\overline{x}_{ac_{wf}} C_{L_{\alpha_{wf}}} + \{\eta_h C_{L_{\alpha_h}} (1 - \frac{d\epsilon}{d\alpha}) \frac{S_h}{S_w} \overline{x}_{ac_h} - \eta_c C_{L_{\alpha_c}} (1 + \frac{d\epsilon_c}{d\alpha}) (\frac{S_c}{S} \overline{x}_{ac_c})\}}{C_{L_\alpha}} \tag{5.8}$$

Where (eqn. (8.83) [20]):

$$\overline{x}_{ac_{wf}} = \overline{x}_{ac_w} + \Delta \overline{x}_{ac_f} \tag{5.9}$$

$C_{L_{\alpha_w}}$ and $C_{L_{\alpha_h}}$ are determined by equation 5.1. When no canard is present and $\Delta \overline{x}_{ac_f}$ is assumed 0, equation 5.8 is reduced to

$$\overline{x}_{ac_A} = \frac{\overline{x}_{ac_w} C_{L_{\alpha_w}} + \{\eta_h C_{L_{\alpha_h}} (1 - \frac{d\epsilon}{d\alpha}) \frac{S_h}{S_w} \overline{x}_{ac_h}\}}{C_{L_\alpha}} \tag{5.10}$$

Where (eqn. (8.34) [20]):

$$\eta_h = \frac{\overline{q}_h}{\overline{q}} \tag{5.11}$$

With $\overline{q}$ being the dynamic pressure in the free stream and $\overline{q}_h$ being the dynamic pressure at the horizontal tail. C_{L_α} is the lift curve slope of the total aircraft. Equations (5.12) to (5.18) correspond to equations (8.42) to (8.48) in [20]:

$$C_{L_\alpha} = C_{L_{\alpha_{wf}}} + C_{L_{\alpha_h}} \eta_h (1 - \frac{d\epsilon}{d\alpha}) \frac{S_h}{S_w} \tag{5.12}$$

In this equation the following terms appear:

$$C_{L_{\alpha_{wf}}} = K_{wf} C_{L_{\alpha_w}} \tag{5.13}$$

where K_{wf} is the fuselage interference factor given by:

$$K_{wf} = 1 + 0.025 \frac{d_f}{b} - 0.35 \Big(\frac{d_f}{b}\Big)^2 \tag{5.14}$$

$\frac{d\epsilon}{d\alpha}$ is the downwash gradient at the horizontal tail:

$$\frac{d\epsilon}{d\alpha} = 4.44 [K_A K_\lambda K_h \sqrt{cos\Lambda_{c/4}}]^{1.19} \frac{(C_{L_{\alpha w}})_{at\ M}}{(C_{L_{\alpha_w}})_{at\ M=0}} \tag{5.15}$$

where:

$$K_A = \frac{1}{A_w} - \frac{1}{1 + A_w^{1.7}} \tag{5.16}$$

$$K_\lambda = \frac{10 - 3\lambda_w}{7} \tag{5.17}$$

$$K_h = \frac{1 - \frac{h_h}{b_w}}{\left(\frac{2l_h}{b_w}\right)^{\frac{1}{3}}} \tag{5.18}$$

Substituting the aircraft geometry parameters in these equations yields the following results:

$K_{wf} = 1.000$ $K_A = 0.085$ $K_\lambda = 1.296$ $K_h = 1.079$

$\frac{d\epsilon}{d\alpha} = 0.35$ $C_{L_{\alpha_{wf}}} = 5.06\ [1/rad]$ $C_{L_\alpha} = 5.25\ [1/rad]$ $\eta_h = 1$

It is assumed that the aerodynamic center of the wing and the horizontal tail is at the quarter chord of their mean chord. The center of gravity is determined experimentally by balancing the aircraft on the wing. When the numerical values are substituted in equation 5.10 the mean aerodynamic center and center of gravity are obtained. The positions of the aerodynamic center and the center of gravity in terms of fuselage station w.r.t. the nose of the aircraft are displayed below the mean values.

$\overline{x}_{ac_A} = 0.44$ $\overline{x}_{cg} = 0.33$

$x_{ac_A} = 235\ [mm]$ $x_{cg} = 219\ [mm]$

The static margin is good measure for the longitudinal stability of the aircraft. Using the above stated numerical values gives the following:

$$SM = \overline{x}_{ac_A} - \overline{x}_{cg} = 0.11$$

5.2 Airfoil Design

5.2.1 Airfoil Geometry

Following a top down approach different airfoil geometries are examined on their aerodynamic properties. This is done using Xfoil, at a Reynolds number of 10^5 and a velocity of 15 m/s. Existing low Reynolds number airfoil geometries are investigated and compared (NACA, Selig, Eppler). In order to be able to apply an axially precompressed piezoelectric element on the camber line a symmetric airfoil is required. Lift, drag and moment are examined at angles of attack ranging from 0 to 15 degrees. For this

morphing wing an NACA 0012 airfoil geometry is proposed ($C_{l_{max}} = 0.95$, $(l/d)_{max} = 33$ and occurs at $\alpha = 5°$).

In the previous chapter it was determined that the piezoelectric element would form both inner and outer skin of the thin airfoil. This way no deforming of the rest of the structure would be necessary and there would be no additional resistance. For a profile with finite thickness it is impossible to *not* deform the structure. There will be structural morphing of at least the skin of wing. The first 40% of the chord is rigid and provides the wing with stiffness to transfer the aerodynamic loads to the remaining wing structure. A bender element is placed over the aft 60% of the chord line of the airfoil. When the element bends, it will deflect the trailing edge, and consequently deform the entire airfoil section. This does require some sort of flexible skin that is able to expand and contract when the airfoil deflects.

Whereas the thin airfoil makes use of a rubber band to pre-compress the piezoelectric laminate, the thick airfoil might use another instrument. Instead of using a flexible skin that produces an as little as possible resistance to bending, the skin could also be used as a precompression tool for the laminate. This way the skin contributes to the deformation of the wing without being actively controlled. A consequence of this is that a flexible skin (e.g. natural rubber) over a substantial part of the wing is required. This also means that it is not possible to follow the entire contour of the NACA 0012 because the second half of the profile will be straight due to the precompression characteristic of the skin.

To check what would be the influence of such a design, the NACA 0012 geometry is adjusted and run in the panel code Xfoil. The characteristics are very much alike. The lift coefficient is only slightly less than for the NACA 0012. The stall characteristics are not as good as for the original profile. Stall will originate at a lower angle of attack (12°)than for the original airfoil (15°).

The shape of the NACA 0012 is prescribed by a set of coordinates. The thickest point lies at 30% of the chord. The maximum thickness is 12% of the chord. After the first 30% of the chord the contour of the NACA 0012 cannot be followed anymore. From there on, the skin could follow a straight line to the trailing edge of the airfoil. However, this would lead to a kink in the skin. This kink is un-beneficial since it is likely to cause separation and consequently a lot of additional drag and a loss in lift. When the trailing edge is moved downwards, the kink on the upper side would increase even more.

Instead of the kink, the straight after part of the airfoil should be tangent to the front part. Then there will be no discontinuities in the skin geometry and the flow is less likely to separate. Moreover, when the trailing edge is deflected the tangency condition should remain. The structure of the airfoil

must be rigid up to the point where the straight part of the skin meets the curved part. When the trailing edge is deflected up or downward this point will move also. This is shown in figure 5.2.

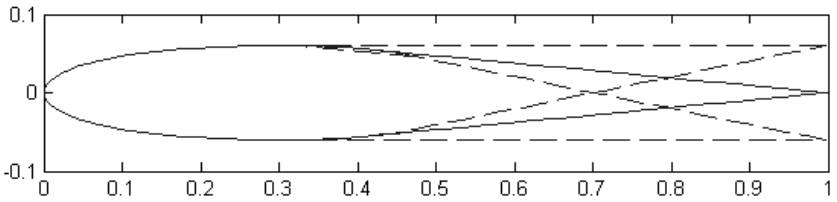

Figure 5.2: Change in airfoil camber due to PBP actuation.

5.2.2 Predicted Static Performance of Thick Airfoil

This section will give an overview of the main characteristics of the thick airfoil. As shown in section 3.3 the actuator deflection, δ_0 is determined by the amount of curvature κ. By changing the curvature the actuator will deflect and the outer shape of the airfoil will deform. In this section $delta_0$ is shortened with δ, for convenience. The deflection angle, δ in these plots is limited to +/-6°.

Figure 5.3 shows the predicted lift coefficient plotted against the deflection angle and angle of attack. Both graphs show a more or less linear relationship between the lift coefficient and the deflection angle (δ) and angle of attack (α), respectively. At zero angle of attack $C_{l_\delta} = 5.54\ [1/rad]$, while at $\alpha = 8°$ this has declined to $C_{l_\delta} = 3.05\ [1/rad]$.

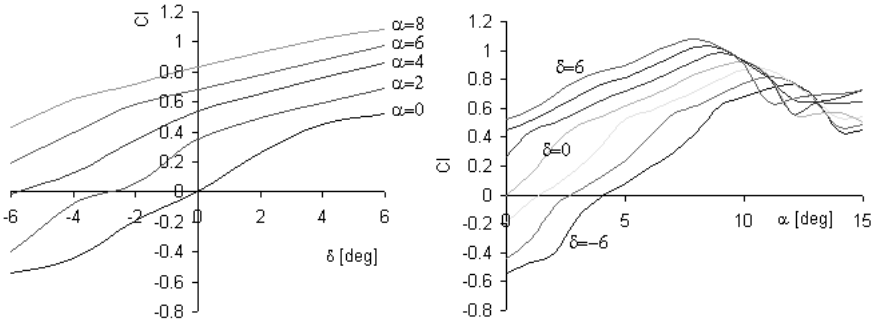

(a) Predicted C_l vs. δ (b) Predicted C_l vs. α

Figure 5.3: Lift coefficient as a function of δ and α.

Figure 5.4 shows the drag coefficient of a function of delta and alpha, re-

spectively. From 5.4-a it can be seen that at angles of attack higher than six degrees the deflection of the airfoil can induce early separation and consequently a drag rise.

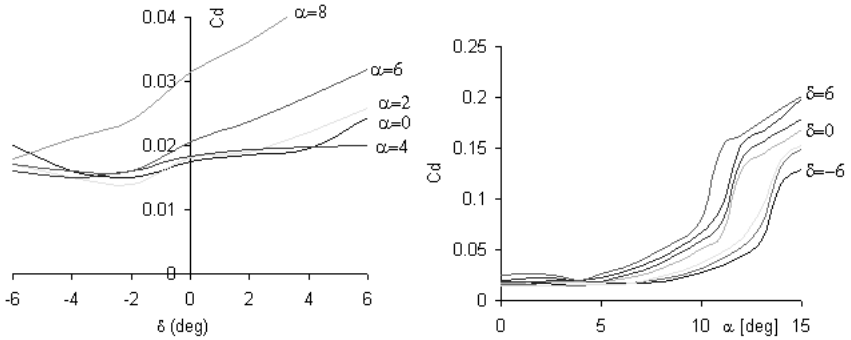

(a) Predicted C_d vs. δ (b) Predicted C_d vs. α

Figure 5.4: Drag coefficient as a function of δ and α.

The moment lines are drawn in figure 5.5. As can be seen from 5.5-b the moment line has a positive slope for each deflection angle. This indicates that the airfoil is unstable and a horizontal tail is required to balance the aircraft. From 5.5-a it can be observed that C_{m_δ} is negative, although decreasing in an absolute sense with increasing angle of attack.

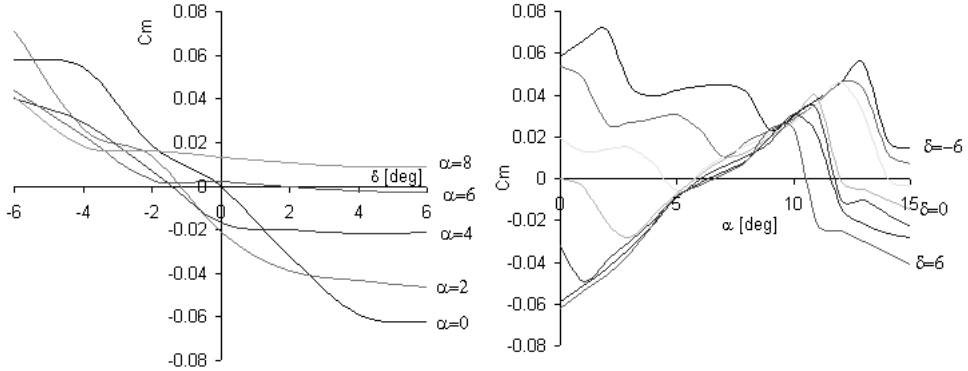

(a) Predicted C_m vs. δ (b) Predicted C_m vs. α

Figure 5.5: Moment coefficient as a function of δ and α.

5.3 Wing Design

The wing of the Aerobird has a mean aerodynamic chord of 145 mm and a span of 140 cm. The replacing wing has these exact same dimensions, in order to stay close to the original design. However, the new wing does not exhibit any taper or sweep, contradictory to the original wing. This is done to make incorporation of the morphing part easier. According to equation 5.2 the aspect ratio of this wing amounts to 9.65.

The morphing parts of the wing are supposed to induce a motion about the longitudinal axis of the aircraft (rolling). They will act the same way as ailerons would do on conventionally controlled aircraft. To produce a large moment around the longitudinal axis, the morphing parts are placed at the outboard side of the wing (confer figure 5.6).

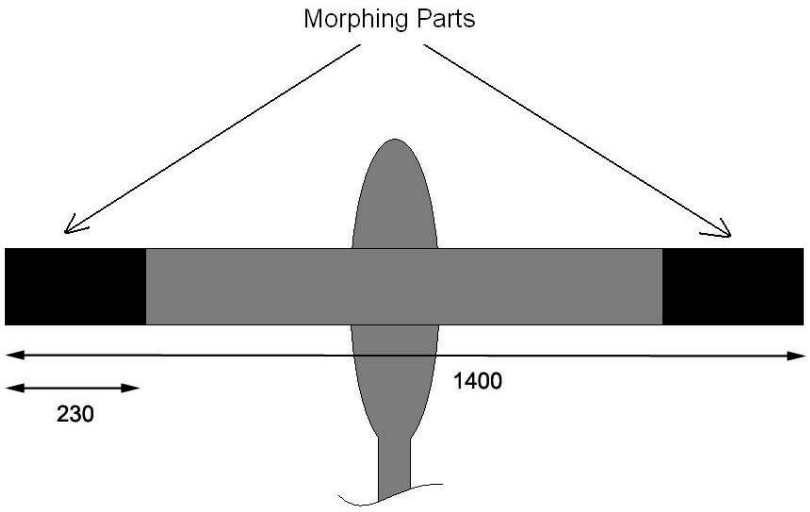

Figure 5.6: Topview of wing, including morphing outboard parts (all dimensions in mm).

The influence on the stability by using this new wing geometry is determined using the model as laid out in section 5.1. Inserting the new values for wing geometry and keeping in mind that the rest of the aircraft remains unchanged, the following values are obtained:

$$C_{l_{\alpha_w}} = 5.11\ [1/rad] \qquad K_A = 0.082 \qquad K_\lambda = 1.000 \qquad K_h = 1.079$$
$$\frac{d\epsilon}{d\alpha} = 0.25 \qquad C_{L_{\alpha_{wf}}} = 5.11\ [1/rad] \qquad C_{L_\alpha} = 5.34\ [1/rad] \qquad \eta_h = 1$$

The neutral position is shifted backward with 2.5% with respect to the original wing and is now positioned at 46.5% of the wing chord. Assuming

the position of the center of gravity remains unchanged, this yields a static margin of 13% for this new wing. Consequently, the application of this straight wing indicates that the aircraft would be slightly more stable than with the original wing.

For the static part of the wing a conventional balsa wood structure is proposed. This section will not go into the details of that part of the wing because it does not exhibit any extraordinary features. Section 5.5 will show the structure of this part of the wing in more detail.

The morphing part of the wing is designed as simple as possible. Including the skin the entire morphing wing part consists of only 6 components: a carbon fibre shell that acts as torque box, three PZT bending actuators, a trailing edge and the skin. The span of each of the morphing parts amounts to 230 mm, which implies that 33% of the will be morphing. Figure 5.7 shows the design of the wing.

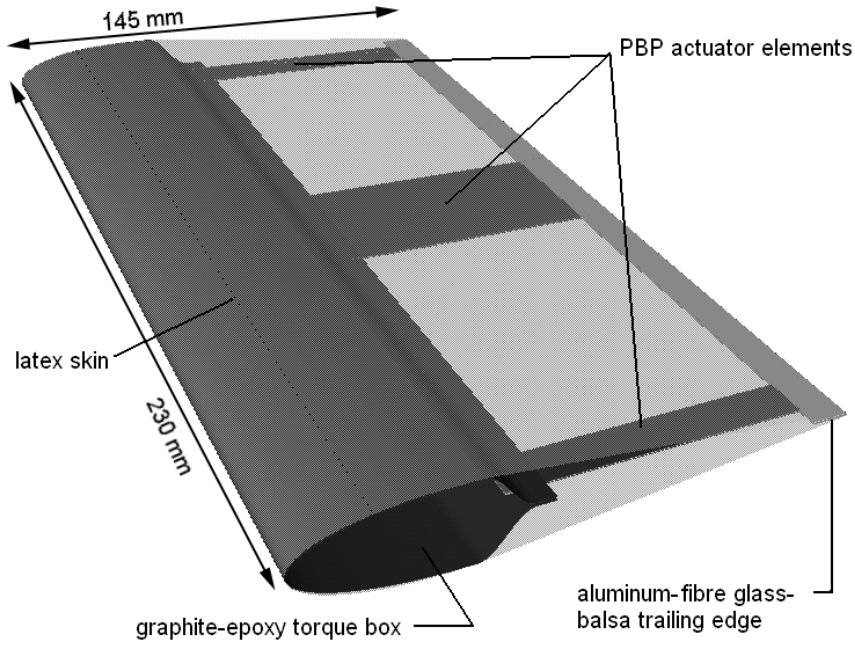

Figure 5.7: Thick wing design.

The most interesting part of this design is the carbon fibre shell. It follows the contour of the NACA 0012 airfoil exactly, up till 30% of the chord. After this point it converges until the top and bottom face almost touch. Between these faces the bender actuators can be clamped. The rubber skin goes over the carbon fibre shell and over the trailing edge thereby forming the outer shape of the airfoil.

The width of the piezoelectric actuators is chosen based on the available stock of PZT 5A with a width of 0.192 mm. The two outboard actuators both have a width of 10 mm while the center element has a width of 35 mm. Accordingly, the total width amounts to 55 mm, which is a slightly smaller than the total width of the two panels for the thin wing concept (60 mm). The total buckling load for these elements lies between 3.0 and 3.3 kgf (compare figure 3.10). The skin precompression should remain well below this value. This means that the force applied by the skin may not me higher than 13 gmf/mm.

5.4 Proof of Concept

5.4.1 Skin of the Wing

As has been said before, the skin of the wing is one of the key features of this design. It fulfills two purposes. First of all it will transfer the pressure distribution to the structure of the wing. Additionally it will also pre-compress the adaptive laminate inside the wing. When the laminate is properly compressed, the deflections will be larger than for the free piezoelectric laminates.

A model of the precompression of the laminate is not too difficult to construct. When the laminate is loaded by the skin, this can be modeled as a cantilevered beam loaded by two springs (compare figure 5.8-a). Since the skin is likely to made out of rubber, the stiffness, k, of the spring is not constant, but will be linear with the amount of stretching. The forces induced by the springs can be decomposed into a force in plane with the laminate and one orthogonal to this plane. This is shown in figure 5.8-b.

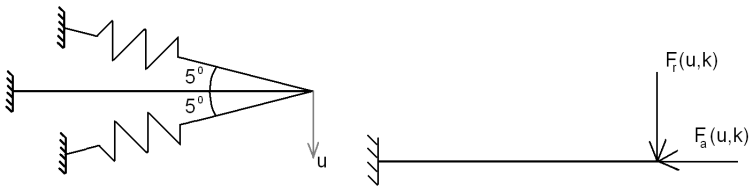

(a) Model of elastic skin. (b) Decomposed forces.

Figure 5.8: Model of the skin pre-compressing the adaptive laminate.

The two forces shown in figure 5.8-b are dependent on the spring stiffness, k, and the amount of deflection, u. The force F_1 will always work in the opposite direction of the deflection. The other force, F_2, will help the laminate deflect, analogous to the rubber band in the thin airfoil concept. The ratio

between those two forces will determine whether the tip of the airfoil will deflect. Naturally these two forces are coupled, because they are produced by the same skin. The amount of initial stretch in the rubber skin determines the amount of deflection of the laminate. The total deflection will probably be less than for the thin airfoil wing, because there is an additional resistive force, F_1.

Skin experiment The stiffness of the skin relates the elongation of the skin to the force it applies. Since the skin of the wing is going to be made out of natural rubber (latex), its modulus of elasticity (E) will not be constant. Therefore an experiment was carried out to determine the relation between the stress and strain in the material. The test setup is shown in figure 5.9. The skin is wrapped over two identical circular bars. One bar is connected to a scale and one bar is connected a vertical displacement measurement device. By turning the wheel on this device the elongation of the skin can be measured up to an accuracy of 0.001". The force on the scale is measured in grams.

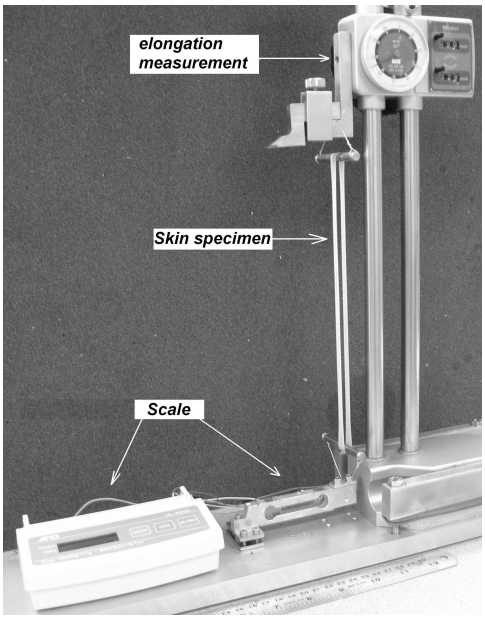

Figure 5.9: Experimental setup to determine the stiffness of the skin material.

A series of experiments were carried out in the following way: After proper installment of the skin in the test setup the skin was elongated over an interval of 12.7 mm (0.5 inch). At each interval the specimen was given time to adjust and settle down to a constant force level. When this level was

reached the force measurement was taken. This was done until a maximum elongation level was reached. Then the specimen was relaxed again at regular intervals and the force was obtained. When the specimen was again in a total relaxed state the run was completed. After one run of experiments a second run was carried out to see what the effect of hysteresis is on the stiffness properties of the material. The same sequence was carried out for this run as for the first one.

During the first set of experiments it was observed that the rubber showed non-uniform lateral contraction and local wrinkling during relaxing of the specimen. Since this is not a desired characteristic it was determined to grease the top and bottom bar so the specimen would be able to slide over them. The next set of experiments therefore showed a uniform lateral contraction (which was also measured) and no wrinkling. Three sets of experiments were carried out. The first one using a specimen from a high quality helium balloon. The second set used specimen from the same type of balloon, only after it had been inflated (polymers are oriented). The third specimen came from a Trojan condom.

Results The results of the experiment are laid out as specific force vs. strain curves in figure 5.10. Curves are shown for three individual specimen with different properties. The first specimen was made out of a high quality helium balloon. The original length of this specimen was 32 mm (4). A second specimen consisted of the same balloon material only after inflation. This pretreatment gave the specimen a new initial length of 50 mm. A third specimen made out of a (Trojan very sensitive) condom had an initial length of 51 mm. The experiments were carried out several times to verify the measurements. The specimen showed very consistent behavior.

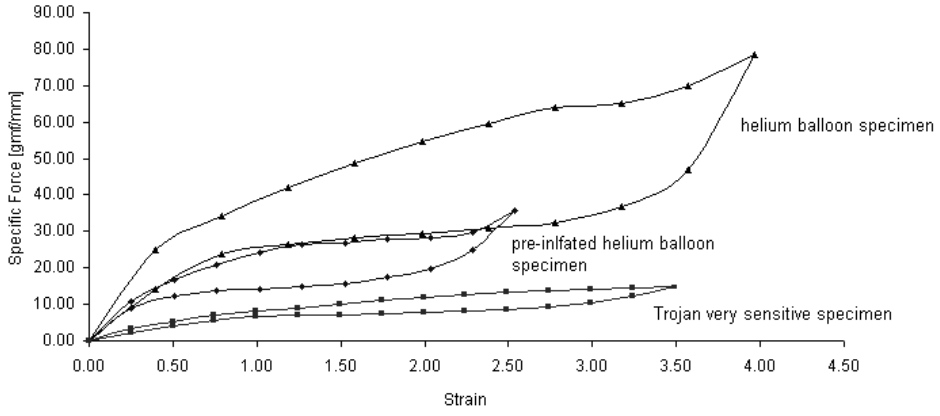

Figure 5.10: Specific force versus strain curves for various specimen.

From figure 5.10 it can be seen that the three specimen had different characteristics. The normal (that is: not pre-tensioned) balloon specimen exerts a much higher force per mm than the pre-inflated specimen. The third specimen (condom) shows distinctly lower specific forces than the other two. Hysteresis is defined as the ratio between the surface area under the upper part of the curve and the surface area between the two curves. It turns out that the hysteresis for both balloon specimen is virtually identical and amounts to 34%. However, for the condom, hysteresis only amounts to 26%.

As stated in section 5.3 a maximum axial force of 13 gmf/mm can be applied by the skin. Both the balloon specimen gave a force that was too high. It was therefore determined that the condom had the most desirable characteristics. It provided a relatively low compressive force per millimeter. Furthermore, the condom showed the lowest amount of hysteresis, comes in uniform quality, is easy to purchase and is relatively cheap.

5.4.2 Static Test Article

Before the actual wing is manufactured, a static test article is build. This test article has the same shape and chord length as the real wing. However, it is made out of normal plywood, and instead of using the expensive PZT actuators, they are replaced by aluminum bars with a similar EI product. The major goal of this test article is to show that precompression of the skin does decrease the effective stiffness of the surrogate actuators. To be able to stretch the skin and wrap it around the frame in a controlled manner, a stretching mechanism built. This ensures that the force-elongation curve as shown in figure 5.10 can be followed.

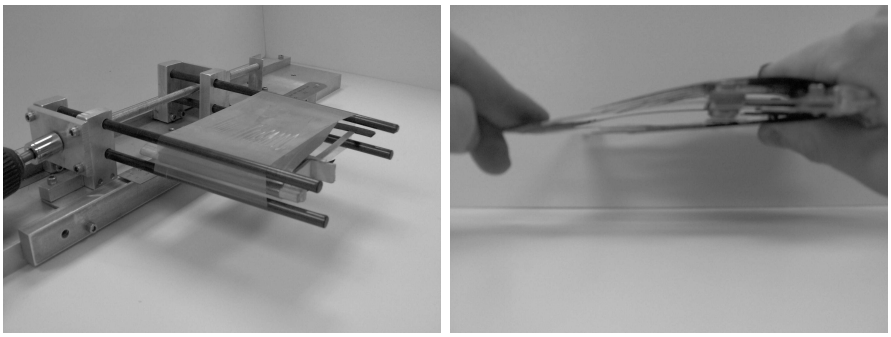

(a) Stretch contraption. (b) Deforming wing.

Figure 5.11: Static test article

The static test article gives a good insight in the result of axial compression on the surrogate actuators. By making a mechanical contraption, the chord

length is made variable. By varying the cord, the tension in the skin can be adjusted. This is used to tweak the precompressive force such that by applying only 0.1 N of a vertical tip force the tip deflection is over 10 mm.

5.4.3 Dynamic Test Article

For the dynamic test article the basic set-up is analogous to the static test article. However, the aluminum strips are replaced by piezoelectric actuators. The product of moment of inertia and stiffness is the same for both the aluminum strip and the actuator. It is assumed that the total laminate stiffness of the actuator can be approximated by the stiffness of the PZT elements.

$$E_a I_a = E_{AL} I_{AL} \tag{5.19}$$

A second deviation from the static test article is the fabrication of the trailing edge. To comply with the Kutta condition a fairly sharp trailing edge is fabricated. It consists of a sandwich of 0.058 mm steel, and a balsa wood core. Between the steel outside and the balsa wood a thin layer of 45 degree oriented glass fibre fabric is integrated to provide torsional stiffness and also insulate the aluminum core of the bending actuator. Figure 5.12 shows the dynamic test article and its dimensions.

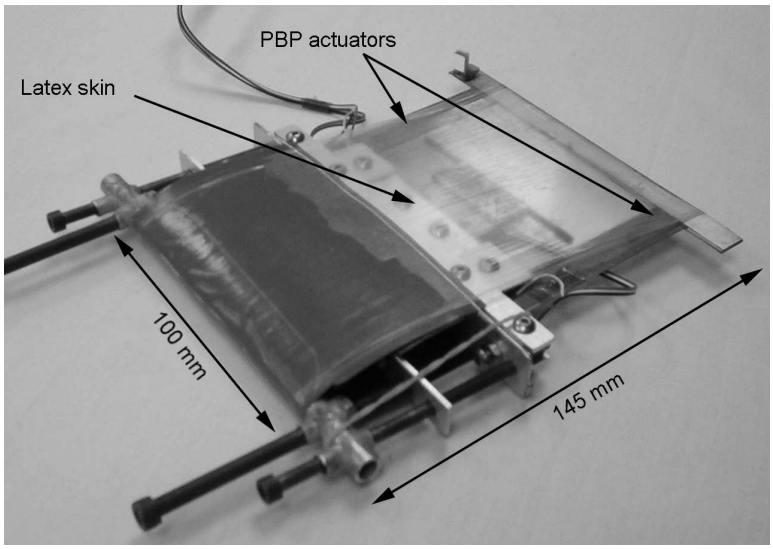

Figure 5.12: Dynamic test article dimensions and features.

The influence of the pre-compression of the skin is investigated. To do this, the end rotation of the specimen is measured for both the skin-on and the

skin-off case. A series of quasi static tests is carried out. The test setup for this experiment is displayed in figure 5.13 and is analogous to the set-up that is described in section 3.5. A small laser mirror is mounted on the trailing edge. A laser beam is used to magnify the end rotations so it can be accurately read from the screen. The laser dot can be seen in figure 5.13-b, near the right edge of the picture.

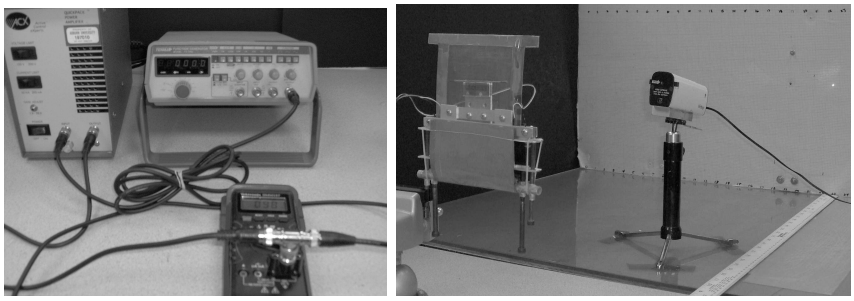

(a) Power supply and signal generator

(b) Deflection measurements

Figure 5.13: Experimental test set-up.

The first test article failed because of an erroneous signal that was created by the power supply upon connecting it to the actuators. Both actuator specimen broke. A second test article was manufactured to continue testing. To prevent this test article from breaking, a bump stop was put in the center of the airfoil section. This acts as a physical boundary for the skin. When the specimen tends to over-rotate the skin will hit the bump stop and will prevent the actuators from breaking. Figure 5.14 shows how the shape of the wing changes when the PBP elements are actuated.

Two series of experiments were carried out. A quasi static test was done to determine the relation between the applied voltage and the end rotation of the specimen. A dynamic test was executed to investigate the change in natural frequency due to the application of the precomprressing skin. Both experiments were carried out on the skin-on and skin-off test article under the same conditions. Figure 5.15 shows the peak-to-peak end rotations of the trailing edge.

From figure 5.15-a it can be noticed that due to the application of the skin the end rotations are more than doubled, to 15° peak to peak. In 5.15-b it is shown that the natural frequency has shifted from 31 Hz to 26 Hz. This indicates that the geometric stiffness of the total assembly, being the actuators plus the skin, has decreased.

$$\frac{k_{skin\ on}}{k_{skin\ off}} = \frac{\omega^2_{skin\ on}}{\omega^2_{skin\ off}} \tag{5.20}$$

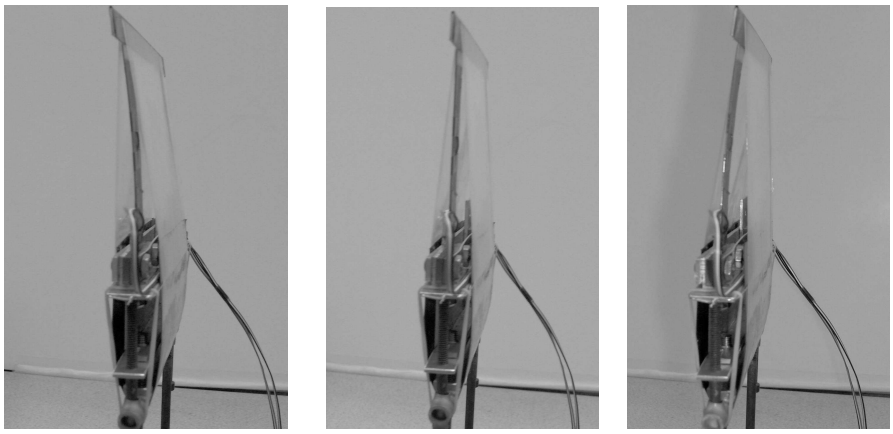

(a) Deflection to the left (b) Neutral position (c) Deflection to the right

Figure 5.14: First dynamic test article deflections.

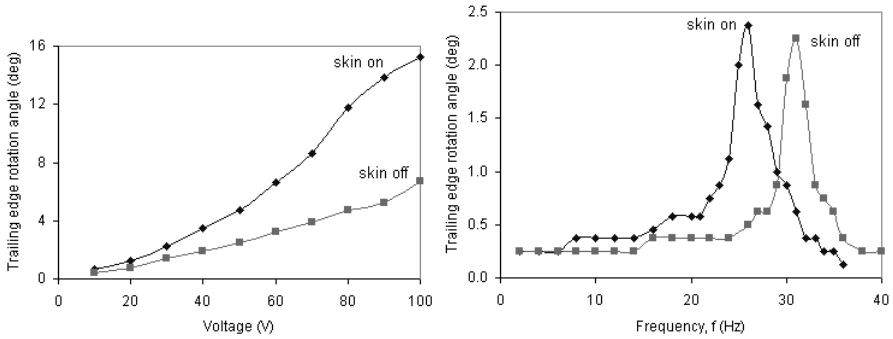

(a) Quasi static end rotations as a function of voltage. (b) End rotations as a function of actuation frequency.

Figure 5.15: Results quasi-static and dynamic experiments

Substituting the above mentioned values for the natural frequency shows that the remaining geometric stiffness in the actuator assembly is only 70% of the original geometric stiffness.

From the dynamic tests it can be concluded that the pre-compression in the skin could still be further increased in order to decrease the effective stiffness even further. A result of that would be higher curvatures. However, if curvatures become too high the skin will eventually break the specimen. The deflections in the test article specimen go up to 40% of the maximum deflection (compare section 3.5). Furthermore it can be seen that the corner frequency of the actuator is shifted from 38 Hz to 34 Hz. Above the corner frequency, the deflections decrease substantially and can therefore not be used anymore.

5.5 Wing Fabrication

5.5.1 Leading Edge Torque Box Fabrication

The carbon fibre torque box is manufactured in three subsequent steps. First a positive mold is made out of oak wood. To ensure symmetry, a thin metal sheet is positioned in the middle of the mould. From the wooden mold a silicone female mold is produced. This is done for each of the two halves separately. After the two molds are finished a carbon fibre pre-preg is positioned in between the two. A vacuum bag is used to apply pressure. Then the entire assembly is cured in the oven. After removal of the molds the carbon fibre torque box remains. Figure 5.16 shows the subsequent steps.

5.5.2 Static Wing Fabrication

The morphing wing part of the wing is intended to replace the ailerons. This means that the static part of the wing ($b = 940\ mm$, $c = 145\ mm$) can be manufactured using a conventional structure and conventional materials. It is chosen to make the wing structure out of balsa wood and use covering material for the skin. A relatively simple structure is designed and built. The structure consists of a main spar, a leading edge (which also acts as front spar), a trailing edge (which also acts as rear spar), and ribs in between. All the individual parts are bonded together using cyanoacrylate resin.

To give additional stiffness to the structure, the first 30% of the airfoil is covered with balsa wood sheeting (both top and bottom face). An extension of the wing is created to attach the carbon fibre shell, which has to be positioned at the tips of the balsa structure. Holes in the ribs allow for electrical wiring to the piezoelectric laminates. The wing has a dihedral of 2 degrees on each side. A picture of the wooden structure is displayed in figure

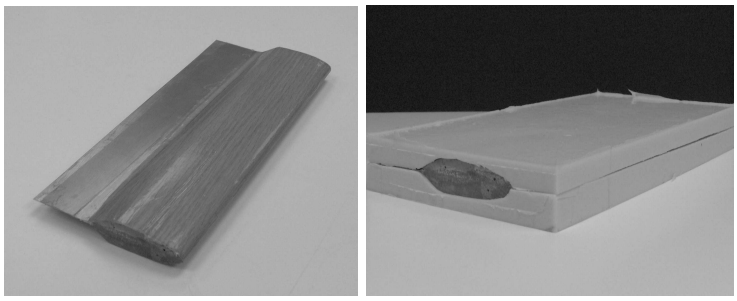

(a) Positive mold (b) Mold sandwich

(c) Vacuum bagging (d) Finished product

Figure 5.16: Torque box fabrication.

5.17-a. The final static part of the wing weighs 120 grams and is shown in figure 5.17-b.

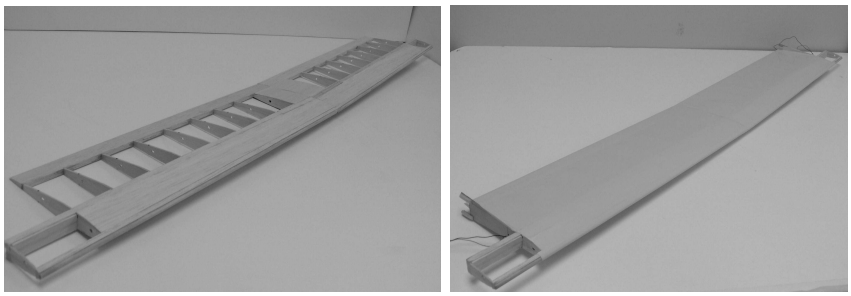

(a) Wing structure. (b) Finished static part.

Figure 5.17: Balsa wood wing.

5.5.3 Actuator Fabrication

Contradictory to the actuator fabrication of the thin wing, for these actuators a dry lay-up is carried out. The bimorph element consists of five layers: [CAP($+\Lambda$)/Hysol bond/aluminum sustrate/Hysol bond/CAP($-\Lambda$)]. The

thickness of each of the PZT sheets is 0.191 mm (7.5 mil). The thickness of the aluminum and the pre-preg Hysol bonding layer amount to 0.0765 mm (3 mil) and 0.101 mm (4 mil), respectively. Total thickness of a well manufactured laminate adds up to 0.66 mm (26 mil). Figure 5.18-a shows the different layers, along with the fibre glass end tabs.

The dry lay-up is a very neat way of manufacturing the bimorph laminates. The finished actuators are placed on a caul plate (figure 5.18-b). A second caul plate is positioned on top of the first one. The whole assembly is being clamped as it goes into the oven at a temperature of 176 degrees Celsius, for two hours. As the laminates come out, they are trimmed to the required size and wired up subsequently. Each element is tested individually before it is applied in the wing structure.

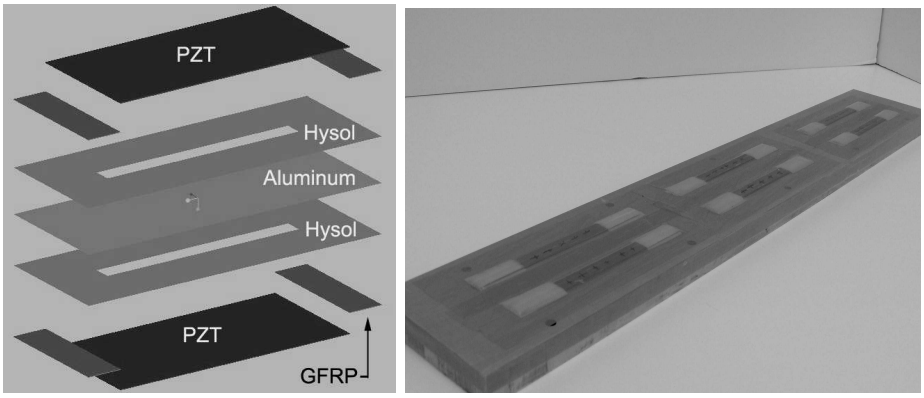

(a) Different layers of the laminate. (b) PZT lay-ups on caul plate before curing.

Figure 5.18: Bimorph actuator fabrication.

5.5.4 Wing Assembly

With all the main components present, the entire wing is assembled. The PZT parts are glued into the carbon shell. However, in addition to the original design, an extra fibre glass slot for the PZT laminates to slide in is fabricated. This prevents electrical charging of the carbon fibre shell during operation. Furthermore, a simple sandwich trailing edge is made analogous to the one used in the test article. The assembled adaptive part is shown in figure 5.19-a and weighs 45 grams.

The adaptive part of the wing is first assembled, then the skin is put around it and a test is run to determine the maximum deflection. Also a frequency sweep is carried out to find the shift in eigen frequency due to the precompression of the skin (compare figure 5.19-b). This is all analogous to the tests done on the test article.

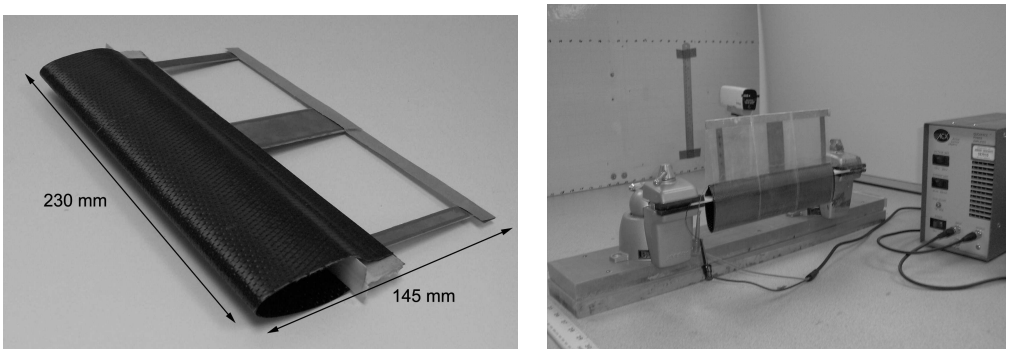

(a) Assembled adaptive part. (b) Deflection testing.

Figure 5.19: Adaptive wing assembly.

The skinned adaptive parts are then bonded to the balsa wood wing. Physical bump stops are connected to the balsa wing and to the tip of the carbon shell. These bump stops prevent the adaptive part from over rotating. The outer bump stop acts as a winglet at the same time and also protects the morphing part during a heavy landing. Figure 5.20 gives an overview of the wing in assembled state. In figure 5.21 the total aircraft is shown with the morphing wing on top and all the electronics included in the body of the aircraft. The total weight of the wing amounts to 210 grams, which is a reduction of 9% with respect to the original wing (230 grams).

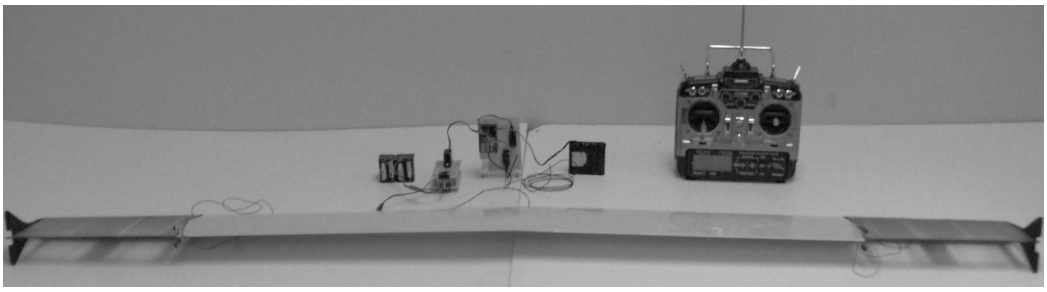

Figure 5.20: Total assembled wing including required driver electronics.

5.6 Flight Testing

To close the design loop a flight test is carried out to see how the wing behaves in flight. This is one way to prove that the concept of a morphing wing is realistic and feasible. Since a symmetric airfoil is used, the wing has to fly at relatively high angles of attack and high speeds to gain enough lift.

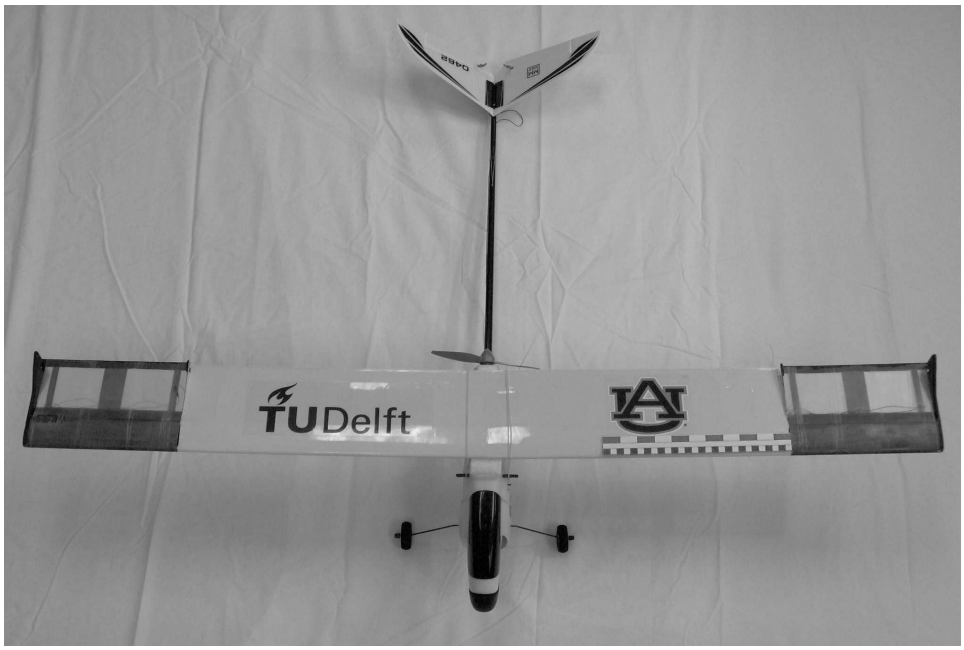

Figure 5.21: PBP Wing mounted on UAV (topview).

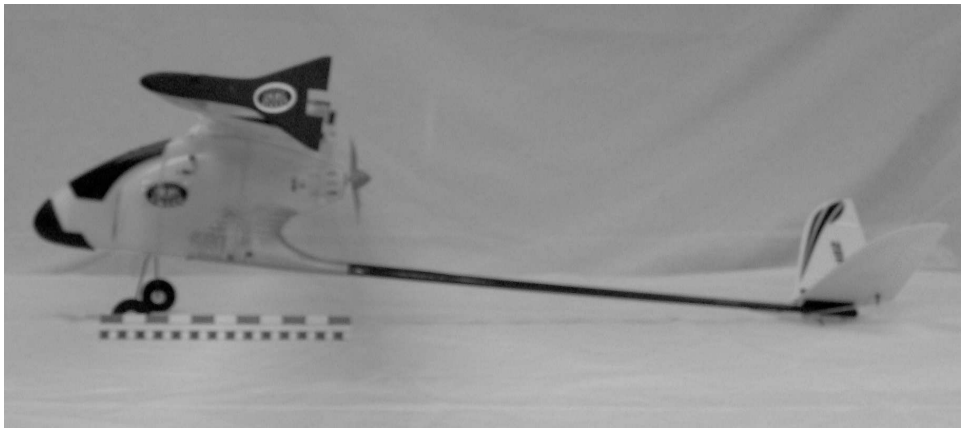

Figure 5.22: PBP Wing mounted on UAV (sideview).

However, this does also mean that a high speed take off is required to get it flying. The aircraft is being hand launched.

The actual flight test was carried out on April 29^{th}, 2005 in Auburn, Alabama. To let the pilot, mr. Christoph Burger, get used to the aircraft characteristics, the aircraft was first flown with the conventional wing on. The original wing does not have any ailerons and is just made out of foam. Pictures and video were taken throughout the maiden flight of the first piezoelectric actuated morphing wing. Figure 5.23 gives an overview of the flight testing.

The first flight with the adaptive wing, showed that the center of gravity was shifted too much to the front. By adding weight to the tail this problem was solved quickly and easily (fig. 5.23-c). The second run the aircraft did not pick up enough speed to take off (it is hand launched) and so it crashed causing the propeller to chop off a small part of the trailing edge of the wing. Flashing tape was used to repair this (fig. 5.23-d).

The third try was successful. The plain took off (fig. 5.23-e) and the pilot manoeuvred it using the conventional controls first. After a few laps of normal control, the morphing parts of the wings were used to induce a rolling motion. According to the pilot the aircraft responded "real nice" to the roll control input. A five minute flight was carried out in which the aircraft rolled really well in both directions (fig. 5.23-f).

Because the wing is symmetric, the plane had to fly fast and under a hight angle of attack. The symmetric profile was chosen because the morphing part of the wing needs symmetry in order to operate well. However, from the test flight it became clear that the static part of the wing should have been made cambered in order to produce enough lift at zero or small angles of attack.

The most important conclusion is however, that it is possible to integrate a piezoelectrically actuated morphing wing on a UAV and make it flight worthy. Moreover, it is shown that this way of wing morphing is a feasible, efficient and light weight alternative for roll control.

5.7 Wind Tunnel Test

To determine the actual behavior of the morphing wing panel under aerodynamic loading, a wind tunnel test article is fabricated. This test article is basically the morphing wing with additional end plates. The end plates prevent tip vortices to distort the flow over the top of the wing. This way a two dimensional wing section is being simulated. Figure 5.24-a shows the wind tunnel test article.

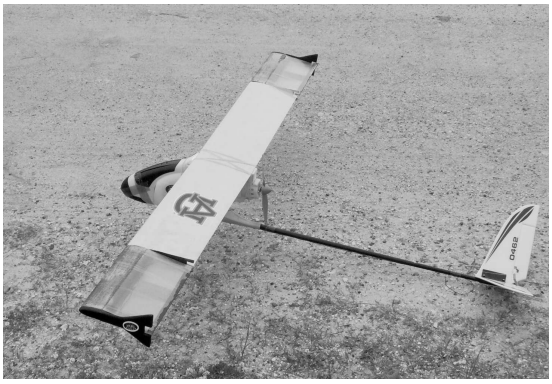

(a) Ready for take off

(b) First take off

(c) Increasing tail load

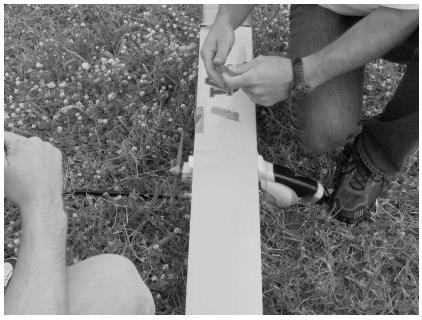

(d) Repairing trailing edge

(e) Successful take off

(f) In flight

Figure 5.23: Flight testing.

The wing panel is tested in the Dobbinga Vertical Wind Tunnel of the TU Delft. The panel is positioned with the leading edge pointing downwards into the airflow. A balance, attached to the wing measures the lift force. Deflections of the trailing edge are measured by a scale which is attached to the inside of one of the endplates. Voltages are kept track of by a voltmeter. Angle of attack can be easily altered by rotating the wing over its longitudinal axis. Air velocity is measured by a pitot tube at the exit of the tunnel. Figure 5.24-b depicts the wing in the test configuration over the wind tunnel.

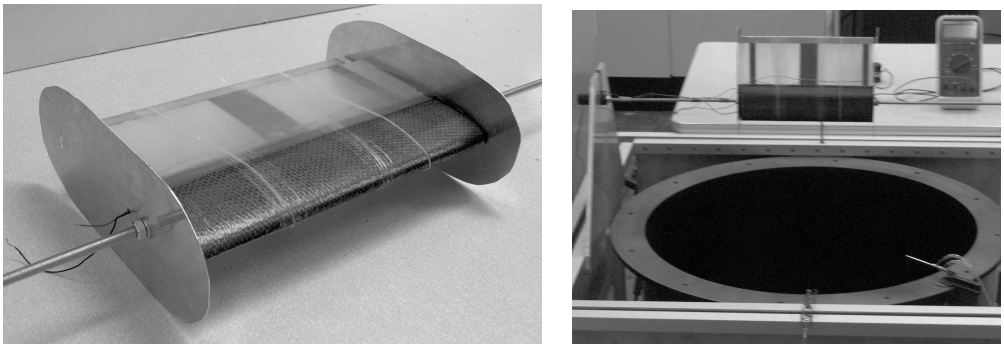

(a) Wind tunnel test article. (b) Test setup in wind tunnel.

Figure 5.24: Wind tunnel test.

Wind tunnel measurements were taken on July 12^{th} 2005. The wing was being positioned at seven different angles of attack, from $-15°$ to $+15°$ in steps of $5°$. At each position a voltage sweep was carried out from +100V to -100V in steps of 10V. At each voltage point both lift force and deflection were recorded. From these parameters a relation is plotted between the lift coefficient and the deflection, δ, of the piezoelectric actuator in figure 5.25. The angle δ is the same as was used in section 5.2.2 and is equal to δ_0 as defined in figure 4.3.

From figure 5.25 shows seven more or less parallel lines that represent the change in lift coefficient due to the shape change of the wing. The attempt to do a two dimensional wind tunnel test on this wing panel partly failed because slots remained present between the end plates and the wing in order to let the wing deform with obstruction of the plates. Therefore the slope of the lines should be corrected. The expression for the two dimensional lift curve slope as a function of δ, C_{l_δ} can now be expressed using the reduced Polhamus equation [20]:

$$C_{l_\delta} = \frac{2 + \sqrt{A^2 + 4}}{A} C_{L_\delta}$$

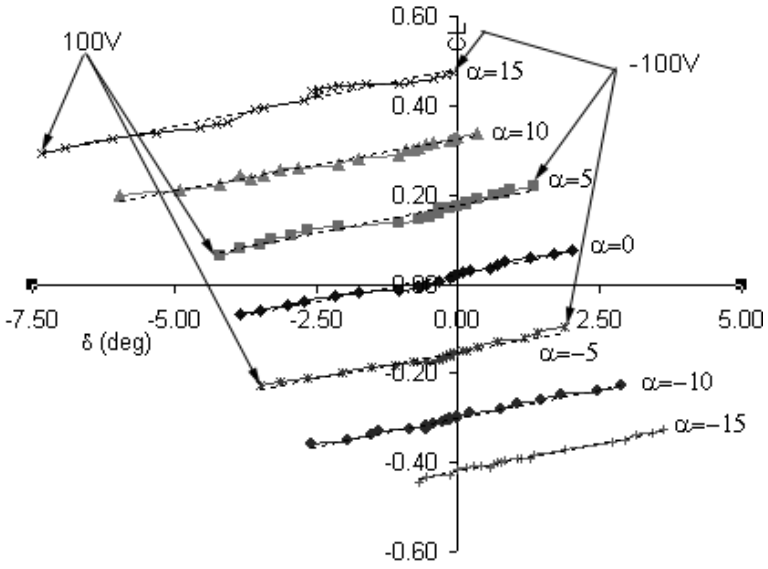

Figure 5.25: End rotation of PBP versus lift coefficient.

Substituting for $A = \frac{b}{c} = \frac{230}{145} = 1.59$, and $C_{L_\delta} = 1.42$ $[1/rad]$ (average value over all angles of attack) yields: $C_{l_\delta} = 4.06$ $[1/rad]$. At $\alpha = 5$ the predicted $C_{l_\delta} = 3.94$ $[1/rad]$ (cf. section 5.2.2) whereas the wind tunnel experiment shows that $C_{l_\delta} = 4.16$ $[1/rad]$. The discrepancy between prediction and experiment is larger at $\alpha = 0$ where it was predicted that $C_{l_\delta} = 5.54$ $[1/rad]$ while in reality it only amounts to $C_{l_\delta} = 3.93$ $[1/rad]$.

From figure 5.25 the influence of the pressure distribution on the deflection of the wing can be seen clearly. At an angle of attack of 15°, the wing is not capable of deflecting in downward anymore. Maximum voltage must be applied to keep the wing at its center position. However, in the other direction the negative pressure helps the wing deflect and much higher deflections than during static bench tests are obtained ($\delta = -5.5°$ in wind tunnel versus $\delta = -3.75°$ at bench test). This effect is caused by the fact that the piezoelectric actuators trade deflection for blocked force and must be taken into consideration when a control system is designed. Increasing the maximum blocked force can be done easily by applying actuators with a larger width. However, this does increase weight so a good trade off is required.

5.8 Synopsis

A thick airfoil morphing wing has been designed, built and flight tested to replace ailerons on a subscale UAV (span = 1.4 m). The outboard parts can

change their camber in order to induce roll control. In total one third of the wing can be actively deformed. A NACA 0012 airfoil has been chosen for the morphing wing section. The leading 40% of the airfoil chord consists of a carbon fibre torque box which transfers the aerodynamic loads from the deforming wing parts to the remaining (static) wing structure. The piezoelectric bending actuators are incorporated on the camber line, over the aft 60% of the airfoil. By using an elastomeric skin, the actuators are being precompressed in order to increase trailing edge deflections. Bench tests on a test article showed that end rotations of the PBP actuator could be increased by a factor of two with respect to the unloaded actuators, up to end rotations of 15° peak to peak. A total new wing was designed and built, incorporating the morphing outboard parts. Flight tests proved that the PBP morphing wing induced excellent roll control. Wind tunnel tests showed an average $C_{L_\delta} = 1.42$, which translates to $C_{l_\delta} = 4.16$ for a two dimensional section of this wing. The presence of wing loading shows a shift in deflection range. At an angle of attack of 15°, the wing is not capable of deflecting downward anymore due to the blocking force of the negative pressure.
(5.21)

Chapter 6

Electronics

Both morphing wing concepts that were discussed in the two previous chapters require the same electronic circuit to power their actuators. The piezoelectric actuators that are used in both these concepts require voltages that range between $+/-100\ V$. Normal electromechanical servo actuators work at $4.8\ V$. Accordingly, a relatively high voltage should be generated out of normal batteries in a very small aircraft. This chapter will present the design, fabrication and testing of the electric circuit.

6.1 Power Consumption

One of the most substantial advantages of using PZT actuators over conventional servo actuators, is their extremely low power consumption. The reason for this lies in the nature of the actuators. They act as capacitors, meaning very little current is actually flowing trough the actuator. The potential between the two electrodes on the PZT sheets is what makes the actuator expand or contract.

The PZT material between the two electrodes of the actuator is a dielectric. The capacitance can be calculated as follows (p. 111 [10]):

$$C = \frac{\epsilon_0 \epsilon_r S_a}{t_a} \tag{6.1}$$

The relative dielectric constant for PZT 5A, $\epsilon_r = 1800\ [-]$. Furthermore, $\epsilon_0 = 8.8542 \cdot 10^{-12}\ [F/m]$, and $t_a = 0.1902\ [mm]$. For the thin wing, the total actuator area amounts to $8,69 \cdot 10^{-3}\ m^2$. Substituting these values yields for a total wing actuator capacitance of 728 nF. The thick wing has a slighter smaller total actuator area ($7.96 \cdot 10^{-3}\ [m^2]$), however, to make a conservative comparison, the actuator area of the thin wing is chosen.

It is assumed that the maximum potential over the individual sheets is $100V$. From the dynamic test, described in section 5.4.3, a corner frequency of 38 Hz is obtained for the non precompressed actuators. Since a conservative estimation of the power consumption is made, this frequency is used.

The consumed power is a product of the applied current (I) and the voltage (V). Using Ohm's law and substituting impedance (Z) for resistance (R) the following can be obtained [7]:

$$P = VI = \frac{V^2}{R} = \frac{V^2}{Z} \tag{6.2}$$

The impedance is a function of the actuator frequency and capacitance (eqn. (10.37) in [10]):

$$Z = \frac{1}{j\omega C} \tag{6.3}$$

Substituting the following values

$$\omega = 2\pi \cdot 38 = 238 \ \ [rad/s] \qquad C = 728 \ \ [nF] \qquad V = 100 \ \ [V]$$

yields a total maximum power consumption of

$$P = 1.73 \ \ [W].$$

To compare this actuator with an average servomechanical actuator of a similar scale and designed for analogous use it is necessary to evaluate their power consumption at equal frequencies. The corner frequency for such a servo actuator is maximally 2 Hz. It draws a constant 5 V and current of 500 mA. This results in a power consumption of $2.5W$. A PZT actuator, actuated at 2 Hz will only consume 0.091 W The proposed piezoceramic actuated morphing wing would therefore represent a power consumption that is only 3.6% that of currently used electromechanical servo actuators. For the thick wing, the power consumption will be even slightly lower than that [7].

6.2 Requirements on the Electronic Circuit

The requirements on the electronic circuit are all very different in nature. Originating from performance, electronics or material perspective, some of the requirements may be conflicting. Consequently, compromises are to be made in order to stay within reasonable boundaries.

The first en most obvious requirement is the fact that the circuit should be able to generate a 100 V potential over the adaptive laminate. Whether this

is done using only a stack of batteries or using a sophisticated is unimportant at the moment. To generate maximum deflection of the piezoelectric laminate this voltage is required.

The second requirement comes from the performance perspective. The electronic circuit, including the batteries, should be as light weight as possible. The circuit creates an electric field over the piezo ceramics.

The third requirement is closely related to the second one and addressed the volume of the electronics. Naturally, a circuit which inhabits all the space in the fuselage is unwanted. One of the reasons to use the piezoelectric actuators in the first places, is the fact that servo motors in the fuselage become obsolete. It would be undesirable to substitute their space with the electronics for the piezoelectric actuators. So, another requirement on the electronics is to make it as small as possible.

From a production point of view there are some additional requirements that are not as strong as the first four, but should be kept in mind during the design process. The size of the components should be such that it can still be handled properly, so not on a miniature scale. The number of components should be minimized. Furthermore, it would be desirable if the batteries that power the electronic circuit could also power the receiver and maybe additional electronics that are to be placed on board the aircraft. The batteries should be either rechargeable or they should last very long. And finally, the components should be commercially available and affordable.

Summing all the above mentioned requirements produces the following circuit. An electronic circuit is required that produces a 100 V electric field, at as low as possible weight and volume. Batteries should also be able to power the additional electronics. Furthermore, everything should be at at a proper size and the batteries should be either rechargeable or very long lasting.

6.3 Design of the Electronic Circuit

6.3.1 High Voltage Generation

There are basically two ways to produce an electric field of 100 V. One is creating a battery of $100V$. Although this may seem odd, it can be a good option when the batteries are small and light. The second option is to use a small stack of batteries, say for example 4 of 1.2 Volts. The resulting 4.8 volts should be amplified with a factor of 20 to get to the required voltage. This second option has been used successfully in the past [5]. To decide which of those two options is best for this application a comparison must be made.

Option one considers two battery packs of 3.6 Volts, each stack containing three 1.2 V rechargeable batteries. Two dc-dc converters are used to amplify the voltage to $^{\pm}65$ V. This means that the potential between the two amounts to 130 V. The weight of each of the batteries is estimated to be 3 grams. The weight of the lightest dc-dc converters amount to 3.5 grams. Consequently, the total weight of this circuit amounts to $6 \cdot 3 + 2 \cdot 3.5 = 25$ $grams$. The volume of the batteries is small. They are about 1.5 cm high and 1 cm in diameter. The converters are about 2 cm^3. Total volume then adds up to approximately 15 cm^3. The circuit is drawn in figure 6.1. The additional capacitors of 10 pF will be very light weight and are not considered here.

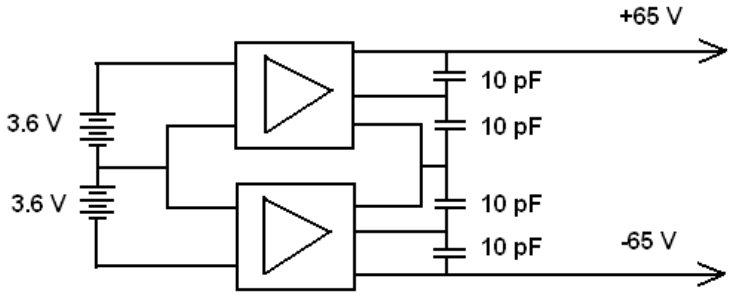

Figure 6.1: The dc-dc converters increase the voltage.

The second option incorporates eight 12 V batteries, together generating a potential of 96 Volts. The 12 Volt batteries are really a stack of eight 1.5 Volt non-rechargeable batteries. So, what is basically done is stacking 64 1.5 Volt batteries together. The weight of each of the batteries amounts to 7 grams. Since no dc-dc converter is required the total weight of this battery stack is $8 \cdot 7 = 56$ $grams$. The batteries are about 3 cm high and 1 cm in diameter. So the entire pack inhabits a space of roughly 30 cm^3.

A third option is added as an interpolation of the first two options. This option incorporates two non-rechargeable 12 Volt batteries and two dc/dc converters. The converters will crank up the voltage to $^{\pm}48V$. Two batteries are required because with one battery it is impossible to impose a ground voltage. In this case the connection between the two batteries functions as ground. The voltage output of the batteries will consequently be $^{\pm}12V$. Total weight of this circuit amounts to 21 $grams$ and the total volume will be about 12 cm^3. The circuit is analogous to the one drawn in figure 6.1 only the input voltage is increased from two times 3.6 V to two times 12 V.

From a weight and volume point of view the last option would be the best, closely followed by the first one (only 4 grams weight difference). Option number two is definitely worse because of the high weight and volume. From

a practical point of view option one has additional benefits over option three. First of all the batteries are rechargeable, so in the long run this will be both less expensive and easier to maintain. Second of all, the 7.2 voltage difference between the batteries could be used to power the receiver of the aircraft. A voltage difference of 12 or 24 volts is not standard to power the receiver and would therefore require additional electronic components or even a separate battery pack. Accordingly option number one is the best compromise between all the requirements.

6.3.2 Amplifying circuit

Apart from generating a high voltage difference, an additional circuit is required to amplify the control signal to this high voltage (compare figure 6.2). The input voltage is generated by the receiver and will be in the order of 5 volts. Amplifying this signal requires so-called operational amplifiers or op-amps.

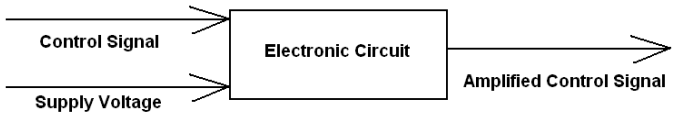

Figure 6.2: The electronic circuit should amplify the control signal.

The way an op-amp amplifies the input signal is clarified using a relevant example. Figure 6.3 gives a schematic representation of the circuit. The triangle in the middle is the symbol of the op-amp. An input signal (V_{in}) of 1.5 Volts is assumed (think of an ordinary Nickel-Cadmium battery). The negative pole of the battery is connected to ground. The supply voltage (V_s) amounts to $\pm 30\ V$. The amount of amplification is determined by the ratio between two resistors in the circuit (compare equation 6.4). However, when the product of the input voltage and the amplification factor exceed the supply voltage, the op-amp saturates and output voltage equals the supply voltage.

$$AR = \frac{R_f}{R_i} \tag{6.4}$$

The resistance $R_i = 2\ [k\Omega]$ and $R_f = 40\ [k\Omega]$. The amplification ratio then amounts to 20 and the output voltage will be -30 Volts, because the op-amp inverts the voltage. This voltage is equal to the supply voltage and the op-amp is saturated.

The output of the op-amp drawn in figure 6.3 is always negative and the maximum range is from zero to the supply voltage. This circuit is capable of

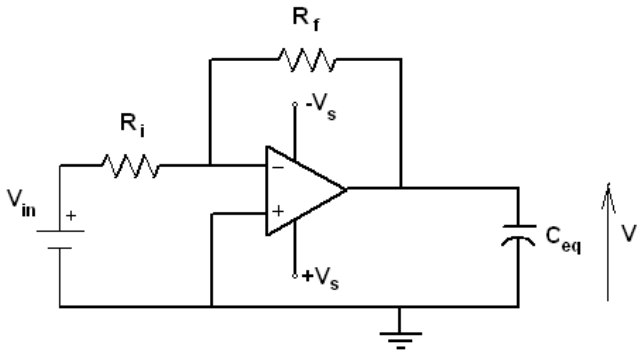

Figure 6.3: Electrical representation of a linear amplifier driving a piezoelectric actuator.

creating an electric field in only one direction over the capacitor (C_{eq}). The direction of this field has been drawn with an arrow pointing upwards. This means that piezoelectric ceramic will be only capable of either contraction or expansion, not both at the same time. In order to be able to create an electric field in the opposite direction, another op-amp should be added to the circuit (figure 6.3.2-a).

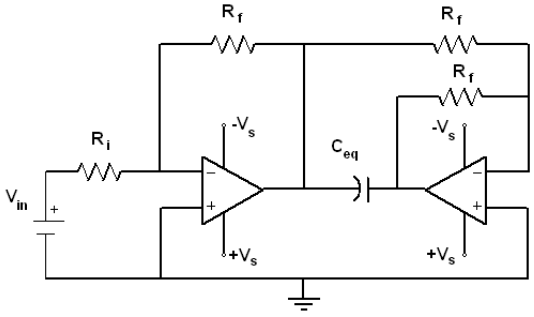

(a) Electrical representation of two linear amplifiers driving a piezoelectric actuator.

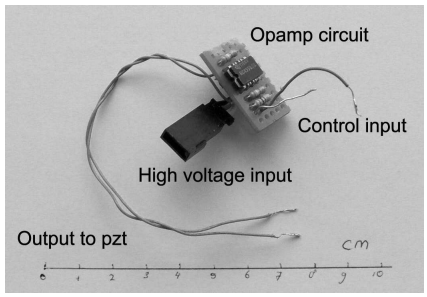

(b) Amplifying circuit including two linear amplifiers.

The circuit drawn in figure 6.3.2-a will be able to let the ceramic expand and contract. Moreover, the potential over the ceramic is now doubled. So the maximum voltage difference amounts to $2V_s$. Assuming a supply voltage of 65 V this would mean a maximum of 130 V. This would be even higher than the de-poling voltage (114 V). Therefore the amplification factor, still determined by equation 6.4, must be determined properly to avoid de-poling.

The amplifying circuit is based on the use of (dual) op-amps. Op-amps are as diverse in specifications as in price. There are op-amps that would

be suitable for this circuit (e.g. APEX PA-41). However, they are very expensive (in the order of 100 Euros), due to their extreme specifications. A disadvantage of this op-amp is the fact that it has a high trickle current. This implies that the circuit will consume a substantial amount of power, even when nothing is being activated. On the other hand there are the TL 741 type of op-amps: cheap, easy to purchase and a low trickle current. The supply voltage of these op-amps is 22 V maximally.

Although the maximum supply voltage is far less than the required supply voltage of 65 V, the TL 741 type op-amps could still be used. This is because the actuators act as a dielectric in a capacitor. This implies that only very little current is drawn, resulting in values two orders of magnitude lower than the maximum allowed current draw. The heat dissipation in the op-amps is the result of internal resistances, R. Since the heat, Q, is proportional to the square of the current ($Q = RI^2$) only little heat is produced [10]. A high voltage in combination with a low current might therefore not be as disastrous for the op-amp as would be expected before hand. There will probably be more heat generated than with a low voltage but this could be dissipated using a dedicated heat sink. Since this scenario has been applied successfully in the past it has proven to be a feasible option [5].

In order to make the amplifying circuit more compact, the two op-amps can be integrated into one IC (integrated circuit). These so-called dual op-amps work exactly the same as two separate op-amps. The circuit as drawn in figure 6.4 remains applicable. However, since two circuits are integrated now, the heat production might be doubled as well. Consequently it must be examined if the dual op-amps can withstand the high voltages. This can only be done by experiment, since there is no data available on overcharged dual op-amps. The op-amp circuit that was made to control the movements of the PBP actuators, only measured $10 \times 10 \times 20$ mm and weighed less than 5 grams (including all wiring and connectors). Figure 6.3.2-b shows a picture of this circuit.

6.3.3 Integration of Components

Integration of the supply voltage circuit and the amplifying circuit does not make the circuit complete. The receiver has been mentioned before, but will now be treated more extensively. The receiver is feeded by a constant voltage from the battery pack. It receives a control signal at a certain frequency (for model airplane the 72 MHz band is often used). It translates the radio signal to a pulsewidth modulated signal. This signal cannot be used as an input for the op-amp because of the pulsewidth nature of it. Accordingly, an additional component should be added to transform this signal into a control signal. Those components are so-called servo controllers and are also integrated in conventional servo motors.

By adding this component to the two circuits, the entire circuit for controlling one piezoceramic is complete. The schematic representation is shown in figure 6.4. Naturally this circuit can be expanded easily to driving a piezoelectric laminate. Then, the circuit drives two piezoelectric elements in parallel. This way, the same circuit can be used to drive one panel of the wing. To control the different panels on the wing independently, only the amplifying circuit and the servo controller have to be copied. The supply circuit can supply a number of op-amps and therefore does not need to be copied.

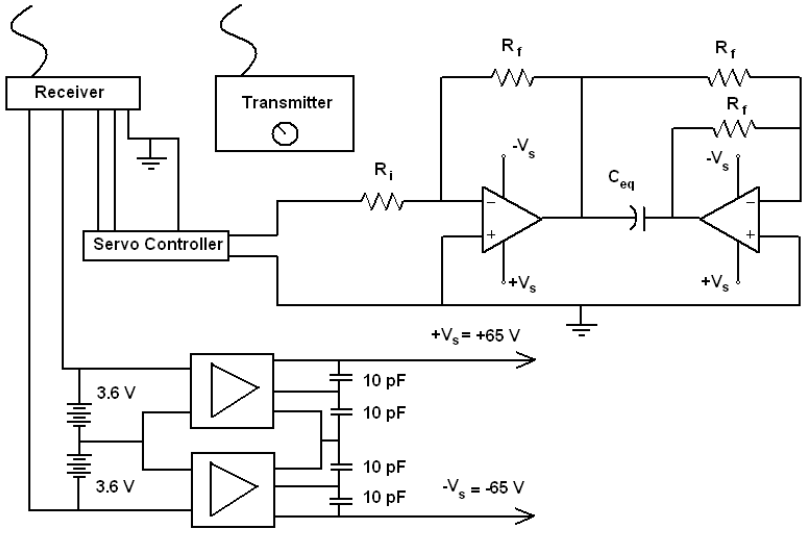

Figure 6.4: Electrical representation of the autonomous circuit driving a piezoelectric actuator.

The wing should be capable of performing roll and direct lift control. The inboard panels of two wings can perform direct lift control, while the output panels can perform roll control. As a first approach, the inboard panels of both wings can operate simultaneously. That implicates that one amplifying circuit is required to operate two panels. This can also be applied to the outboard panels. The only difference is that their deflection must be anti-symmetric. Consequently, only two circuits are required to control all of the control surfaces. In figure 6.5 these two circuits are shortened with "Direct Lift Control" and "Roll Control."

6.4 Flight worthy electronics

When building the electronic circuit as displayed in figure 6.4, a number of problems arose. The first problem had to do the with the pulsewidth

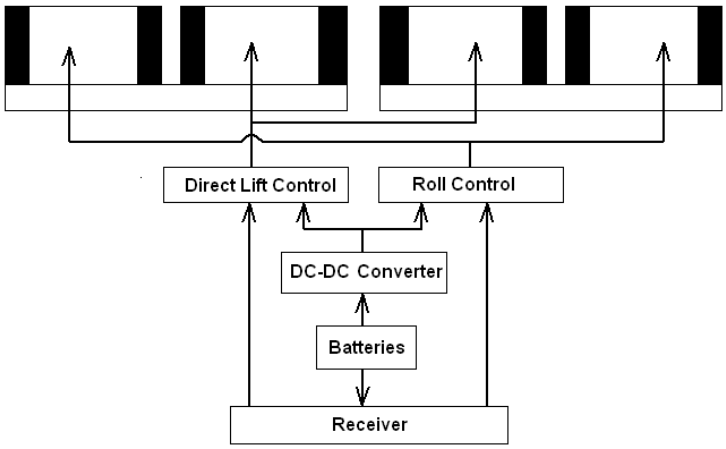

Figure 6.5: All panels of the wing are controlled by two amplifying circuits.

modulated control signal. In order to get a voltage regulated input signal for the op-amp, this control signal should be demodulated. This became a problem since commercial available demodulators come in miniaturized form, which means they cannot be soldered by hand. Using demodulators from existing electronics did not seem to work.

Overheating of the op-amps was another problem. The high voltage caused the op-amp to overheat and eventually the internal circuitry was critically damaged . Using a different type of op-amp, in combination with a heat sink may be the solution to this problem. However, a more fundamental obstacle is the fact that the op-amp dissipates all the energy whether the pzt is activated or not. This takes away the advantage of the low power consumption of pzt actuators with respect to conventional electromechanical servo actuators.

Due to these two problems a new circuit was designed, built and tested. In the new setup the high voltage circuit is electrically separated from the low voltage circuit. The amount of output voltage is controlled by a $100k\Omega$ dual potentiometer which is mechanically linked to a electromechanical servo actuator. The servo actuator is controlled by a 4.8V control signal from the receiver.

The advantages of this circuit are that high voltages can be obtained with almost no losses in the circuit, it is relatively simple to manufacture and it does not require additional elements such as a heat sink. On the other hand, it is relatively big, heavy and the maximum operating frequency is determined by the servo actuator. It is therefore definitely not a well suited circuit for a PBP actuated morphing wing. However, it still is able to control the pzt actuators during flight and with that proof the concept of a piezo-

electrically actuated morphing wing. Figure 6.6 shows all the electronics that were used to power the PBP actuators in the thick wing.

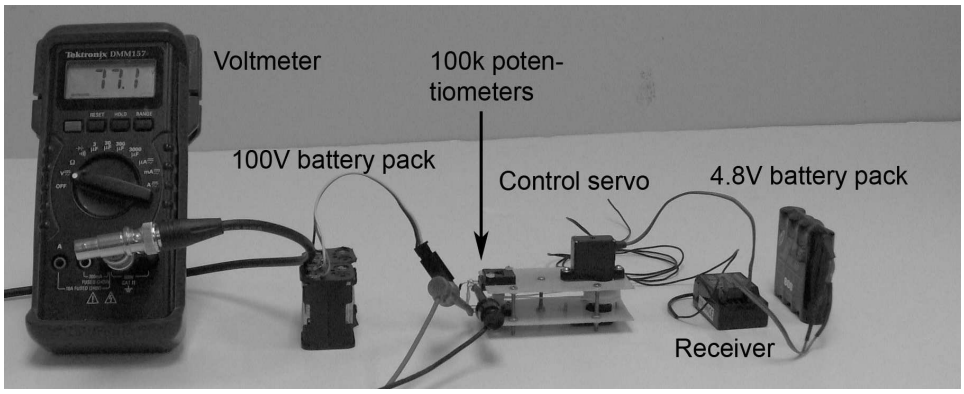

Figure 6.6: Flight worthy electronics prior to integration into the aircraft.

6.5 Synopsis

It has been shown that piezoelectric actuators, integrated in a morphing wing, consume an order of magnitude less power than electro mechanical servo actuators for aileron control. While power consumption is low, a high potential voltage (maximum of +/- 100V) has to be generated to control the PZT sheets. A linear amplifier was used to increase the control signal (4.8V) to this high voltage. A direct current converter was intentioned to increase the supply voltage from the batteries up to a potential difference of 130V. When integrating the electronics two major problems arose: demodulation of the control signal, and overheating of the linear amplifiers. To be able to make flight worthy electronics it was decided to use a 96V battery pack in combination with a dual potentiometer linked to a electro mechanical control servo. This way no interference between the high and low voltage circuit occurred and losses were minimized. On the other hand, the circuit was relatively heavy, big and the maximum operating frequency was determined by the maximum operating frequency of the control servo.

Chapter 7

Conclusions and Recommendations

7.1 Conclusions

It can be concluded that the application of Post-Buckeled Precompressed (PBP) piezoelectric elements in a morphing wing configuration is feasible and has significant benefits over conventional control surface actuation.

PBP actuators It is shown that axial precompression of conventional bimorph piezoelectric bender elements (PBP actuators) can increase end rotations up to a factor of four. Classical Laminate Plate Theory (CLPT) models are shown to capture the behavior of bimorph piezoelectric laminates. A deflection model, employing nonlinear structural relations, is shown to predict the behavior of axially compressed elements very well. A series of actuator specimen were tested to demonstrate the utility of the PBP elements. Advantages of PBP actuators over conventional electro mechanical servo actuators are a substantial reduction in slop, dead band, complexity, power consumption and weight. Moreover, their corner frequency is an order of magnitude higher.

Thin wing A thin airfoil, employing PBP actuators on the aft 70% of the camber line, was designed, built and tested. Precompression of the piezoelectric elements was ensured by using rubber bands at each side of the individual wing panels. A static test article was fabricated in order to verify the lifting capability of the wing. Wind tunnel tests showed a lift curve slope of 3.80 and attached flow up to 15° angle of attack. It has been shown that by using precompression end rotations were increased with almost a factor of 2, up to 14° peak to peak. Wind tunnel tests showed that for

this wing $C_{L_\alpha} = 3.52\ [1/rad]$ and $C_{L_\delta} = 2.97[1/rad]$, which translates to $C_{l_\alpha} = 5.97[1/rad]$ and $C_{l_\delta} = 5.03[1/rad]$ for a two dimensional section of this wing. The maximum lift to drag ratio, $(C_L/C_D)_{max} = 5$. Furthermore, the profile shows a gradual stall behavior, which starts at $\alpha = 18°$.

Thick wing Two morphing wing panels of finite thickness, employing PBP actuators on the aft 60% of the camber line, were designed, built and flight tested on a subscale UAV (span 1.4 m). A NACA 0012 airfoil was used to provide the first 30% of the airfoil shape. Bench tests have shown that by using the skin of the wing to precompress the piezoelectric actuators, trailing edge deflections are increased with a factor of two, up to 15° peak to peak, with respect to the unloaded actuators. A maximum actuation frequency of 34 Hz can be attained. The morphing wing panels were positioned at the outboard side of the wing in order to induce roll control. A carbon fibre torque box was fabricated to transfer aerodynamic loads to the inboard (static) parts of the wing. Flight tests showed excellent control characteristics. Wind tunnel tests measured an average $C_{L_\delta} = 1.42[1/rad]$, which translates to $C_{l_\delta} = 4.16[1/rad]$ for a two dimensional wing section. The presence of wing loading shows a shift in deflection range. At an angle of attack of 15°, the wing is not capable of deflecting downward anymore due to the blocking force of the negative pressure.

Electronics Power consumption of PBP actuators employed in a morphing wing panel has shown to be only 3.6% of the power consumption of their electro mechanical counterparts. An electronic circuit was designed employing linear amplifiers to increase the control signal to the required +/-100V. Due to problems with demodulating the control signal and overheating of the amplifiers it was decided to separate the high voltage circuit from the low voltage control circuit and to link them mechanically. This led to a flight worthy electronic circuit which was suitable to control the morphing wing panels employed on the UAV. However, they were relatively heavy, big and the control frequency was low.

7.2 Recommendations

PBP actuators Further research is needed to increase deflections of the PBP actuator and to make it suitable to integrate in an MAV/UAV control system. Current deflections are limited by the ultimate tensile strain of the PZT sheets. Whenever this limit is surpassed cracks occur at the face of the sheet which makes part of the actuator inactive. Applying thin facing sheets of a very high stiffness at both sides of the actuator will limit the maximum tensile strain of both PZT elements. In this case the maximum

curvatures will not be limited by the PZT sheet that is loaded in tension, but by the compressed PZT sheet. Since PZT has an ultimate compression stress which is an order of magnitude higher than the ultimate tensile stress, much higher curvatures could be attained.

Increasing deflections could also be done by deliberately making cracks in the pzt sheets. The individual panels on the actuator that occur as a result of the cracks should be interconnected by electric wiring. Accordingly, there will be no inactive parts on the PZT sheets. Because of the cracks, the actuator will be able to rotate more and deflections can be increased.

Apart from increasing deflections, integration of the actuators into a control system is one of the most important steps towards a "plug and play" control actuator. At this moment, PBP actuators have open loop control, meaning that a control input correlates with voltage output to the actuators. No information on the amount of deflection is fed back into the control system. Since deflections of the actuator will be different for different airspeeds or air loads, it is important to control the voltage over the actuator in order to ensure that the input deflection is maintained.

Thin wing The main drawback of the thin wing concept is the lack of a physical stop to protect the actuators from over rotating and thus breaking. Hard gusts or heavy landings can cause a the actuators to break very easily. Applying a facing sheet over the elements might be a solution to this problem. This would imply no additional elements would stick out of the wing like for example a trailing edge bump stop would do. Additional wind tunnel tests are necessary to determine the behavior of the wing under aerodynamic loading. Sizing of the piezoelectric elements can be done in conjunction with the obtained results from these tests. This way a more optimal balance can be found between the total mass of the actuators and their performance.

Further wind tunnel tests are required to determine the effect of wing loading on the deflections of the wing. A dynamic test article is required, which can be actuated in the wind tunnel. This wind tunnel experiment should record all the aerodynamic data plus the wing deflection and the voltage input. This requires a measurement method to determine the deflections without obstructing the flow and thereby influencing the aerodynamic measurements. Small strain gauges at the top and bottom of the PZT elements might be a solution for this. The boundary layer is already turbulent over the aft part of the wing, so no danger of separation is present. Moreover, the application of the strain gauges might be the first step towards a closed loop control system for the actuator.

Thick wing It has been proven that using a morphing wing based on a symmetric NACA 0012 airfoil is suitable for roll control on a subscale UAV. A disadvantage of this airfoil is the fact that a relatively high (take off) speed and angle of attack is required to get the aircraft in the air. Furthermore, leading edge separation occurs at a relatively low angle of attack (12°) which makes the wing relatively sensitive to stall. In general, Selig airfoils are very suitable for low Reynolds number wings. However, they are cambered, which make them unsuitable to axially precompress the PBP actuators in the wing. It is suggested to investigate the performance of an airfoil which has the same thickness distribution as such a well performing low Reynolds number airfoil. Camber can be induced actively by deforming the airfoil with the PBP actuators. In practice this will imply an airfoil with a sharper leading edge and a thickest point which is shifted more backwards.

Thorough research is required in the skin material. The hysteresis in the total PBP actuator is being determined mainly by the hysteresis in the skin. During this research, natural rubber was chosen as skin material because it easy to purchase and relatively cheap. However, the natural rubber possesses a large amount of hysteresis (26%), which is undesirable for the actuator.

Electronics Converting direct current of low voltage to 100V is inefficient. Losses will occur in the conversion process which are really hard to overcome. On the other hand, converting from 100V down to a low voltage (e.g. 4.8V) can be done very efficient. To save electrical energy from dissipation it could be efficient for the entire aircraft to have one 100V battery pack to control both the PBP actuators and the additional electronics (e.g. receiver and motor). Instead of using eight 12V (non-rechargeable) batteries it might be more convenient to use small rechargeable Lithium Polymer Cells (3.7V) and put them in series.

In addition, instead of using linear amplifiers (opams) the use of switching amplifiers to control the PBP actuators should be investigated. It has been shown that switching amplifiers can operate very efficiently up to high actuation frequencies [17]. Switching amplifiers control the piezoelectric actuators by sending a pulse signal at very high frequency and constant voltage. By altering the actuation frequency the mean voltage will be changed which can control the actuator. Since switching amplifiers should be custom made, complexity, wight and volume might be substantially higher than for linear amplifiers. A fair comparison between linear amplifiers and switching amplifiers in the low frequency range should be made.

Appendix A

Classical Laminate Plate Theory Model

This appendix will give a more in-depth analysis of the application of the CLPT on the piezoelectric laminate. As stated in chapter 3 the analysis follows the analysis in Jones [12]. The reader must note that not all the subscripts that are used in this section are in conjunction with the subscripts used in chapter two.

A.1 Actuator Dimensions

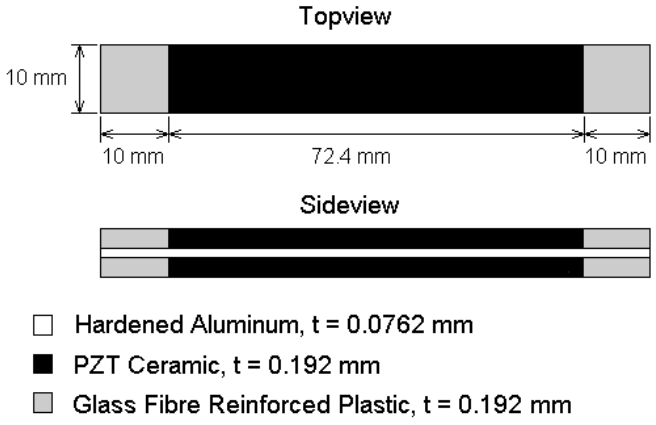

Figure A.1: Actuator dimensions. [18]

Piezoelectric actuator thickness (m):

$$t_a = 0.191 \cdot 10^{-3}$$

Substrate thickness (m):

$$t_s = 0.0762 \cdot 10^{-3}$$

Bonding layer thickness (m):

$$t_b = 0.0635 \cdot 10^{-5}$$

Length of PBP actuator (m):

$$L_0 = 0.0724$$

Total length of the laminate (m):

$$L_{0tot} = 0.0889$$

width of PBP laminate (m):

$$b_{=}0.010$$

A.2 Material Properties

Material properties PZT-5A

Stiffness (Pa):

$$E_{a1} = 61 \cdot 10^9 \quad E_{a2} = 61 \cdot 10^9 \quad G_{a12} = 23 \cdot 10^9$$

$$\mu_{a12} = 0.3 \quad \mu_{a21} = 0.3$$

Thermal expansion coefficients:

$$\alpha_{a1} = 9 \cdot 10^{-6} \quad \alpha_{a2} = 9 \cdot 10^{-6}$$

Piezoelectric charge coefficients (m/V):

$$d_{31_{lina}} = -115 \cdot 10^{-12} \qquad d_{31_{linb}} = -3.27 \cdot 10^{-16}$$
$$d_{32_{lina}} = -115 \cdot 10^{-12} \qquad d_{32_{linb}} = -3.27e \cdot 10^{-16}$$

Orientation of the actuator:

$$\theta_{a1} = 0 \quad \theta_{a2} = 0$$

Material properties of the Al 6064 substrate

Stiffness (Pa):

$$E_{s1} = 100 \cdot 10^9 \quad E_{s2} = 100 \cdot 10^9 \quad G_{s12} = 38.5 \cdot 10^9$$

$$\mu_{s12} = 0.3 \quad \mu_{s21} = 0.3$$

Thermal expansion coefficients:

$$\alpha_{s1} = 22.05 \cdot 10^{-6} \quad \alpha_{s2} = 22.05 \cdot 10^{-6}$$

Orientation of the substrate:

$$\theta_s = 0$$

Material properties of the bonding layer

Stiffness (Pa):

$$E_b = 1 \cdot 10^9 \quad G_b = 0.4 \cdot 10^9 \quad \mu_b = 0.3$$

A.3 Stress-strain relations for plane stress in each lamina

PZT stiffness matrix components

$$Q_{xxa} = \frac{E_{a1}}{1 - \mu_{a12}\mu_{a21}} \qquad Q_{xya} = \frac{\mu_{a12}E_{a2}}{1 - \mu_{a12}\mu_{a21}}$$
$$Q_{yya} = \frac{E_{a2}}{1 - \mu_{a12}\mu_{a21}} \qquad Q_{zza} = G_{a12}$$

Rotated stiffness matrix components of upper piezoelectric element

$$\overline{Q}_{11a1} = Q_{xxa}cos^4(\theta_{a1}) + 2(Q_{xya} + 2Q_{zza})sin^2(\theta_{a1})cos^2(\theta_{a1}) + Q_{yya}sin^4(\theta_{a1})$$
$$\overline{Q}_{12a1} = (Q_{xxa} + Q_{yya} - 4Q_{zza})sin^2(\theta_{a1})cos^2(\theta_{a1}) + Q_{xya}(sin^4(\theta_{a1}) + cos^4(\theta_{a1}))$$
$$\overline{Q}_{22a1} = Q_{xxa}sin^4(\theta_{a1}) + 2(Q_{xya} + 2Q_{zza})sin^2(\theta_{a1})cos^2(\theta_{a1}) + Q_{yya}cos^4(\theta_{a1})$$
$$\overline{Q}_{16a1} = (Q_{xxa} - Q_{xya} - 2Q_{zza})sin(\theta_{a1})cos^3(\theta_{a1}) + (Q_{xya} - Q_{yya} + 2Q_{zza})sin^3(\theta_{a1})cos(\theta_{a1})$$
$$\overline{Q}_{26a1} = (Q_{xxa} - Q_{xya} - 2Q_{zza})sin^3(\theta_{a1})cos(\theta_{a1}) + (Q_{xya} - Q_{yya} + 2Q_{zza})sin(\theta_{a1})cos^3(\theta_{a1})$$
$$\overline{Q}_{66a1} = (Q_{xxa} + Q_{yya} - 2Q_{xya} - 2Q_{zza})sin^2(\theta_{a1})cos^2(\theta_{a1}) + Q_{zza}(sin^4(\theta_{a1}) + cos^4(\theta_{a1}))$$

Rotated stiffness matrix components of lower piezoelectric element

$$\overline{Q}_{11a2} = Q_{xxa}cos^4(\theta_{a2}) + 2(Q_{xya} + 2Q_{zza})sin^2(\theta_{a2})cos^2(\theta_{a2}) + Q_{yya}sin^4(\theta_{a2})$$
$$\overline{Q}_{12a2} = (Q_{xxa} + Q_{yya} - 4Q_{zza})sin^2(\theta_{a2})cos^2(\theta_{a2}) + Q_{xya}(sin^4(\theta_{a2}) + cos^4(\theta_{a2}))$$
$$\overline{Q}_{22a2} = Q_{xxa}sin^4(\theta_{a2}) + 2(Q_{xya} + 2Q_{zza})sin^2(\theta_{a2})cos^2(\theta_{a2}) + Q_{yya}cos^4(\theta_{a2})$$
$$\overline{Q}_{16a2} = (Q_{xxa} - Q_{xya} - 2Q_{zza})sin(\theta_{a2})cos^3(\theta_{a2}) + (Q_{xya} - Q_{yya} + 2Q_{zza})sin^3(\theta_{a2})cos(\theta_{a2});$$
$$\overline{Q}_{26a2} = (Q_{xxa} - Q_{xya} - 2Q_{zza})sin^3(\theta_{a2})cos(\theta_{a2}) + (Q_{xya} - Q_{yya} + 2Q_{zza})sin(\theta_{a2})cos^3(\theta_{a2});$$
$$\overline{Q}_{66a2} = (Q_{xxa} + Q_{yya} - 2Q_{xya} - 2Q_{zza})sin^2(\theta_{a2})cos^2(\theta_{a2}) + Q_{zza}(sin^4(\theta_{a2}) + cos^4(\theta_{a2}))$$

Substrate stiffness matrix components:

$$Q_{xxs} = \frac{E_{s1}}{1-\mu_{s12}\mu_{s21}} \qquad Q_{xys} = \frac{\mu_{s12}E_{s2}}{1-\mu_{s12}\mu_{s21}}$$
$$Q_{yys} = \frac{E_{s2}}{1-\mu_{s12}\mu_{s21}} \qquad Q_{zzs} = G_{s12};$$

Rotated stiffness matrix components:

$$\overline{Q}_{11s} = Q_{xxs}cos^4(\theta_s) + 2(Q_{xys} + 2Q_{zzs})sin^2(\theta_s)cos^2(\theta_s) + Q_{yys}sin^4(\theta_s)$$
$$\overline{Q}_{12s} = (Q_{xxs} + Q_{yys} - 4Q_{zzs})sin^2(\theta_s)cos^2(\theta_s) + Q_{xys}(sin^4(\theta_s) + cos^4(\theta_s))$$
$$\overline{Q}_{22s} = Q_{xxs}sin^4(\theta_s) + 2(Q_{xys} + 2Q_{zzs})sin^2(\theta_s)cos^2(\theta_s) + Q_{yys}cos^4(\theta_s)$$
$$\overline{Q}_{16s} = (Q_{xxs} - Q_{xys} - 2Q_{zzs})sin(\theta_s)cos^3(\theta_s) + (Q_{xys} - Q_{yys} + 2Q_{zzs})sin^3(\theta_s)cos(\theta_s)$$
$$\overline{Q}_{26s} = (Q_{xxs} - Q_{xys} - 2Q_{zzs})sin^3(\theta_s)cos(\theta_s) + (Q_{xys} - Q_{yys} + 2Q_{zzs})sin(\theta_s)cos^3(\theta_s)$$
$$\overline{Q}_{66s} = (Q_{xxs} + Q_{yys} - 2Q_{xys} - 2Q_{zzs})sin^2(\theta_s)cos^2(\theta_s) + Q_{zzs}(sin^4(\theta_s) + cos^4(\theta_s))$$

Bonding layer stiffness matrix components (always considered isotropic therefore no rotation required):

$$\overline{Q}_{11b} = \frac{E_b}{1-\mu_b^2}$$
$$\overline{Q}_{12b} = \frac{\mu_b E_b}{1-\mu_b^2}$$
$$\overline{Q}_{22b} = Q_{11b}$$
$$\overline{Q}_{66b} = G_b$$
$$\overline{Q}_{16b} = 0$$
$$\overline{Q}_{26b} = 0$$

A.4 Resultant Laminate Forces and Moments

Thickness definitions:

$$t_1 = t_s/2 + t_b + t_a \qquad t_2 = t_s/2 + t_b \qquad t_3 = t_s/2$$
$$t_4 = -t_s/2 \qquad t_5 = -t_s/2 - t_b \qquad t_6 = -t_s/2 - t_b - t_a$$

Determination of the ABD matrix elements:

$$A_{ij_{a1}} = (\overline{Q}_{ij})_{a1}(t_1 - t_2)$$
$$B_{ij_{a1}} = \frac{1}{2}(\overline{Q}_{ij})_{a1}(t_1^2 - t_2^2)$$
$$D_{ij_{a1}} = \frac{1}{3}(\overline{Q}_{ij})_{a1}(t_1^3 - t_2^3)$$

$$A_{ij_{a2}} = (\overline{Q}_{ij})_{a2}(t_5 - t_6)$$
$$B_{ij_{a2}} = \frac{1}{2}(\overline{Q}_{ij})_{a2}(t_5^2 - t_6^2)$$
$$D_{ij_{a2}} = \frac{1}{3}(\overline{Q}_{ij})_{a2}(t_5^3 - t_6^3)$$

$$A_{ij_{b1}} = (\overline{Q}_{ij})_{b1}(t_2 - t_3)$$
$$B_{ij_{b1}} = \frac{1}{2}(\overline{Q}_{ij})_{b1}(t_2^2 - t_3^2)$$
$$D_{ij_{b1}} = \frac{1}{3}(\overline{Q}_{ij})_{b1}(t_2^3 - t_3^3)$$

$$A_{ij_{b2}} = (\overline{Q}_{ij})_{b2}(t_4 - t_5)$$
$$B_{ij_{b2}} = \frac{1}{2}(\overline{Q}_{ij})_{b2}(t_4^2 - t_5^2)$$
$$D_{ij_{b2}} = \frac{1}{3}(\overline{Q}_{ij})_{b2}(t_4^3 - t_5^3)$$

$$A_{ij_s} = (\overline{Q}_{ij})_s(t_3 - t_4)$$
$$B_{ij_s} = \frac{1}{2}(\overline{Q}_{ij})_s(t_3^2 - t_4^2)$$
$$D_{ij_s} = \frac{1}{3}(\overline{Q}_{ij})_s(t_3^3 - t_4^3)$$

Actuator ABD-matrices:

$$A_{a1} = \begin{bmatrix} A_{11a1} & A_{12a1} & A_{16a1} \\ A_{12a1} & A_{22a1} & A_{26a1} \\ A_{16a1} & A_{26a1} & A_{66a1} \end{bmatrix} \quad A_{a2} = \begin{bmatrix} A_{11a2} & A_{12a2} & A_{16a2} \\ A_{12a2} & A_{22a2} & A_{26a2} \\ A_{16a2} & A_{26a2} & A_{66a2} \end{bmatrix}$$

$$B_{a1} = \begin{bmatrix} B_{11a1} & B_{12a1} & B_{16a1} \\ B_{12a1} & B_{22a1} & B_{26a1} \\ B_{16a1} & B_{26a1} & B_{66a1} \end{bmatrix} \quad B_{a2} = \begin{bmatrix} B_{11a2} & B_{12a2} & B_{16a2} \\ B_{12a2} & B_{22a2} & B_{26a2} \\ B_{16a2} & B_{26a2} & B_{66a2} \end{bmatrix}$$

$$D_{a1} = \begin{bmatrix} D_{11a1} & D_{12a1} & D_{16a1} \\ D_{12a1} & D_{22a1} & D_{26a1} \\ D_{16a1} & D_{26a1} & D_{66a1} \end{bmatrix} \quad D_{a2} = \begin{bmatrix} D_{11a2} & D_{12a2} & D_{16a2} \\ D_{12a2} & D_{22a2} & D_{26a2} \\ D_{16a2} & D_{26a2} & D_{66a2} \end{bmatrix}$$

Bonding layer ABD-matrices:

$$A_{b1} = \begin{bmatrix} A_{11b1} & A_{12b1} & A_{16b1} \\ A_{12b1} & A_{22b1} & A_{26b1} \\ A_{16b1} & A_{26b1} & A_{66b1} \end{bmatrix} \quad A_{b2} = \begin{bmatrix} A_{11b2} & A_{12b2} & A_{16b2} \\ A_{12b2} & A_{22b2} & A_{26b2} \\ A_{16b2} & A_{26b2} & A_{66b2} \end{bmatrix}$$

$$B_{b1} = \begin{bmatrix} B_{11b1} & B_{12b1} & B_{16b1} \\ B_{12b1} & B_{22b1} & B_{26b1} \\ B_{16b1} & B_{26b1} & B_{66b1} \end{bmatrix} \quad B_{b2} = \begin{bmatrix} B_{11b2} & B_{12b2} & B_{16b2} \\ B_{12b2} & B_{22b2} & B_{26b2} \\ B_{16b2} & B_{26b2} & B_{66b2} \end{bmatrix}$$

$$D_{b1} = \begin{bmatrix} D_{11b1} & D_{12b1} & D_{16b1} \\ D_{12b1} & D_{22b1} & D_{26b1} \\ D_{16b1} & D_{26b1} & D_{66b1} \end{bmatrix} \quad D_{b2} = \begin{bmatrix} D_{11b2} & D_{12b2} & D_{16b2} \\ D_{12b2} & D_{22b2} & D_{26b1} \\ D_{16b2} & D_{26b2} & D_{66b2} \end{bmatrix}$$

Substrate ABD-matrices:

$$A_s = \begin{bmatrix} A_{11s} & A_{12s} & A_{16s} \\ A_{12s} & A_{22s} & A_{26s} \\ A_{16s} & A_{26s} & A_{66s} \end{bmatrix} \quad B_s = \begin{bmatrix} B_{11s} & B_{12s} & B_{16s} \\ B_{12s} & B_{22s} & B_{26s} \\ B_{16s} & B_{26s} & B_{66s} \end{bmatrix}$$

$$D_s = \begin{bmatrix} D_{11s} & D_{12s} & D_{16s} \\ D_{12s} & D_{22s} & D_{26s} \\ D_{16s} & D_{26s} & D_{66s} \end{bmatrix}$$

Laminate ABD-matrices:

$$\begin{aligned} A_l &= A_{a1} + A_{a2} + A_{b1} + A_{b2} + A_s \\ B_l &= B_{a1} + B_{a2} + B_{b1} + B_{b2} + B_s \\ D_l &= D_{a1} + D_{a2} + D_{b1} + D_{b2} + D_s \end{aligned}$$

Complete ABD-matrices:

$$ABD_{a1} = \begin{bmatrix} A_{a1} & B_{a1} \\ B_{a1} & D_{a1} \end{bmatrix} \quad ABD_{a2} = \begin{bmatrix} A_{a2} & B_{a2} \\ B_{a2} & D_{a2} \end{bmatrix}$$

$$ABD_{b1} = \begin{bmatrix} A_{b1} & B_{b1} \\ B_{b1} & D_{b1} \end{bmatrix} \quad ABD_{b2} = \begin{bmatrix} A_{b2} & B_{b2} \\ B_{b2} & D_{b2} \end{bmatrix}$$

$$ABD_s = \begin{bmatrix} A_s & B_s \\ B_s & D_s \end{bmatrix} \quad ABD_l = \begin{bmatrix} A_l & B_l \\ B_l & D_l \end{bmatrix}$$

A.5 Actuation

Thermal loading

In-plane Thermal strains

$$
\begin{aligned}
T_{1a1} &= \alpha_{a1} dT sin^2(\theta_{a1}) + \alpha_{a2} dT cos^2(\theta_{a1}) \\
T_{2a1} &= \alpha_{a2} dT sin^2(\theta_{a1}) + \alpha_{a1} dT cos^2(\theta_{a1}) \\
T_{3a1} &= \frac{1}{2}(\alpha_{a1} dT - \alpha_{a2} dT) sin(2\theta_{a1}) \\
T_{1a2} &= \alpha_{a1} dT sin^2(\theta_{a2}) + \alpha_{a2} dT cos^2(\theta_{a2}) \\
T_{2a2} &= \alpha_{a2} dT sin^2(\theta_{a2}) + \alpha_{a1} dT cos^2(\theta_{a2}) \\
T_{3a2} &= \frac{1}{2}(\alpha_{a1} dT - \alpha_{a2} dT) sin(2\theta_{a2}) \\
T_{1s} &= \alpha_{s1} dT sin^2(\theta_s) + \alpha_{s2} dT cos^2(\theta_s) \\
T_{2s} &= \alpha_{s2} dT sin^2(\theta_s) + \alpha_{s1} dT cos^2(\theta_s) \\
T_{3s} &= \frac{1}{2}(\alpha_{s1} dT - \alpha_{s2} dT) sin(2\theta_s)
\end{aligned}
$$

$$
T_{a1} = \begin{bmatrix} T_{1a1} \\ T_{2a1} \\ T_{3a1} \\ 0 \\ 0 \\ 0 \end{bmatrix} \quad T_{a2} = \begin{bmatrix} T_{1a2} \\ T_{2a2} \\ T_{3a2} \\ 0 \\ 0 \\ 0 \end{bmatrix} \quad T_s = \begin{bmatrix} T_{1s} \\ T_{2s} \\ T_{3s} \\ 0 \\ 0 \\ 0 \end{bmatrix}
$$

Strains:

$$
\begin{aligned}
\epsilon_{T11a1} &= T_{1a1} \\
\epsilon_{T11a2} &= T_{1a2} \\
\epsilon_{Ts11} &= T_{1s}
\end{aligned}
$$

Electrical loading

Polarization of the piezoelectric elements:

$$p_1 = 1$$

$$p_2 = -1$$

Determination of the electrical strain coefficients:

$$d_{31} = d_{31_{lina}} + d_{31_{linb}}(V_3/t_a)$$

$$d_{32} = d_{32_{lina}} + d_{32_{linb}}(V_3/t_a)$$

Piezoelectric element strain caused by electrical field in upper piezoelectric element:

$$\Lambda_{311} = \frac{p_1 V_3 d_{31}}{t_a} sin^2(\theta_{a1}) + \frac{p_1 V_3 d_{32}}{t_a} cos^2(\theta_{a1})$$

$$\Lambda_{321} = \frac{p_1 V_3 d_{32}}{t_a} sin^2(\theta_{a1}) + \frac{p_1 V_3 d_{31}}{t_a} cos^2(\theta_{a1})$$

$$\Lambda_{361} = \frac{1}{2}\Big(\frac{p_1 V_3 d_{31}}{t_a} - \frac{p_1 V_3 d_{32}}{t_a}\Big) sin(2\theta_{a1})$$

Total electrical strain vector upper element:

$$\Lambda_{a31} = \begin{bmatrix} \Lambda_{311} \\ \Lambda_{321} \\ \Lambda_{361} \\ 0 \\ 0 \\ 0 \end{bmatrix}$$

Piezoelectric element strain caused by electrical field in lower piezoelectric element:

$$\Lambda_{312} = \frac{p_2 V_3 d_{31}}{t_a} sin^2(\theta_{a2}) + \frac{p_2 V_3 d_{32}}{t_a} cos^2(\theta_{a2})$$

$$\Lambda_{322} = \frac{p_2 V_3 d_{32}}{t_a} sin^2(\theta_{a2}) + \frac{p_2 V_3 d_{31}}{t_a} cos^2(\theta_{a2})$$

$$\Lambda_{362} = \frac{1}{2}\Big(\frac{p_2 V_3 d_{31}}{t_a} - \frac{p_2 V_3 d_{32}}{t_a}\Big) sin(2\theta_{a2})$$

Piezoelectric element strain vector lower element

$$\Lambda_{a32} = \begin{bmatrix} \Lambda_{312} \\ \Lambda_{322} \\ \Lambda_{362} \\ 0 \\ 0 \\ 0 \end{bmatrix}$$

Resultant Strain

$$\begin{bmatrix} A_l & B_l \\ B_l & D_l \end{bmatrix} \begin{pmatrix} \epsilon \\ \kappa \end{pmatrix}_l = \begin{bmatrix} A_{a1} & B_{a1} \\ B_{a1} & D_{a1} \end{bmatrix} \Lambda_{a31} + \begin{bmatrix} A_{a2} & B_{a2} \\ B_{a2} & D_{a2} \end{bmatrix} \Lambda_{a32} + \begin{bmatrix} A_{a1} & B_{a1} \\ B_{a1} & D_{a1} \end{bmatrix} T_{a1} + \begin{bmatrix} A_{a2} & B_{a2} \\ B_{a2} & D_{a2} \end{bmatrix} T_{a2} + \begin{bmatrix} A_s & B_s \\ B_s & D_s \end{bmatrix} T_s$$

Appendix B

PBP Simulation

In this appendix an exact copy of the Matlab code that was used to solve equation 3.47 is presented [3].

```
clc clear close all

format short

% Everything in this m-file is based on equation 18 of SPIE paper no 5762-16
% 'Post-buckled precompressed (PBP) benders: a new class of grid-fin
% actuators enhancing high speed autonomous VTOL MAV's'

PZT_5A

% actuator dimensions:
% Lay-up:
ta = 0.191e-3           ;% piezo actuator thickness (m)
ts = 0.0762e-3          ;% substrate thickness (m)
tb = 0.0635e-5          ;% bonding layer thickness (m)
% PBP dimensions
L0 = 0.0724             ;% length of piezo actuator (m)
L0tot = 0.0889          ;% length of flex spar (m)
b=0.010                 ;% width of PBP laminate element [m]

for V3=[20 40 60 70 80 90 100]; % Input Voltage
E3=V3/(ta+tb);                  % Electric field (V/m)
d31lin= -(d31lina + d31linb*E3);% Piezoelectric constant (m/V)
Lambda =d31lin*E3;              % Free strain actuator

% Pre-compressive force
Fcr=6.18;                   % buckling load [N]
```

```
Fcrgmf=Fcr/0.009808;        % buckling load [gmf]
for i=0.001:0.1587/2:1
Fagmf=i*Fcrgmf;             % pre-compression force [gmf]
Fa=i*Fcr;                   % pre-compression force [N]

% Correction factors
C1=(-3.2e-3)*V3+0.76; C2=((4e-3)*V3+1.25)*C1;

% Definition of the D and B components:
B= C1*(Ea1*(ts*ta+2*tb*ta+ta^2));
D= C2*((Es1*ts^3)/12+Ea1*((ta*(ts+2*tb)^2)/2+(ts+2*tb)*ta^2+ (2/3)*ta^3));

% Initial Curvature [rad/m] (without pre-compression):
kappa=(B/D)*Lambda;

% Left side of equation 18:
sol1=(L0/2)*sqrt(Fa/(D*b));

% Initial values:
sol2=0;
delta0=0;               % [rad]

% Finding delta0 which compares to the given pre-compressive force
for counter=1:10000 if sol1>sol2;
    delta0=delta0+.0005;

% Right side of equation 18
dxi=pi/200; xi=(0:dxi:pi/2);
f=(sin(delta0./2)).*(cos(xi))./(sqrt(((sin(delta0./2)).^2).*(cos(xi)).^2+...
 ((kappa.^2).*D.*b)/(4.*Fa)).*sqrt(1-((sin(delta0./2)).^2).*(sin(xi)).^2));
ff=f*dxi; sol2=sum(ff); end end

delta0=delta0*180/pi;

end end

plot(delta0,Fagmf,'.')
xlabel('Rotation, delta0 (1/2 peak to peak) (deg)')
ylabel('Axial force (gmf)')
title('Axial force vs. Rotation') axis([0 5 0 600]) hold on
```

Appendix C

Leading Edge Geometry

Before Xfoil can be used, the shape of the leading edge must be mathematically determined. Figure C.1 shows how the leading edge contour is divided into three different parts. The top-front part is being represented by a quarter part of an ellipse:

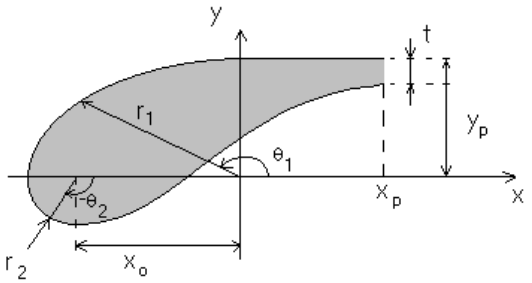

Figure C.1: Definition of the leading edge geometry of the airfoil.

$$x_1 = a\cos\theta_1, \qquad \pi/2 < \theta_1 < \pi$$
$$y_1 = b\sin\theta_1$$
$$a = x_0 + r_2, \qquad b = y_p$$

A quarter circle marks the bottom side of the leading edge contour:

$$x_2 = r_2\cos\theta_2 - x_0, \qquad \pi < \theta_2 < 3\pi/2$$
$$y_2 = r_2\sin\theta_2$$

The last line is the aft part of the leading edge. This is represented as an inverse cosine shape:

$$y_3 = d + A\cos(\frac{x + x_0}{x_p + x_o}\pi)$$

$$A = \frac{y_p - t + r_1}{2}, \quad d = A - r_1$$

These three curves together determine the shape of the leading edge. In order to change the shape, essentially four variables can be altered: x_0, x_p, r_2, and y_p. As stated in the first paragraph of this section, the leading edge can be maximally 30% of the entire chord (c) of the airfoil. If it was to be made larger, there would not be much left of the morphing wing concept. The design would then degenerate to an ordinary wing with a fancy flapping mechanism for roll and direct lift control. That is not the goal of this investigation. Consequently one of the constraints is:

$$r_2 + x_0 + x_p < 0.30 \cdot c \tag{C.1}$$

As established in the preliminary design, the length of the flat part of the airfoil amounts to 82 mm. Consequently, the maximum length of the leading edge amounts to 34 mm. The maximum thickness of the leading edge, determined by adding the value of y_p and r_2, is unconstrained. However, for practical purposes the investigation is limited to a maximum of 15% of the chord length:

$$r_2 + y_p < 0.15 \cdot c \tag{C.2}$$

In practice this means that the maximum thickness of the leading edge is 17 mm. All variables represent distances, so a final set of constraints can be added:

$$x_0, x_p, r_2, t_p > 0 \tag{C.3}$$

Appendix D

Trailing Edge Analysis

The function of the trailing edges of the thin airfoil wing is threefold. It has to provide an aerodynamically favorable end of the airfoil. It has to transfer the precompression force to the adaptive laminates. And, it provides a frame for the flexible aluminum skin. The first of these functions dictates a thin, sharp trailing edge. This is not much of a problem, since the aft part of the wing is not thicker as 0.5 mm. The load introduction of the precompression force on the adaptive laminates does require some more thought.

The buckling load for a 2 cm wide element amounts to 11.5 N [8]. If a precompression of 90% of the buckling load is applied, that means that each rubber band must apply a force of 10.4 N. The load on the laminates is being introduced, using thin steel rods (diameter: 0.5 mm). When only this rod would be applied, the PZT laminates would be asymmetrically loaded (compare figure D.1). To counteract this undesirable effect, a broader beam is required.

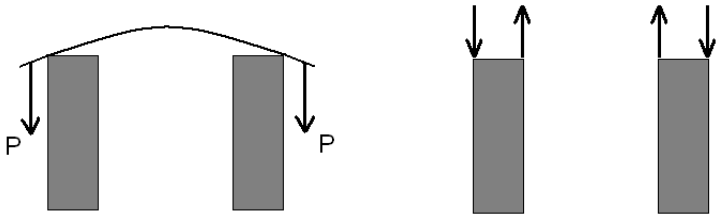

(a) Deflection (b) Force

Figure D.1: Asymmetric loading of the adaptive laminate.

In the preliminary design a trailing edge with a width of 1 cm is proposed. A thickness of 0.5 mm would make the trailing edge as thick as the adaptive laminate. A glass fibre reinforced polymer is chosen as trailing edge material. The calculations in this section will show that such a trailing edge will be stiff enough to assume it to be rigid. Figure D.2 shows a side view on the adaptive part of the airfoil. The airfoil is deflected over a certain angle, δ. The angle θ is larger than δ, causing an out of plane force on the trailing edge, P'. The difference between both angles, Δ, determines the value of P'. For large tip deflections ($6.4mm$ is assumed to be the maximum), Δ amounts to 3.2 *degrees*. The in-plane force will consequently almost be equal to P, while the out of plane force, $P' = P\cos\Delta = 0.66$ $[N]$.

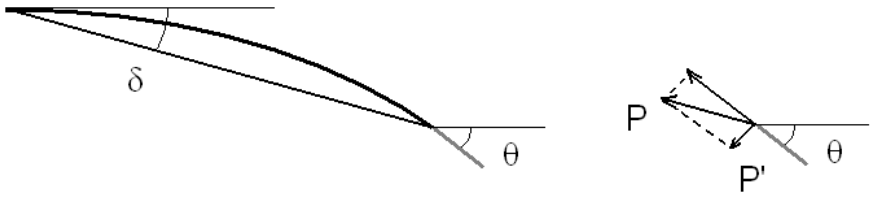

Figure D.2: Pre-compression force on the trailing edge.

The force on the trailing edge will cause a moment in plane of the trailing edge (in the direction of P'). A model of the two laminates and the two rubber bands is depicted in figure D.3. The trailing edge is represented as a simply supported beam. The laminates are modeled as two simple supports. The distance, l, is the width of one panel (95 mm). The distance to the point of application of the force and the laminate is denoted by d. The cross section of the trailing edge is drawn to the right of the beam.

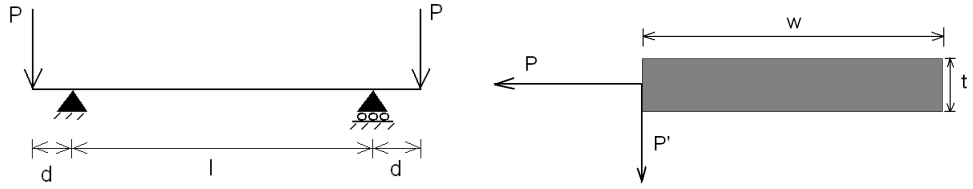

(a) Simply supported beam (b) Cross section

Figure D.3: Model of trailing edge loading.

The maximum moment is constant between the two supports: $M = Pd$. The curvature, κ,is given by:

$$\kappa = \frac{M}{EI} \tag{D.1}$$

The E-modulus for glass fibre reinforced polymer is assumed to be 25 GPa. The moment of inertia about the vertical axis through P',I_1, is calculated as follows:

$$I_1 = \frac{1}{3}tw^3 \tag{D.2}$$

Inserting this in equation D.1 gives $\kappa = 9.53 \cdot 10^{-12}$ $[1/mm]$. The amount of bending is so small that it can be assumed to be zero. Consequently the laminates will be loaded uniformly.[11]

For the force P' an analogous approach can be applied. The only difference is that the moment of inertia must now be taken around the cross section's axis of symmetry:

$$I_2 = \frac{1}{12}wt^3 \tag{D.3}$$

The moment, $M = P'd$. Substituting this in equation D.1 yields $\kappa = 9.78 \cdot 10^{-10}$ $[1/mm]$. Although this is a factor 100 larger than the value found for the in-plane bending, it still is very small. Therefore, also this curvature is neglected.

Finally, the force P' will cause a moment around the center of mass of the cross section. To prevent torsional deformation the fibres in the laminate could be placed at a relative angle of 45 *degrees*. Figure D.4 shows how the fibres should be oriented to counteract the torsional moment.[11]

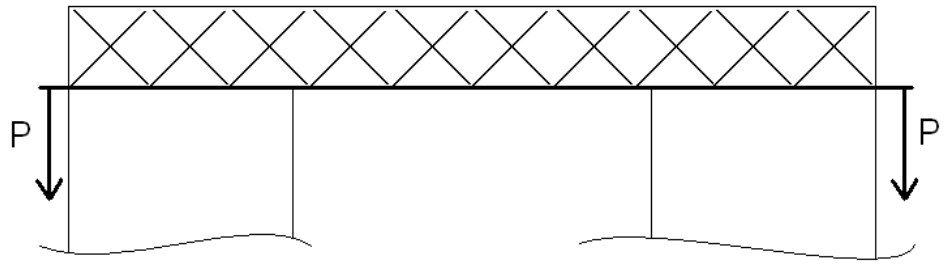

Figure D.4: Fibre orientation in the trailing edge (top view).

Acknowledgements

The past year has been an adventure for me, trying to design and build the first morphing wing, actuated by piezoelectric materials. I was not alone in this adventure and there are a lot of people that I would like to thank for helping me bringing it to a good ending. First of all my esteemed mentor in Delft, ir. Lars Krakers and my supervisor, prof. dr. ir. Michel van Tooren. Also at the faculty of aerospace engineering, I would like to thank dr. Mostafa Abdallah (MSc) and dr. ir. Leo Veldhuis.

But what is an engineer if there are no people who can tell him how to build his design? Therefore I would like the following people at Delft Aerospace for their practical help in the field of composites, electronics and wind tunnel tests: ir. Maarten Labordus, Hans Weerheim and Leo Molenwijk. My fellow students with whom I did this project with, ir. Roeland de Breuker, Ross McMurtry and Domenico Casella, thank you for all your efforts that made this project to a success.

A special thank you is reserved for the person that inspired me, motivated me, and laid the basis for this project. That is my supervisor at Auburn University, and my dear friend, dr. Ron Barrett. His creativity really inspired me in my project work. For technical advise, also at AU, I thank Christoph Burger, without whom I would never have been able to make a flight worthy morphing wing. At the aerospace department there are a number of people I would like to thank for helping me, either with small technical adjustments, or with big building projects: Lori Prothero, Shannon Wheatley, Mike Brennison, Amanda Gilliand, Ryan Leurck, Richard Bramlette, Robert Love and Brooke Hill.

Bibliography

[1] Anderson, J.D. "Fundamentals of Aerodynamics", second edition; McGraw Hill, copyright 1991

[2] Barrett, R.M. and Tiso, P., "Post Buckled Precompressed Actuator," International Patent Application PCT/NL2005/000054, by Delft University of Technology, Holland, 25 January 2005

[3] Barret, R., R. McMurtry, R. Vos, P. Tiso, R de Breuker, "Post-buckled precompressed (PBP) elements: a new class of flight control actuators enhancing high speed autonomous VTOL MAVs"; SPIE Paper No 5762-16, presented San Diego, California 6-10 March 2005

[4] Barrett, Ron, "Active Plate and wing research using EDAP elements", Smart Mater. Struct.1 (1992) 214-226, June 1992

[5] Barrett, R, Frye, P and Schliesman, M "Design, construction and characterization of a flightworthy piezoelectric solid state adaptive rotor" Smart Mater. Struct. 7 (1998) pages 422-431.

[6] Barrett, R., "Introduction to adaptive aerostructures" Lecture material, Fall 2003

[7] Bramlette, R and R. Leurck, "A method for control surface deflection utilizing Piezoceramic Bimorph Actuators", proceedings of the 56^{th} AIAA Southeastern Regional Student Conference, Gainesville, Florida, 4 April 2005

[8] Breuker, Roeland de, "Structural and aeroelastic modeling of adaptive beams"; Master thesis, TU Delft, December 2004

[9] Cesnik, Carlos E. S., "Wing shape deformation for high-performance aerial vehicles"; ICASE Morphing Seminar Series, NASA LaRC26 June 2002

[10] Duffin, W.J. "Electricity and Magnetism" Cottingham, East Yorkshire, UK , W.J. Duffin Publishing 2001

[11] Gere, J.M. and Timoshenko, S.P. "Mechanics of Materials" Fourth SI edition; Stanly Thorns (Publishers) Ltd, 1999

[12] Jones, R.M. "Mechanics of Composite Materials" Hemisphere Publishing Cooporation, 1975

[13] Kikuta, T.M., "Mechanical Properties of Candidate Materials for Morphing Wings"; Thesis Submitted to the Faculty of the Virginia Polytechnic Institute and State University, December 11, 2003 Blacksburg, Virginia; 2003

[14] Lesieutre, G.A. and Davis, C.L., "Can a Coupling Coefficient of a Piezoelectric Acturato be Higher Than Those of Its Active Material?" Journal of Intelligent Materials Systems and Structures, Vol. 8, 1997, pp. 859-867

[15] Levin, Ori and Wei Shyy, "Optimization of low Renolds number airfoil with flexible membrane" ; CMES, vol.2, no.4, pp.523-536, 2001; Tech Science Press, 2001

[16] Lind, Rick, Mujahid Abdulrahim , Kenneth Boothe , and Peter Ifju, "Morphing for Flight Control of Micro Air Vehicles" AIAA-2003-5347, Department of Mechanical and Aerospace Engineering University of Florida

[17] Lindner, Douglas K., Zhu, Molly, Vujic, Nikola, Leo, Donald J. "Comparison of Linear and Switching Drive Amplifiers for Piezoelectric Actuators" AIAA-2002-1352

[18] McMurtry, "Performance Enhancement of PZT Piezoelectric Actuators for Aircraft Control", Master Thesis, TU Delft, June 2004

[19] Mueller, Thomas J, "Aerodynamic Measurements at Low Reynolds Numbers for Fixed Wing Micro-Air Vehicles"; VKI, Belgium, September 13-17, 1999

[20] Roskam, dr. Jan, "Airplane Design, part 6: Preliminary caluculation aerodynamic, thrust and power characteristics"; University of Kansas, 1990

[21] Ruijgrok, G.J.J. "Elements of Airplane Performance" Delft University press, 1996

[22] Sathaye, Sagar Sanjeev, "Lift Distributions on Low Aspect Ratio Wings at Low Reynolds Numbers"; Worcester Polytechnic Institute, faculty of Mechanical Engineering, May 2004

[23] Torenbeek prof. ir. E. "Inleiding luchtvaarttechniek 1" Technische Universiteit Delft, faculteit der Luchtvaart- en Ruimtevaarttechniek, januari 1996

[24] Torres, Gabriel and Mueller, Thomas J, " Micro Aerial Vehicle Development: Design, Components, Fabrication and Flight-testing"; University of Notre Dame, 117 Hessert Center

[25] Drela, Mark and Youngren, Harold "XFOIL 6.94 User Guide" MIT and Aerocraft, Inc. 10 Dec 2001. http://raphael.mit.edu/xfoil/xfoil_doc.pdf

[26] www.defense-aerospace.com; found on September 16^{th}, 2004.

[27] www.newscientist.com/news; found on September 16^{th}, 2004.

[28] www.aae.uiuc.edu/m-selig/uiuc-lsat.html; found September 23^{rd}, 2004

[29] www.nd.edu/ mav/competition.htm; found September 21^{st}, 2004

[30] www.aae.uiuc.edu/m-selig/uiuc-lsat.html; found September 23^{rd}, 2004

[31] www.nd.edu/ mav/competition.htm; found September 21^{st}, 2004

[32] www.epson.co.jp/e/newsroom; found September 16^{th}, 2004

[33] www.ae.msstate.edu/ masoud/Teaching/SA2; found October 10^{th}, 2004

[34] www.picoelectronics.com/dcdclow/pe62_63.htm; found December 13^{th}, 2004

[35] www.engineering.gr/design/home; found January 10^{th} 2005

[36] www.darpa.mil/dso/thrust/matdev/mas.htm; found August 9^{th} 2005

[37] www.afrl.af.mil/accomprpt/dec02/images/dec$_7a.jpg$; $foundAugust9^{th}$ 2005

[38] www.libraries.wright.edu/icons/special/flyer.gif; found August 9^{th} 2005

[39] www.texasbeyondhistory.net/forts/images/eagle-sm.jpg; found August 9^{th} 2005